Fermi National Accelerator Laboratory

TM-1682

A Bottom Collider Vertex Detector Design, Monte-Carlo Simulation and Analysis Package

P. Lebrun
Fermi National Accelerator Laboratory
P.O. Box 500
Batavia, Illinois 60510

October 1, 1990

Operated by Universities Research Association Inc. under contract with the United States Department of Energy

A Bottom Collider Vertex detector design, Monte-Carlo simulation and analysis package.

P. Lebrun
Fermi National Accelerator Laboratory, Batavia, Illinois 60510, USA

Abstract : A detailed simulation of the BCD vertex detector is underway. Specifications and global design issues are briefly reviewed. The BCD design based on double sided strip detector is described in more detail. The GEANT3-based Monte-Carlo program and the analysis package used to estimate detector performance are discussed in detail. The current status of the expected resolution and signal to noise ratio for the "golden" CP violating mode $B_d \rightarrow \pi^+\pi^-$ is presented. These calculations have been done at *FNAL* energy ($\sqrt{s} = 2.$ TeV). Emphasis is placed on design issues, analysis techniques and related software rather than physics potentials.

I. INTRODUCTION : DESIGN SPECIFICATIONS.

The Silicon Vertex Detector (SVX) is one of the most critical elements of a Collider Detector dedicated to bottom Physics [1]. The SVX identifies the tracks belonging to B decays via reconstruction of secondary vertices.[2]. The decay length $c\tau$ of B mesons is about 360 μm, to be compared with the 5 to 10 μm intrinsic resolution achievable with a 25 μm pitch strip detector. Although we will describe in detail the effective resolution of such a detector through a complete Monte-Carlo simulation, it is worthwhile to first establish some elementary design rules based on a simple *back of the envelope* calculation.

In order to have good separation between B tracks and the primary vertex, one must have a spatial resolution at the vertex of the order of 20 to 40 μm. This is certainly bigger than the best intrinsic resolution one can achieve with silicon Detector (5 μm in perfect laboratory conditions, while in practice, with large systems, 10 μm is achievable). Such fine spatial resolutions will actually be required since the detectors cannot be located at the vertex itself and therefore resolution losses due to extrapolation to the vertices are to be anticipated. The obvious way to improve the spatial resolution at the vertices while keeping the detector resolution fixed is simply to improving the angular resolution of the tracks at this first detector, reducing this extrapolation error. Thus, we already three major limitations to the position resolution at the vertices : (i) the intrinsic silicon strip resolution (ii) the extrapolation error from the silicon wafer to the vertices (iii) the multiple scattering uncertainty in computing the track angles required to perform this extrapolation.

The first detector comes within 1.5 cm. of the beams. There are many reasons why this distance cannot be made smaller. One of them is certainly radiation damage. In order to minimize the extrapolation error, one must place the second detector of similar resolution at distances greater than this 1.5 cm. As described later, a track is detected by at least 3 planes (typically 5 to 10) located between 2 and 5 cm apart from each other, leading to an angular resolution of a few tens of a mr. Unfortunately, such a sufficient resolution is quickly degraded by multiple scattering. A 200 μm thick silicon plane will deflects a track of momentum P (in GeV/c) in average by an angle of :

$$\theta_{ms} \approx .65 \times 10^{-3}/P$$

Therefore, at a few GeV/c or less (0.5 GeV), the angular resolution (1.3 mr) will be limited by multiple scattering (1.3 mr can easily be achieved by placing 2 wafers at a distance of 2 cm. Even worse, since the added material required for mechanical support or readout electronic has not been taken into account in this naive calculation. Thus, the multiple scattering effect will have to be carefully simulated in the Monte-Carlo program and taken into account in the track fitting algorithm.

Clearly, in order to minimize both the amount of multiple scattering and the number of pixels or strips above pedestals - and therefore the event size and complexity-, one has to place wafers perpendicular to these tracks. Unfortunately, in a hadron collider environment, this is very difficult to achieve, for two reasons :

- The tracks are emitted over 4π, in the lab frame. If one requires large acceptance and keeps the angle of incidence at 90°, one must design a *silicon ball!* .
- The source (the primary vertex) of these tracks can not be kept at the same location : the size of the luminous region along the Z axis extends over 60 cm at the Tevatron, which is much bigger than the typical size of a silicon

wafer. Thus, the geometry is only optimum over either a small region along the Z axis or a small solid angle (see Fig. 1). For instance, a *BARREL* detector (as defined on fig. 3) is designed to reconstruct tracks in the central region ($|\eta| < 1.2$), but will be sensitive to tracks at much greater rapidities if the primary vertex occurs in the tail of this luminous region. Similarly, a *DISK* wafer is designed to detect small angle (high rapidity) tracks, but will be in the path of low momentum, small rapidity tracks to be measured by a *BARREL* wafer. Currently, this width σ_z is of the order of 30 cm to 50 cm at the Tevatron, and is expected to be 7 cm at the SSC. Clearly, as shown in this study, there is a big premium in reducing this width. Calculations described in this paper have been done with σ_z arbitrarily set to 30. cm.

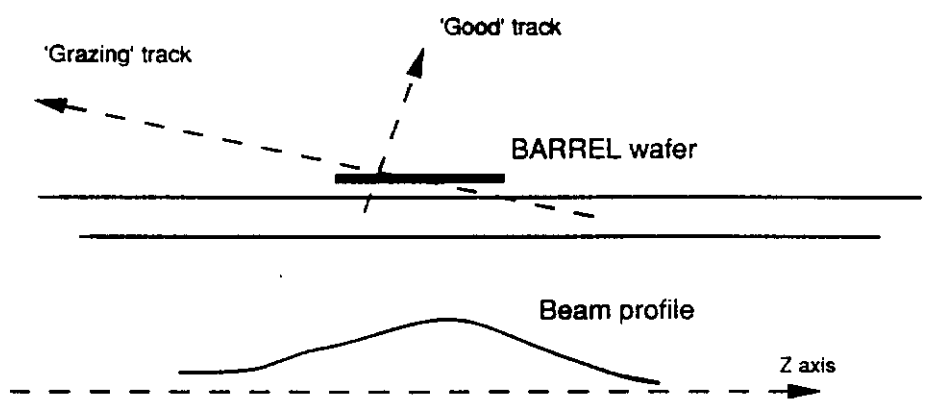

FIG. 1. The *no-win* game in designing an optimised geometry for the Silicon wafer layout : a module intended to detect at small rapidity will be in the path - at grasing incidence - for a track at large rapidity coming from a vertex located in the wing of the luminous region.

In order to cover a large rapidity gap ($|\eta| < 3.5$), both *DISK* and *BARREL* wafers are required. More complex geometries have been disregarded in face of the tremendous mechanical complexity in building a very light - but rigid - structure capable of sustaining of the order of a few kW. of heat transfer and, as demonstrated below, this *DISK* / *BARREL* in a dipole field implies already quite a complex track reconstruction and fitting code.

Another related issue is the effective 2 track resolution, driven by the probability of finding a *confusing* track in the vicinity of the *measured* track. This probability not only depends on the geometry of the detector (see Fig 2 for an intuitive definition) and the average charged multiplicity in the event, but also depends on unforeseen dynamical correlations between tracks in the event (i.e. jets or mini jets, decays..). Assuming an average multiplicity of 50 charged tracks per events, the average azimuthal separation between 2 tracks is about 125 mrad., corresponding to an average distance on the *BARREL* wafer located at 1.5 cm of 1.8 mm, or 75 25 μm strips. In the absence of these dynamical correlations and assuming a critical 2 tracks minimum allowed 2-track separation of 1 to 3 strips, the hit confusion probability appears to be of the order of a few percent or less. This calculation assumes that the strips measuring this azimuthal angle extend over the complete rapidity gap.

Fixed target experiments have been quite successful in reconstructing charm decays very cleanly with similar hit confusion probabilities. But this argument must be taken very cautiously. As we shall see later, a more correct calculation taking into account secondary decays, conversions, looping tracks in the magnetic field and so forth... gives hit confusion probabilities much greater (up to an order of magnitude !) than the simple calculation described above.

Nevertheless, it is true that the average cartesian distance between hits is much larger than the intrinsic resolution of the detector. Thus, this problem can be solved with pixel devices. Unfortunately these devices are undoubtedly more costly than conventional strip detectors. They are also likely to introduce more material in the detector. One of the main purposes of this study is to determine the appropriate strip length as a function of the event topology and detailed detector geometry. These questions can not be answered by a simple calculation, particularly when all

the other effects previously mentioned, such as finite detector resolution, multiple scattering and the nasty collider geometry are considered. Fast and simplified simulations have been done ([1]), demonstrating the need for a 3-dim. vertex detector and determining the required resolution at the wafer. Yet, because these simulations did not produce *exact raw data* , issues such as the confusion probability were not addressed in an objective way. Therefore, a global (entire events are simulated) , but yet detailed (raw data is produced) simulation calculation is highly justifiable, it's current status is described in detail in this note.

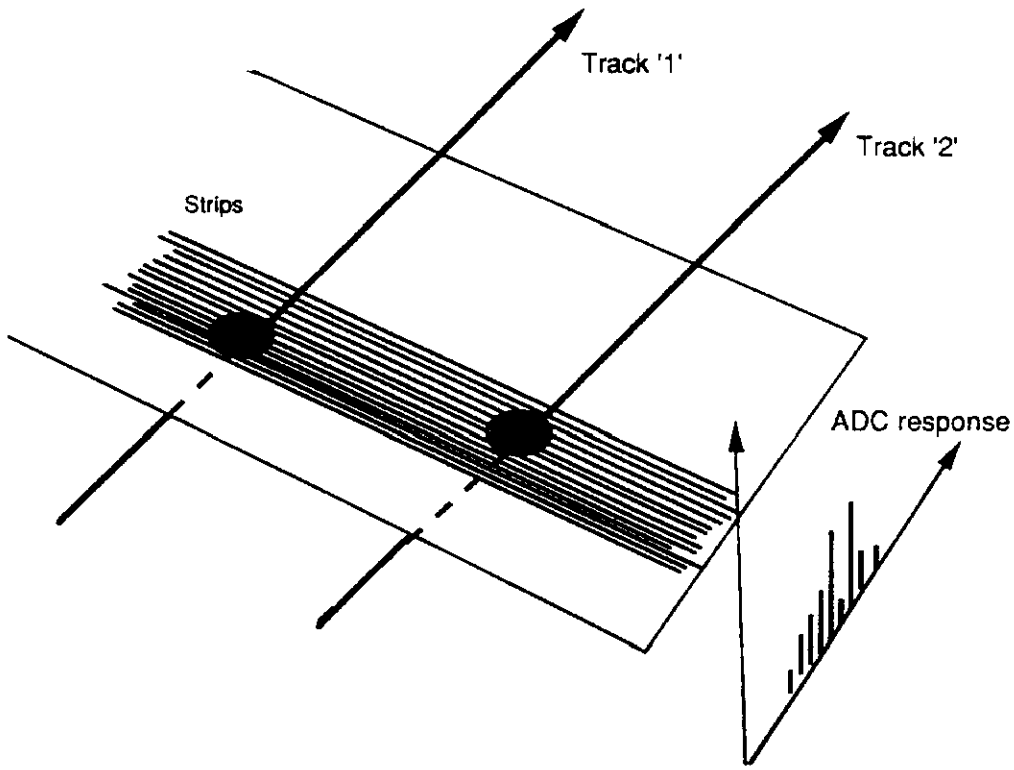

FIG. 2. Intuitive definition of the hit confusion probability : 2 tracks are crossing the detector plane at widely separated locations. Unfortunately one or more strips detect charge created by both tracks. This problem is specific to a 2-dim. planar detector (i.e. strip detector). Pixels detectors are intrinsically 3-dimensional and do not suffer from this basic flaw.

This paper is organised as follows. The GEANT3 implementation of the SVX Monte-Carlo is described first. The ISAJET event generation, the geometrical layout, the tracking and the final digitisation are explained in detail. Second comes the description of the algorithm used to associate Silicon hits to tracks, and tracks to secondary vertices. Quantitative features of the raw data is described such as multiplicities and ADC spectra .Preliminary results on the effective resolution are given as a function of momentum and track topology. This resolution has been studied at the wafer locations and at the vertex level. This requires a track fitting package. Finally the effective *merit factor* of the SVX detector is discussed in the particular case of the CP violating decay $B_d \rightarrow \pi^+\pi^-$. Some important technical or computational aspects are discussed in the appendix, such the intrinsic accuracy of the Monte-Carlo simulation package. The conclusion addresses future developments of this software (such as track fitting and accuracy improvements) and the required modifications to the *reference design* described in the next section, such as strip orientations and wafer shapes. Although these calculations have been done at FNAL c. m. energy ($\sqrt{s} = 2.0$ TeV) and assuming a proton-antiproton collider, the conclusions are valid at the SSC.

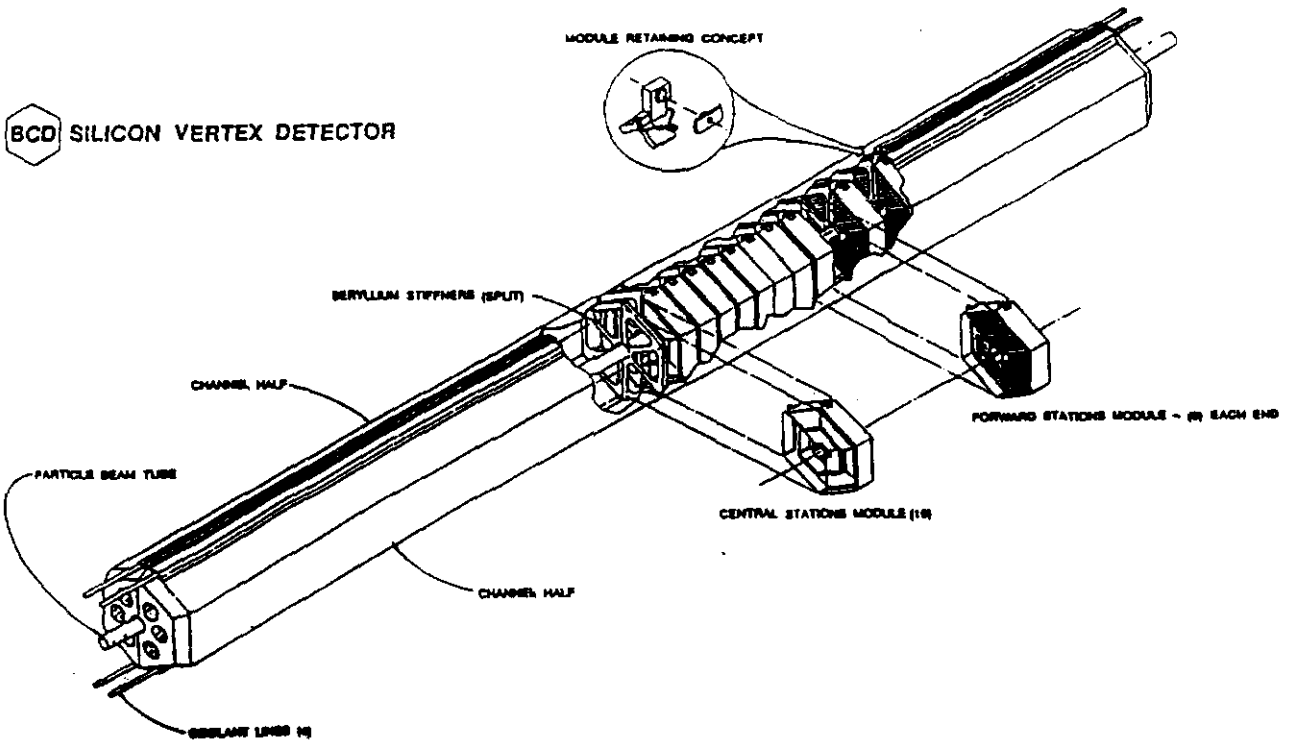

FIG. 3. The *reference* design of the BCD vertex detector (SVX) [1] is shown on this drawing. The hexagonal shaped modules surrounding the beam pipe are located in a Beryllium gutter.

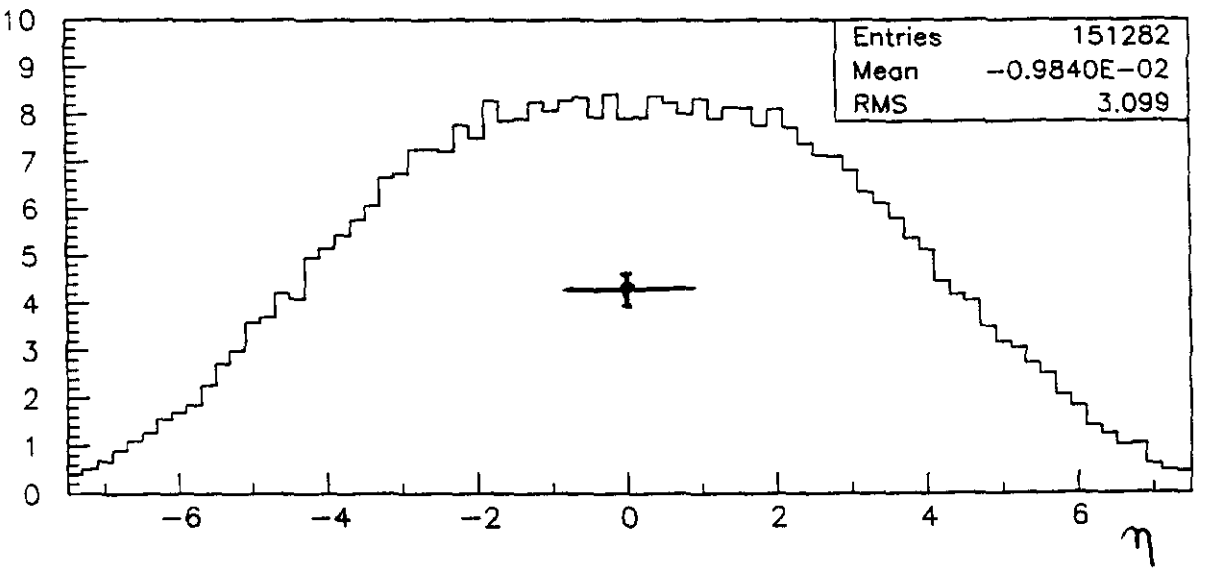

FIG. 4. Generated number of charged particles per unit of rapidity from the ISAJET Monte-Carlo. The center of mass energy is 2 Tev, Beams are Proton/Antiprotons and $B - jet$ option was requested with a range of transverse momentum is 1.0 to 20.0 GeV/c. Decays products from resonances (such as the the ρ^0) as well as from weak decays occurring within 1 cm. radius off the primary vertex are included. Minimum bias events are characterised in reality by much lower (up to a factor 2) multiplicities. The single data point refers to CDF low P_t data [3].

II. DESCRIPTION OF THE GEANT3 IMPLEMENTATION.

GEANT3 [15] has been chosen for its flexibility, support within the FERMILAB Computing Division and its rather complete set of HEP simulation tools, such as the particles dictionary, interaction of particle with matter, decays in flight and so forth. The SVX simulation is only one part of a complete Bottom Collider Detector Monte-Carlo package. BCD is currently using only one 'main' GEANT3 setup for all the detector components. One can easily turn on/off subdetector components. Most of the work described in this note has been done using only the SVX option. We carefully checked that other detector components such as the STRAW tracking system can be run at the same time without geometry inconsistencies or data structure clashes. Monte-Carlo data samples have been generated with and without a magnetic field (a 'perfect' 1.0 Tesla dipole field, perpendicular to the beam). The GEANT3 system has many interfaces to sophisticated *event generator* packages, such as ISAJET [18] or PYTHIA [19]. Rather arbitrarily, we used ISAJET for this analysis. More technical details on the computing aspects are described in the appendix.

A. The Kinematics : Use of the ISAJET Monte-Carlo.

Minimum bias events as well as Charm and Beauty jets samples have been generated using the ISAJET package (Version 6.25). A typical B event is shown on Fig 6. Evidently, one of the most important parameter is the track multiplicity as a function of the pseudo-rapidity (Fig. 4). The multiplicity observed in *minimum bias* event is smaller than the one observed in these ISAJET $B-jets$ events. Unfortunately, the Monte-Carlo *minimum bias* does not necessarily agrees with true *minimum bias* data measured by CDF [3]. This issue will be investigated in further versions. In any event, studying the 'worst case' is a good engineering practice at the design stage. Thus, most of the calculation presented below have been done with $B-jets$ event topology, where the multiplicity is almost twice as high as the one measured by CDF (fig 4).

$B-jets$ fragmentation produces B mesons as well as B baryons. The extended BCD/GEANT3 particle dictionary knows about all stable mesons and Baryons made of u, d, s, c and b quarks. Branching ratios are *particle data group* value, or, if not yet measured, most probable values based on phase space considerations and known quark weak decay matrix elements [6]. The decay modes and branching ratios used in this simulation for the B_u and the B_d are available on Table I. So far, all decay products are produced according to phase space, ignoring spin orientation or other kind of angular correlation. Since all particles with a life time greater than $\approx 10^-14$ sec are traced by GEANT, vertex positions and associated track lists are saved. Given a particle, the entire genealogical tree up to the primary vertex can be reconstructed once the event has been completely generated and tracked through the entire detector. In order to study particular physics topics, the user has the possibility of selecting a particular decay mode - such as $B_d \rightarrow \pi^+\pi^-$ -. The other B in the event decays following the unbiased table I. The event might be aborted prior to the tracking phase if kinematical cuts - such as invariant mass cuts on any $\pi^+\pi^-$ are not satisfied.

Finally, provision has been made in the Monte-Carlo to generate multiple ISAJET events within a single GEANT3 event, in order to simulate multiple events per rf bucket expected to occur at high luminosity. Specific results in term of pattern recognition losses are not yet available, but can be easily deduced from single event results, since no correlations between these simultaneous events are expected.

B. The SVX Detector Geometry

The SVX geometrical layout is based on a conceptual design from the BCD collaboration (Fig 3). Engineering studies are currently underway at FERMILAB[4,5]. Mechanical issues, such as assembling, alignment, electrical connections, cooling and electronics must be considered jointly. Given the severe constraints on the amount of material, none of these issues are trivial and do impact on each other.

Clearly, many small mechanical features displayed on Fig 3 can not be - and probably should not - be implemented in this simulation, although the average amount of material 'seen' by the tracks must be respected. For instance, one can neglect some of the supports or frame mounts provided one also ignores the holes - or thinner elements - of the supporting gutter, keeping the average thickness seen by a generic track more or less correct.

TABLE I. Assumed decay modes and branching ratios for B_u and B_d. These values are obviously not the real ones, but follow the known patterns of B decay, such as average multiplicities and leptonic fractions. Since these branching ratios are used for generic decay pattern studies or exclusively for the 'tagging' B mesons only, small differences in relative branching ratios can be considered as second order effects.

Decay mode B_d	Branching ratio (%)	Decay mode B_u	Branching ratio (%)
$D^{*-}\ \pi^+$	0.330	$D^{*-}\ \pi^+\ \pi^+$	0.250
$D^{*-}\ \rho^+$	8.000	$D^{*-}\ \pi^+\ \pi^+\ \pi^0$	2.750
$D^{*-}\ \pi^+\ \pi^0$	1.500	$D^{*0}\ \pi^+$	0.270
$D^{*-}\ \pi^+\ \pi^+\ \pi^-$	3.300	$J/\psi\ K^+\ \pi^+\ \pi^-$	0.110
$D^{*-}\ e^+\ \nu$	7.000	$D^0\ e^+\ \nu$	8.500
$D^{*-}\ \mu^+\ \nu$	7.000	$D^0\ \mu^+\ \nu$	7.700
$J/\psi\ K^{*0}$	0.370	$D^-\ \pi^+\ e^+\ \nu$	3.800
$D^+\ e^-\ \nu$	6.160	$D^-\ \pi^+\ \mu^+\ \nu$	3.300
$D^+\ \mu^-\ \nu$	5.580	$D^0\ \pi^+$	0.470
$D^0\ e^-\ \nu\ \pi^+$	2.760	$D^0\ \pi^+\ \pi^0$	2.800
$D^0\ \mu^-\ \nu\ \pi^+$	2.390	$D^0\ \pi^+\ \pi^0\ \pi^0$	2.100
$D^0\ \pi^0$	0.360	$D^0\ \pi^+\ \pi^0\ \pi^0\ \pi^0$	1.000
$D^0\ \pi^0\ \pi^0$	0.580	$D^0\ \pi^+\ \pi^0\ \pi^0\ \pi^0\ \pi^0$	0.500
$D^0\ \pi^0\ \pi^0\ \pi^0$	0.440	$D^-\ \pi^+\ \pi^+$	0.2500
$D^0\ \pi^0\ \pi^0\ \pi^0\ \pi^0$	0.290	$D^-\ \pi^+\ \pi^+\ \pi^0$	1.300
$D^+\ \pi^-$	0.800	$D^-\ \pi^+\ \pi^+\ \pi^0\ \pi^0$	4.700
$D^+\ \pi^-\ \pi^0$	1.600	$D^-\ \pi^+\ \pi^+\ \pi^0\ \pi^0\ \pi^0$	3.000
$D^+\ \pi^-\ \pi^0\ \pi^0$	1.600	$D^-\ \pi^+\ \pi^+\ \pi^0\ \pi^0\ \pi^0\ \pi^0$	2.500
$D^+\ \pi^-\ \pi^0\ \pi^0\ \pi^0$	1.090	$D^0\ \pi^+\ \pi^+\ \pi^-$	1.300
$D^+\ \pi^-\ \pi^0\ \pi^0\ \pi^0\ \pi^0$	0.870	$D^0\ \pi^+\ \pi^+\ \pi^-\ \pi^0$	3.400
$D^0\ \pi^+\ \pi^-$	5.660	$D^0\ \pi^+\ \pi^+\ \pi^-\ \pi^0\ \pi^0$	4.300
$D^0\ \pi^+\ \pi^-\ \pi^0$	2.100	$D^0\ \pi^+\ \pi^+\ \pi^-\ \pi^0\ \pi^0\ \pi^0$	3.600
$D^0\ \pi^+\ \pi^-\ \pi^0\ \pi^0$	2.540	$D^0\ \pi^+\ \pi^+\ \pi^-\ \pi^0\ \pi^0\ \pi^0\ \pi^0$	4.000
$D^+\ \pi^+\ \pi^-\ \pi^-$	1.560	$D^-\ \pi^+\ \pi^+\ \pi^+\ \pi^-$	1.200
$D^+\ \pi^+\ \pi^-\ \pi^-\ \pi^0$	3.260	$D^-\ \pi^+\ \pi^+\ \pi^+\ \pi^-\ \pi^0$	3.000
$D^+\ \pi^+\ \pi^-\ \pi^-\ \pi^0\ \pi^0$	3.260	$D^-\ \pi^+\ \pi^+\ \pi^+\ \pi^-\ \pi^0\ \pi^0$	3.700
$D^+\ \pi^+\ \pi^-\ \pi^-\ \pi^0\ \pi^0\ \pi^0$	2.180	$D^-\ \pi^+\ \pi^+\ \pi^+\ \pi^-\ \pi^0\ \pi^0\ \pi^0$	6.700
$D^+\ \pi^+\ \pi^-\ \pi^-\ \pi^0\ \pi^0\ \pi^0\ \pi^0$	1.740	$D^0\ \pi^+\ \pi^+\ \pi^+\ \pi^-\ \pi^-$	1.100
$D^0\ \pi^+\ \pi^+\ \pi^-\ \pi^-$	0.870	$D^0\ \pi^+\ \pi^+\ \pi^+\ \pi^-\ \pi^-\ \pi^0$	2.800
$D^0\ \pi^+\ \pi^+\ \pi^-\ \pi^-\ \pi^0$	2.180	$D^0\ \pi^+\ \pi^+\ \pi^+\ \pi^-\ \pi^-\ \pi^0\ \pi^0$	9.700
$D^0\ \pi^+\ \pi^+\ \pi^-\ \pi^-\ \pi^0\ \pi^0$	2.760	$D^-\ \pi^+\ \pi^+\ \pi^+\ \pi^+\ \pi^-\ \pi^-$	0.500
$D^0\ \pi^+\ \pi^+\ \pi^-\ \pi^-\ \pi^0\ \pi^0\ \pi^0$	4.780	$D^-\ \pi^+\ \pi^+\ \pi^+\ \pi^+\ \pi^-\ \pi^-\ \pi^0$	5.500
$D^+\ \pi^+\ \pi^+\ \pi^-\ \pi^-\ \pi^-$	0.580	$D^0\ \pi^+\ \pi^+\ \pi^+\ \pi^+\ \pi^-\ \pi^-\ \pi^-$	3.900
$D^+\ \pi^+\ \pi^+\ \pi^-\ \pi^-\ \pi^-\ \pi^0$	1.520		
$D^+\ \pi^+\ \pi^+\ \pi^-\ \pi^-\ \pi^-\ \pi^0\ \pi^0$	5.290		
$D^0\ \pi^+\ \pi^+\ \pi^+\ \pi^-\ \pi^-\ \pi^-$	0.360		
$D^0\ \pi^+\ \pi^+\ \pi^+\ \pi^-\ \pi^-\ \pi^-\ \pi^0$	4.000		
$D^+\ \pi^+\ \pi^+\ \pi^+\ \pi^-\ \pi^-\ \pi^-\ \pi^-$	3.340		

The GEANT3 3D geometry package allows the construction of a set of elementary volumes organised in a hierarchical *volume tree*. The SVX volume tree is displayed on Fig. 7. Three regions are defined : the Central region (SVXC) extending to $\pm$ 24 cm and the forward (and backward) high rapidity region (SVXR) extending to 1.75 m along the beam pipe. The set of physical volume is rather simple, consisting of a beam pipe (PIPE), a hexagonal shaped gutter containing the detectors (GUTT), a set of polygonal shaped Silicon wafers for the *DISK*, and rectangular shaped *BARREL* wafers (Fig. 8). Material type and other volume characteristics are given on Table IV. The Silicon thickness is assumed to be 200 μm, the Beryllium pipe and gutter, 300 μm. The length of a module is 4.8 cm, the central region has 10 modules and the forward regions have 9 modules each. (5). Table II and table III give detailed information on the strip configuration for the various wafer types.

TABLE II. Strip and wafer configuration, from a geometrical and electronic standpoint for the three layers of barrel shaped wafers ($BARREL_I$, $BARREL_M$ and $BARREL_O$ refers to the inner, middle and outer layer respectively). The number of readout channel is half the number of strips. A Data collector chip reads out 128 channels, that is 256 strips.

Layer location	$BARREL_I$	$BARREL_M$	$BARREL_O$
Pitch for the ϕ and Z strip (in μ)	25.	50.	50.
Length of the ϕ strip (in cm.)	4.6	4.6	4.6
Length of the Z strip (in cm.)	1.952	6.0	10.5
Relative stereoangle between ϕ and z strips	90°	90°	90°
Number of wafers per modules	6	6	6
Number of ϕ strips per wafer	780	1,200	2,100
Number of Z strips per wafer	1,840	920	920
Number of ϕ strips per module	4,680	7,200	12,600
Number of Z strips per module	11,040	5,520	5,520
Total number of ϕ strips	46,800	72,000	126,000
Total number of Z strips	110,400	55,200	55,200
Number of ϕ chips per wafer	4	5	9
Number of Z chips per wafer	8	4	4
Number of ϕ chips per module	24	30	54
Number of Z chips per module	48	24	24
Total number of ϕ chips	240	300	300
Total number of Z chips	480	240	240
Total number of modules		10	
Total number of wafers		180	
Total number of strips		466,240	
Total number of readout chips		1,800	

TABLE III. Strip and wafer configuration, for the inner and outer $DISK$ wafers. The configurations for the central and forward are identical. As for the $BARREL$ wafers, the Data collector chips read out 128 channels, that is 256 strips.

Layer location	$DISK_I$	$DISK_O$
Pitch for the U and V strip (in μ)	25.	50.
Minimum length of the U or V strip (in cm.)	1.95	5.8
Maximum length of the U or V strip (in cm.)	6.0	10.3
Relative stereoangle between U and V strips	60°	60°
Number of wafers per modules	6	6
Number of U strips per wafer	1,392	776
Number of V strips per wafer	1,392	776
Number of U strips per module	8,352	4,656
Number of V strips per module	8,352	4,656
Total number of U and V strips	467,712	260,736
Number of U and V chips per wafer	12	7
Number of U and V chips per module	72	42
Total number of U and V chips	1296	756
Total number of central modules	10	
Total number of forward modules	18	
Total number of wafers	336	
Total number of strips	728,448	
Total number of readout chips	2,052	

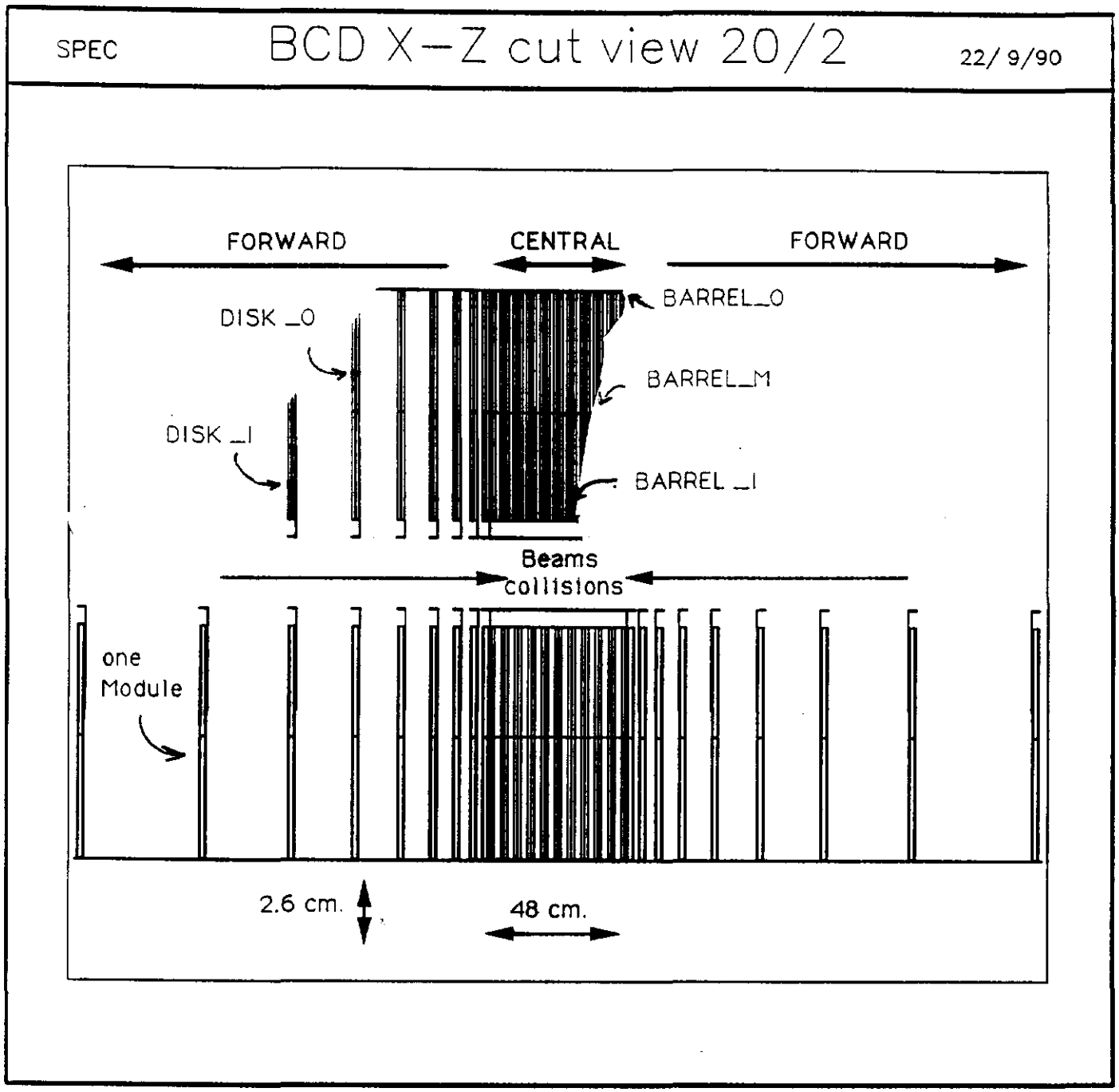

FIG. 5. A GEANT representation of SVX, showing more clearly the wafer arrangement : *DISK* wafers are perpendicular to the beam directions and *BARREL* are parallel to the beam. For obvious reasons, only the central region has *BARREL* wafers. The outer barrel radius is about 10 cm. Figure 8 describes in more detail how the *DISK* and *BARREL* wafer are arranged within a module . Note the horizontal scale along the beam has been compressed 10 times with respect to the vertical scale.

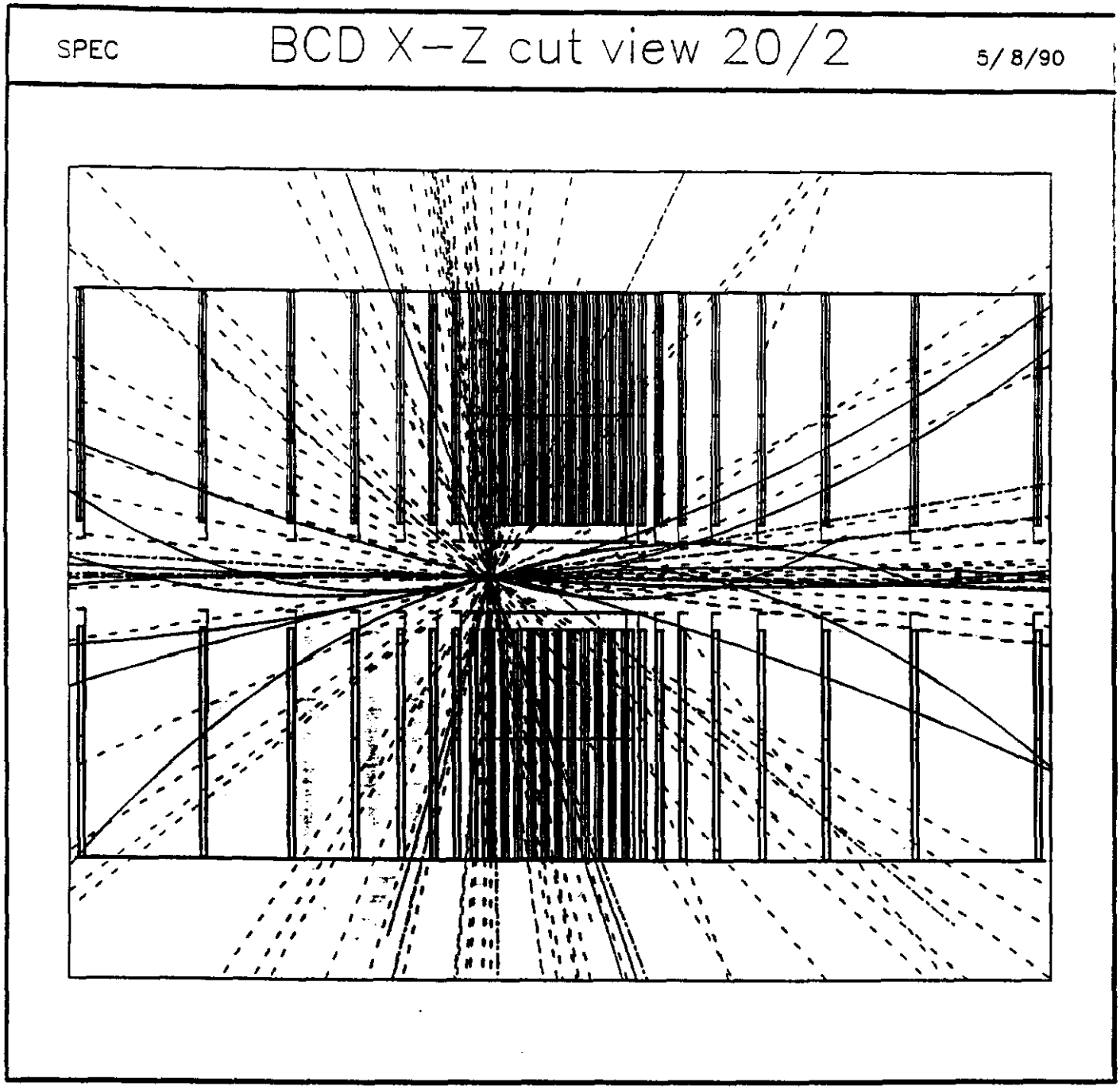

FIG. 6. A GEANT3 drawing of a typical event at FNAL c.m. energy. The detector shown on figure 5 is reproduced as well, illustrating the wide range of intersection angles of tracks and wafers. The scale is identical to the one on fig. 5 .

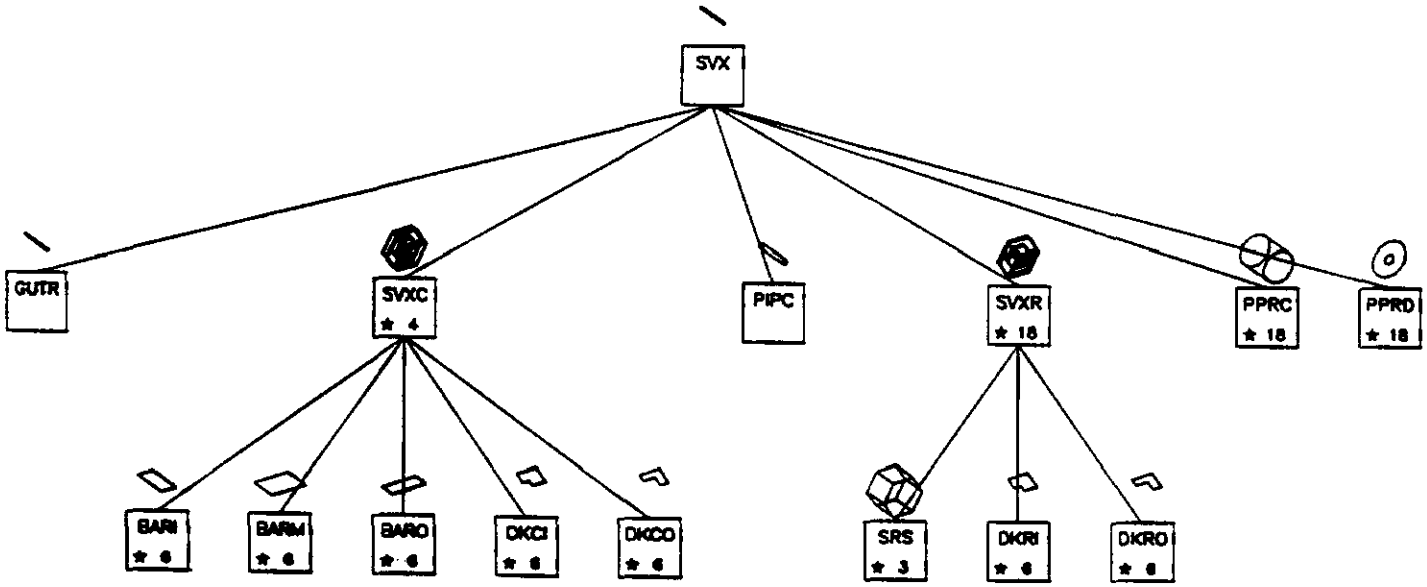

FIG. 7. The hierarchical Volume organisation in the GEANT3 simulation. At the top of the hierarchy, we have the three main regions, defined by a set of crude rapidity gaps, below the 'module' level, within a module we have 6 $DISK$ wafers and 3*6 $BARREL$ wafers ($BARREL$ are for the central region only).

At high rapidity ($\eta > 2.5 \rightarrow 3.$), the cylindrical geometry of the beam pipe and the use of $BARREL$ wafers become inappropriate because of excessive multiple scattering for these *grazing* tracks. The radial uncertainty due to multiple scattering for a track at an angle of incidence θ traversing the 300 μm thick Beryllium beam pipe and detected at a distance L from the vertex is essentially given by the product of θ_{ms} and L. At high rapidity, this becomes :

$$r_{pl} \approx \frac{4.0 \times 10^{-4}}{P \times \sqrt{sin(\theta)}} \times L \approx \frac{4.0 \times 10^{-4}}{P \times \sqrt{(\theta)}} \times L$$

with;
$\eta = ln(cot(\theta/2))$ and $\theta \approx 2. \times e^{-\eta}$

In order to balance the wafer occupancy, it is preferable to have forward (backward) $DISK$ with a fixed acceptance in pseudo-rapidity η, since the particle multiplicity is more or less independent of η. $\Delta\eta$ is fixed, hence, $\Delta\theta \approx 2.0 \times e^{-\eta} \times \Delta\eta$. Since the radial dimension R_d of these wafer is also constant, one must have :

$$L \approx \frac{R_d}{\Delta\theta} \approx \frac{R_d \times 0.5 \times e^{\eta}}{\Delta\eta}$$

$$r_{pl} \approx \frac{1.4 \times 10^{-4}}{P} \times \frac{R_d \times e^{1.5 \times \eta}}{\Delta\eta}$$

P, P_t and η are clearly related, this becomes :

$$r_{pl} \approx \frac{2.8 \times 10^{-4}}{P_t} \times \frac{R_d \times e^{0.5 \times \eta}}{\Delta\eta}$$

At $\eta \approx 3.0$, fixing R_d at 5.0 $cm.$, keeping $\Delta\eta = 0.5$, the distance is $L \approx 1$ meter and $r_{pl} \approx 60$ μm for a 1.0 GeV/c P_t track.

This effect is clearly more relevant at the SSC than at FNAL, because the relative B yield at high rapidity is only a few percent above a rapidity of 3. at FNAL c.m. energy, but is expected to rise to $\approx$ 50% at the SSC c.m. energy.

This worsened resolution may be avoided by use of a succession of conical (or 'flared') beam pipes, as shown on Fig. 9 Since only the endcaps of these cones are seen the tracks, the cones themselves have been omitted in the GEANT3

simulation for sake of simplicity. This omission obviously will lead to an underestimate of the multiple scattering for tracks not originating at $z = 0.$, or tracks deflected by the magnetic field, at high rapidity. This flaw will be corrected in later versions.

C. The Tracking : From the kinematics to the GEANT 'hits'

The GEANT3 system performs the tracking phase automatically , by propagating each particle from one volume to the next until the particle decays, interacts or leaves the detector. A track is defined as a particle path. The particle comes either directly from the primary vertex (*prompt* or *primary* track) or from subsequent physics processes occuring in the detector, such as decays in flight, photon conversions or secondary interactions (*secondary*). The tracking accuracy and related GEANT parameters are given in table IV.

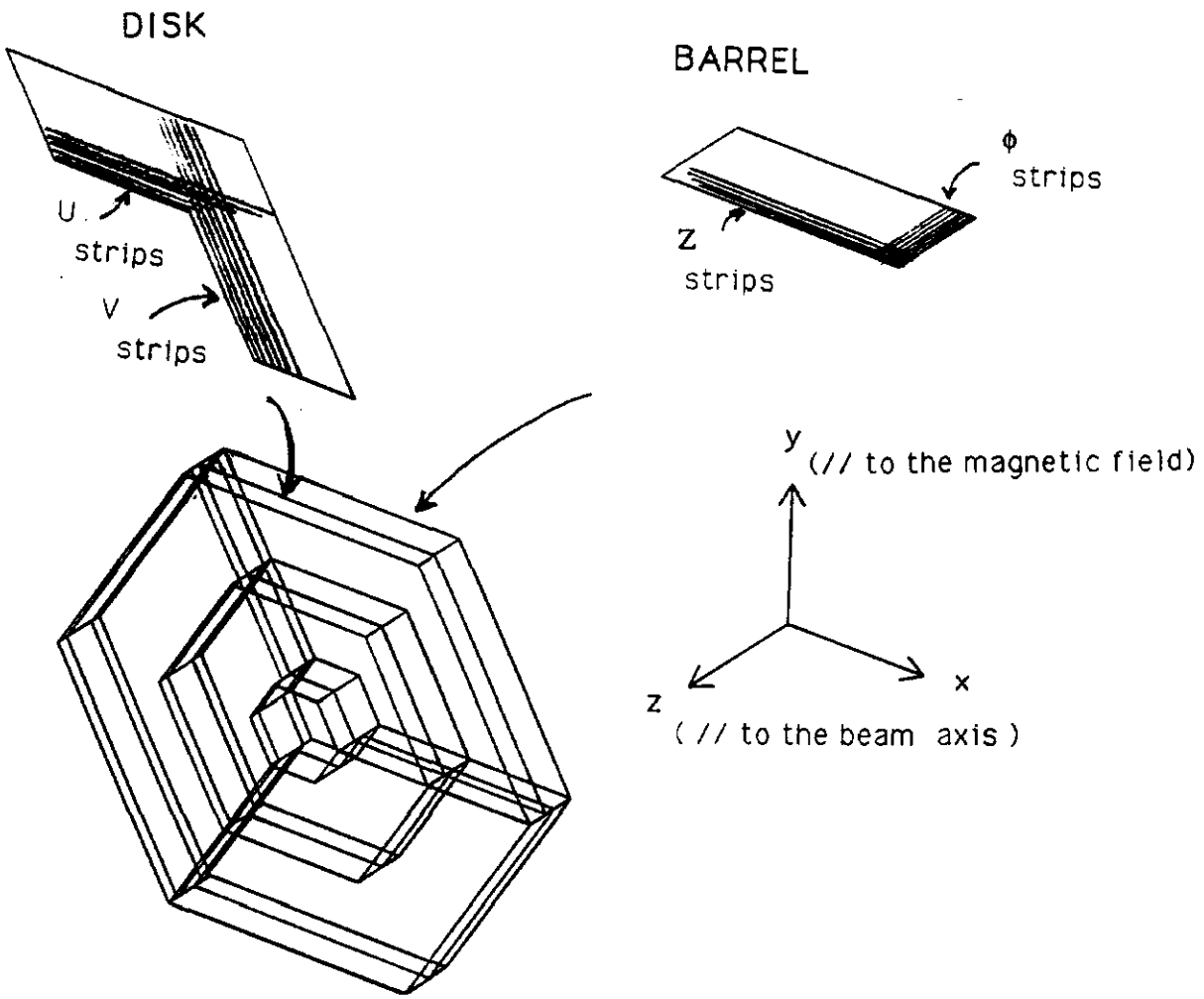

FIG. 8. Detailed representation of a single module and the relative strip orientation. A module is made of 6 inner disks ($DISK_I$) and 6 outer disks ($DISK_O$), each of them covering 120° azimuthal angle. In most cases, a track intersects 2 disks within a module. In order to ensure appropriate air flow, these wafers are located at different Z positions, following a helicoidal path. For the central modules, 6 inner, middle and outer barrel (*BARREL*) surround the beam region. The following convention for the strip stereoangle is used : the label refers to the coordinate being measured, for instance, the Z strip measure the track position along the beam. The approximate radius of a module is 10 cm., its length is 4.8 cm.

TABLE IV. List of materials, medium parameters related to the tracking accuracy and volume dimensions and types used in this simulation. These numbers have been directly extracted from the BCD/GEANT3 output listing. See GEANT3 manual for more details.

MATERIALS

MATERIAL		A	Z	DENSITY	RADIAT L	ABSORP L	NMIXT
BERILLIUMS	5	9.010	4.000	1.848	0.353E+02	0.387E+02	1
AIRS	15	14.610	7.300	0.001	0.304E+05	0.675E+05	1
VACUUMS	16	0.000	0.000	0.000	0.100E+17	0.100E+17	1
SILICONS	17	28.090	14.000	2.330	0.936E+01	0.456E+02	1

TRACKING MEDIA

TMED	MATERIAL	ISVOL	IFIELD	FIELDM	TMAXFD	DMAXMS	DEEMAX	EPSIL	STMIN
1 VACUUMS	16	0	2	10.00	10.00	0.000	0.000	0.001	0.000
2 BERYLLIUMS	5	0	2	10.00	10.00	0.004	0.010	0.001	0.000
3 AIR (0.01 mm)S	15	0	2	10.00	10.00	0.010	0.010	0.001	0.000
4 AIR (0.10 mm)S	15	0	2	10.00	10.00	0.050	0.050	0.010	0.000
5 AIR (1.00 mm)S	15	0	2	10.00	10.00	0.100	0.100	0.100	0.000
11 SILICONS	17	0	2	10.00	0.50	0.004	0.010	0.001	0.002
12 INACTIVE SILICONS	17	0	2	10.00	0.50	0.004	0.010	0.001	0.002

VOLUMES

VOLUME	NAME	NUMED	SHAPE	NPAR	PARAMETERS									
1	SPEC	3	BOX	3	0.100E+02	0.920E+01	0.175E+03							
2	BEAM	1	TUBE	3	0.000E+00	0.130E+01	0.175E+03							
3	SVX	3	BOX	3	0.920E+01	0.920E+01	0.175E+03							
4	GUTR	2	PGON	10	0.000E+00	0.360E+03	0.600E+01	0.200E+01-0.173E+03	0.911E+01	0.914E+01	0.173E+03	0.911E+01	0.914E+01	
5	SVXC	3	PGON	10	0.000E+00	0.360E+03	0.600E+01	0.200E+01-0.230E+01	0.169E+01	0.911E+01	0.230E+01	0.169E+01	0.911E+01	
6	BARI	11	BOX	3	0.976E+00	0.100E-01	0.230E+01							
7	BARW	11	BOX	3	0.300E+01	0.100E-01	0.230E+01							
8	BARO	11	BOX	3	0.525E+01	0.100E-01	0.230E+01							
9	DKCI	11	PGON	10	0.000E+00	0.120E+03	0.200E+01	0.200E+01-0.100E-01	0.171E+01	0.519E+01	0.100E-01	0.171E+01	0.519E+01	
10	DKCO	11	PGON	10	0.000E+00	0.120E+03	0.200E+01	0.200E+01-0.100E-01	0.521E+01	0.909E+01	0.100E-01	0.521E+01	0.909E+01	
11	DKRI	11	PGON	10	0.000E+00	0.120E+03	0.200E+01	0.200E+01-0.100E-01	0.171E+01	0.519E+01	0.100E-01	0.171E+01	0.519E+01	
12	DKRO	11	PGON	10	0.000E+00	0.120E+03	0.200E+01	0.200E+01-0.100E-01	0.521E+01	0.909E+01	0.100E-01	0.521E+01	0.909E+01	
13	SVXR	3	PGON	10	0.000E+00	0.360E+03	0.600E+01	0.200E+01-0.120E+01	0.169E+01	0.911E+01	0.120E+01	0.169E+01	0.911E+01	
14	SRS	12	PGON	10	0.000E+00	0.360E+03	0.600E+01	0.200E+01-0.120E+01	0.169E+01	0.171E+01	0.120E+01	0.169E+01	0.171E+01	
15	PIPC	2	TUBE	3	0.130E+01	0.133E+01	0.103E+02							
16	PPRC	2	TUBE	3	0.130E+01	0.133E+01	0.150E+01							
17	PPRO	2	TUBE	3	0.130E+01	0.504E+01	0.200E-01							

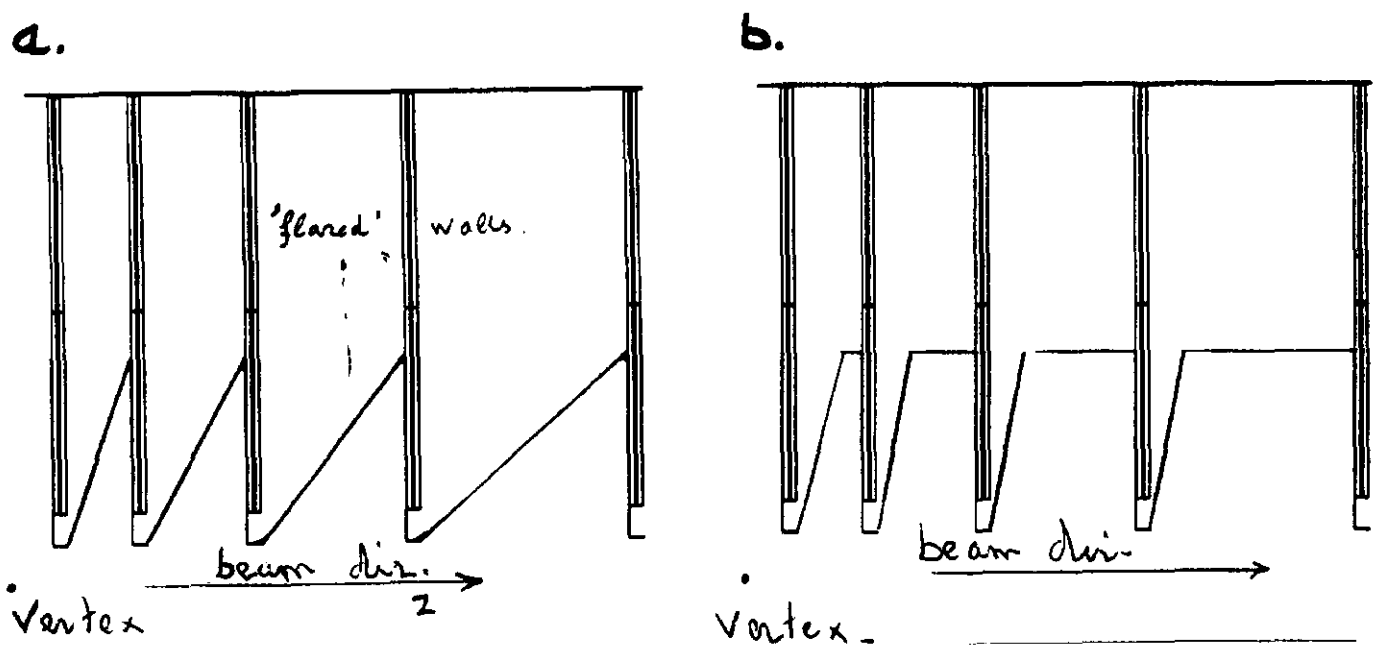

FIG. 9. The conical ('flared') or indented beam pipe arrangement. Although the total amount of material is bigger than the one in a simple cylindrical design, the resolution loss due to multiple scattering at the most crucial wafer - the one closest to the vertex - could be greatly reduced. Within a given module, the beam pipe is cylindrical. Choice between design *a* and *b* depends on mechanical or thermal considerations.

The particle positions, the direction cosinus ($1/P \times \partial P_x/\partial x$, $1/P \times \partial P_y/\partial y$, $1/P \times \partial P_z/\partial z$) and the absolute value of the momentum P are recorded whenever a track intersects a subdetector element, such as a wafer. This small data structure is called a GEANT hit. These hits are organised by detector 'sets'(only one set is considered in this analysis, SVX) and by detector type (*BARREL* (Inner, Middle and Outer) and *DISK* (Central/High Rapidity and Inner/Outer)). For a given wafer/track intersection, to each hit corresponds one and only one track. In most cases (i. e., if the track does curl in the magnetic field), there is only one hit per track per wafer.

D. The Digitisation : From the Hits to Simulated Raw Data

Once the entire event has been traced, the digitisation phase takes place. If the track intersect the sensitive region of the wafer (that is, if the distance of the track position at this intersection to the edge of the wafer is greater than one mm), the hit information is used to generate simulated raw data, *i.e.*, channel numbers and *ADC* data. This is done on a per wafer basis : all the hits for a given wafer must be considered jointly in order to simulate correctly the hit confusion cases. (see fig 2).

The entrance and exit points of the track on the wafer are computed from the hit information, assuming the track is a straight line. These wafers are *double sided* : the energy deposition is measured on both sides of the wafer. Each side has a different strip orientation (see fig 8, and table III, III).

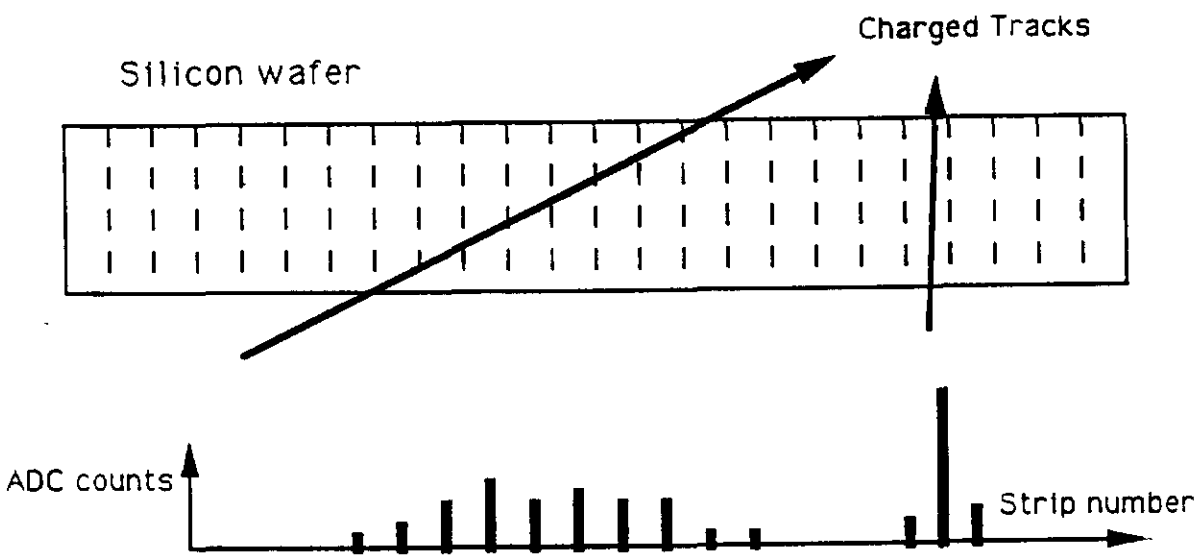

FIG. 10. A cluster is defined as a contiguous sequence of strips whose charge is significantly above the noise level. Note the cluster width (i. e., the number of strips) depends on the angle of incidence)

Because of the double sided feature of the wafer readout, the amounts of charge collected on each side are correlated to each other. Thus, the particle path inside the wafer is subdivided into *pseudo pixels*, where this 2-dimensional pixel grid is defined by the relative strip stereoangle and the strip pitch. For each pixels, the path length is computed exactly. This path length is converted into a most probable energy deposition, taking into the mass and kinetic energy of the particle as well as Landau fluctuations. This energy deposition is then converted into a number of electron/hole pairs, assuming that the sensitive region (i. e., the 'depleted' region inside the diode) is simply the thickness of the silicon wafer. It was assumed that for 90 KeV energy loss (corresponding to a path of 200 μm, for a minimum ionizing particle), 16,000 e/h pairs are created. These charges are collected on a per strip basis, one strip could be "charged" by more than one particle.

The next step is the simulation of the *charge sharing* readout scheme, by which only one out of two neighboring strips are readout. The amount of charge collected by a readout channel is simply the sum of the charge on the

corresponding strip and half of the charge on each neighbouring strip. The *r.m.s* noise of the preamplifier was assumed to 600 electrons. The amplification process is simulated for every active readout channel, assuming a perfectly linear *7-bit A* to *D* converter, with pedestal suppressed. Noise for neighbouring readout channel is also generated, and these channel become part of the data. At last, the discriminator at the output stage of the preamplifier is also simulated: strips with a signal less than 1,800 electron equivalents are disregarded. Assuming such a rather optimistic detector performance, it is not necessary to simulate electronic noise across the whole wafer for the following reason. The total signal for real tracks corresponds to 16,000 electrons, or roughly 40 ADC counts. An noisy channel will be isolated, with a small signal corresponding to less than 4 % of the signal corresponding to a real track (barely one channel count). Assuming that the electronic noise follows a Gaussian distribution, even with thousands of readout channel, the probability for a noisy channel to simulated a real track is negligible.

Contrary to the hit described above, a *D_hit* - defined by a strip number and a 7bit pulse height - can be associated to more than one track, if these tracks are confused. In order to diagnose pattern recognition failures at the analysis stage, the list of GEANT track numbers associated to such a D_hit is recorded on tape. Conversely, a given track will usually induce a significant charge on more than one strip because the angle of incidence of the track with respect to the detector plane. This purely geometrical effect is significant as soon as the strip width (25 or 50 μm) is of the order of (or smaller than !) of the Silicon thickness (200 μm) (Fig. 10).

E. The Final Output : a FZ File or 8mm Exabyte Tape

Given the large amount of computing time required to run such simulations, it is certainly worthwhile writing all relevant data on sequential mass media for further, detailed but less time consuming, analysis. The standard GEANT3 data structure *VERT* (vertex positions and related list of child particles), *KINE* (list of particles and related vertices), *HIT* (the list of hits) and *DIGI* (the list of D_hits) are saved for each event.

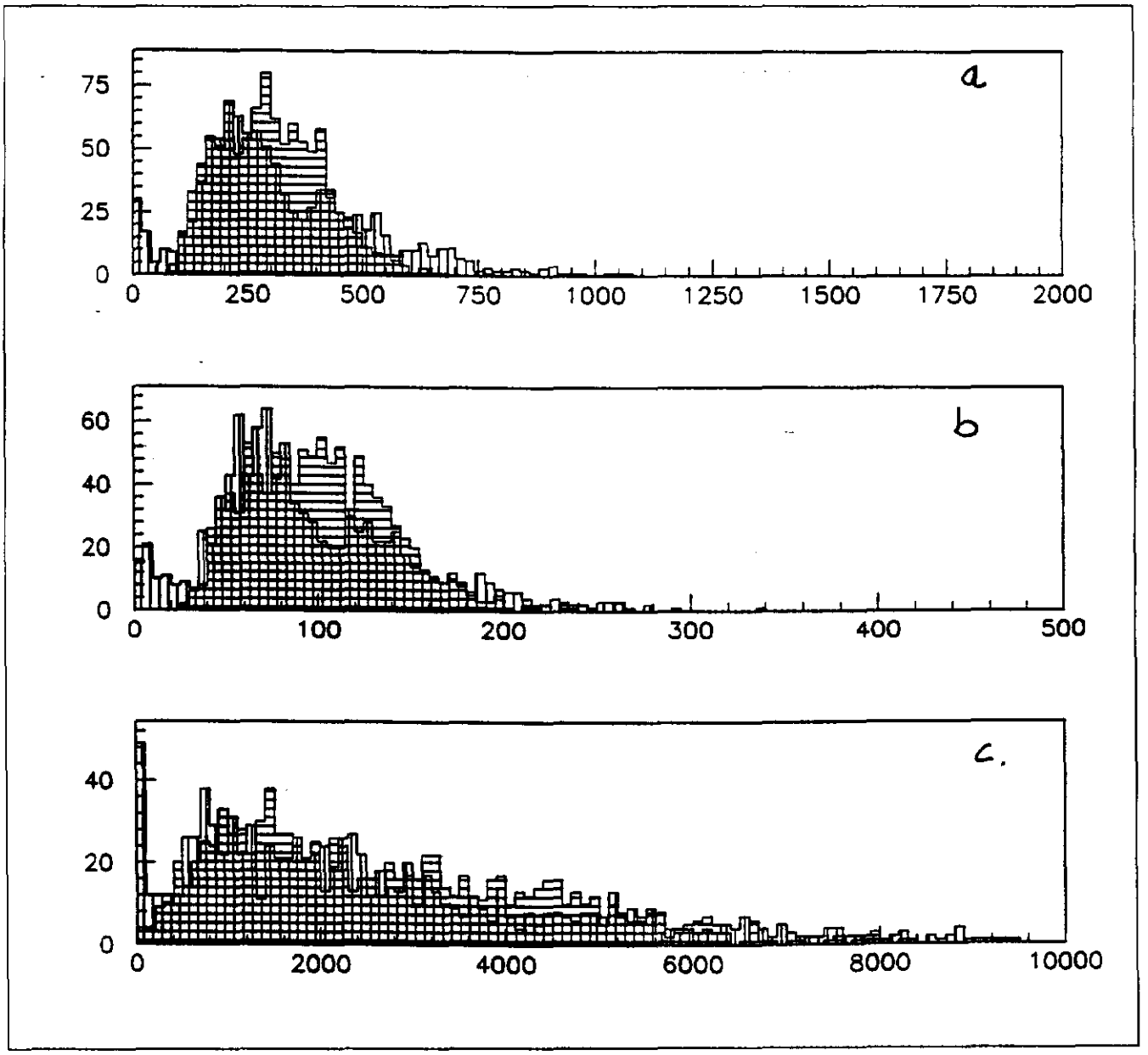

FIG. 11. Raw multiplicity distributions : (a) the number of particles considered by GEANT per event (b) the number of charged particles (c) the number of D-hits generated for the entire SVX system per event. Vertical hash lines refer to *minimum bias*, horizontal hash lines to '$B - jet$' events. The few *minimum bias* events with almost no hits are semi-elastic events with almost no tracks emerging from the beam pipe segment surrounded by the SVX silicon wafers.

III. RECONSTRUCTION ALGORITHMS AND DETECTOR PERFORMANCE.

A. Preliminary observations : Event multiplicities

Prior considering specific reconstruction algorithms, it is useful to simply histogram some of the basic quantities listed in the previous section. Of crucial importance for data acquisition issues is the number of elementary digitisations per wafer, per detector type and per event:

1. *Global multiplicities*, such as the total number of particles created at the ISAJET and at the GEANT3 tracking phase, the total number of charged tracks and the total number of D_hits produced (Fig. 11) are useful to consider. As expected, the number of D_hits is larger than the number of tracks: simple algorithms describe below will reduce this large volume of data quickly. These multiplicities are shown for '*minimum bias*' and '$B - jets$' topologies.

2. *D_hit multiplicity distributions* are presented on Fig 13 for various wafer types and locations. Table V summarizes the multiplicities at various levels: the data collector chips gather signals from 128 readout channels, next we consider the wafer level, the module level and finally the region (Central vs Forward) level. These averages can be quite large, most significant contributions coming from grazing tracks. This will be clearly established in the next section, where the properties of D_hit clusters are studied in more detail (Fig 17, 18 Fortunately, these type of D_hit clusters can be easily recognized very early in the reconstruction stage : a set of contiguous strips characterized by a relatively low detected charge, corresponding roughly to a 50 μm path length, contiguous strips clearly indicates a grazing track (Fig 10). Since the intrinsic hit resolution for these extended clusters is rather poor, as shown in the next subsection, this information will not contribute significantly in the fitting phase and can be safely disregarded by the data acquisition system, at an early stage.

3. *Detector occupancy* is defined as the probability that an arbitrarily chosen strip to be *on* in a given event. This quantity can be obtained by simply dividing the number of observed D_hits per wafer by the total number of strips on the wafer.(The charge sharing readout scheme, by virtue of the neighbouring readout, implies a correction, not worth mentioning in this context.) Fig 14 shows rather small occupancy - of the same order than current fixed target experiments, despite of the large amount of data for the whole detector.

4. *The raw detected charge distribution* for all wafers is shown for various wafer types on Fig. 15. The average charge for the wafer $DISK$ is obviously bigger than the $BARREL$ one. This is simply due to the geometrical effect described above. Clearly, large charge variations due to this geometrical effect as well as Landau fluctuation are observed for all wafer types.

   The effect of the detector noise and the Landau fluctuations can be observed independently if one selects 2.5 GeV/c muon tracks crossing the wafer at 90° (single track events, no hit confusion). They are minimum ionizing, their path length is 200 μm. The total charge associated to these perfect clusters (summed over 2 channels, at most) is shown of Fig 12. The amplifier gain has been adjusted in such a way that a 50 μm path length gives of the order of 10 counts, and can be discriminated against noise. Should the preamplifier noise be larger, one would have to give up on such signals and be able to lower the gain.

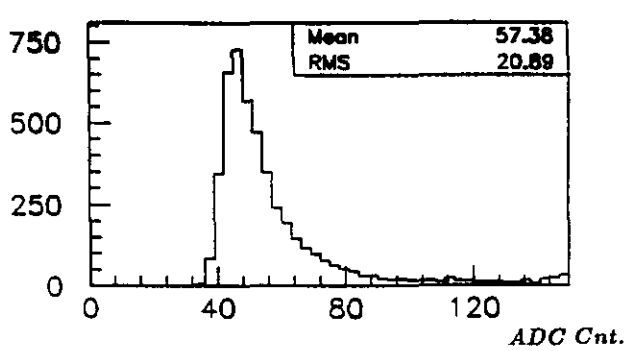

FIG. 12. The reconstructed charge spectrum for isolated clusters generated by a single 2.5 GeV/c muon at $\eta = 0$. The geometrical effects and hit confusion effects do not appear in this special sample. The average number of e-hole pairs in the wafer is about 16,000, corresponding to $\approx$ 50 channel count. The electronic noise ($\approx$ 600 electrons or *approx*1 channel) is small compared to the Landau fluctuation.s

TABLE V. D_hit multiplicities observed at various data collection levels. The data collector chips gathers 128 channels, or 256 strips. The wafer level refers to data from these chips for a given silicon wafer (at most 2×12 chips). A module consist of 12 *DISK* polygonal wafers, or, for the central modules only, 6 *BARREL* wafers. At each level, the average number of chips, wafers and modules per event (N_l) with at least one D_hit is given in the first column. Next is the average number of D_hits per chip, wafer or modules ($\langle D_h \rangle$). For each event, the maximum number of D_hits recorded by a chip, wafer or module within a given event is computed and histogrammed separately. The quantity ($\langle AM(D_h) \rangle$) is the average of these histograms, and reflects the expected *worst case* multiplicity at a given level. Wafers are subdivided in 7 categories, depending on their configuration. The indices I, M, O refer to the inside, middle and outer layers respectively, the indices C and F to the central or forward/backward rapidity regions. (see Fig 5 for geometrical description.)

ISAJET Minimum bias events ($\sqrt{s} = 2.$ TeV)

Wafer type	Data collector chip			Wafer level		
	N_l	$\langle D_h \rangle$	$\langle AM(D_h) \rangle$	N_l	$\langle D_h \rangle$	$\langle AM(D_h) \rangle$
$BARREL_I$	46	13	74	17.0	38	102
$BARREL_M$	37	5.5	19	16	12	27
$BARREL_O$	33	4.0	12.0	14	8.8	18
$DISK_{CI}$	145	3.3	12	31	14	26
$DISK_{CO}$	85	3.0	8.1	25	9.1	17
$DISK_{FI}$	176	2.8	10	57	12	26
$DISK_{FO}$	152	2.7	7.3	48	8.3	17
Wafer type	Module level			Event level		
	N_l	$\langle D_h \rangle$	$\langle AM(D_h) \rangle$	N_l	$\langle D_h \rangle$	$r.m.s.(D_h)$
$BARREL_I$	7.1	44	94	n.a.	720	500
$BARREL_M$	7.2	13	24	n.a.	186	142
$BARREL_O$	7.0	9.2	15.3	n.a.	115	85
$DISK_{CI}$	6.8	14	19	n.a.	560	393
$DISK_{CO}$	6.4	8.9	13	n.a.	300	221
$DISK_{FI}$	12	13	21	n.a.	850	470
$DISK_{FO}$	11.0	8.8	13	n.a.	520	347

ISAJET *Bjets* events ($\sqrt{s} = 2.$ TeV)

Wafer type	Data collector chip			Wafer level		
	N_l	$\langle D_h \rangle$	$\langle AM(D_h) \rangle$	N_l	$\langle D_h \rangle$	$\langle AM(D_h) \rangle$
$BARREL_I$	49	13	78	18	36	109
$BARREL_M$	42	5.2	20	18	11	28
$BARREL_O$	37	3.9	13	16	8.6	20
$DISK_{CI}$	158	3.2	12	39	13.0	29
$DISK_{CO}$	92	3.0	9.1	28	8.7	19
$DISK_{FI}$	204	2.8	12	61	10.3	28
$DISK_{FO}$	168	2.6	8.3	51	7.7	18
Wafer type	Module level			Event level		
	N_l	$\langle D_h \rangle$	$\langle AM(D_h) \rangle$	N_l	$\langle D_h \rangle$	$r.m.s.(D_h)$
$BARREL_I$	7.4	43	100	n.a.	731	380
$BARREL_M$	7.9	13	25	n.a.	195	112
$BARREL_O$	7.8	9.3	17	n.a.	128	73
$DISK_{CI}$	7.2	13	20	n.a.	369	412
$DISK_{CO}$	6.9	8.8	14	n.a.	222	202
$DISK_{FI}$	12	11.0	21	n.a.	580	490
$DISK_{FO}$	12	8.1	14	n.a.	360	300

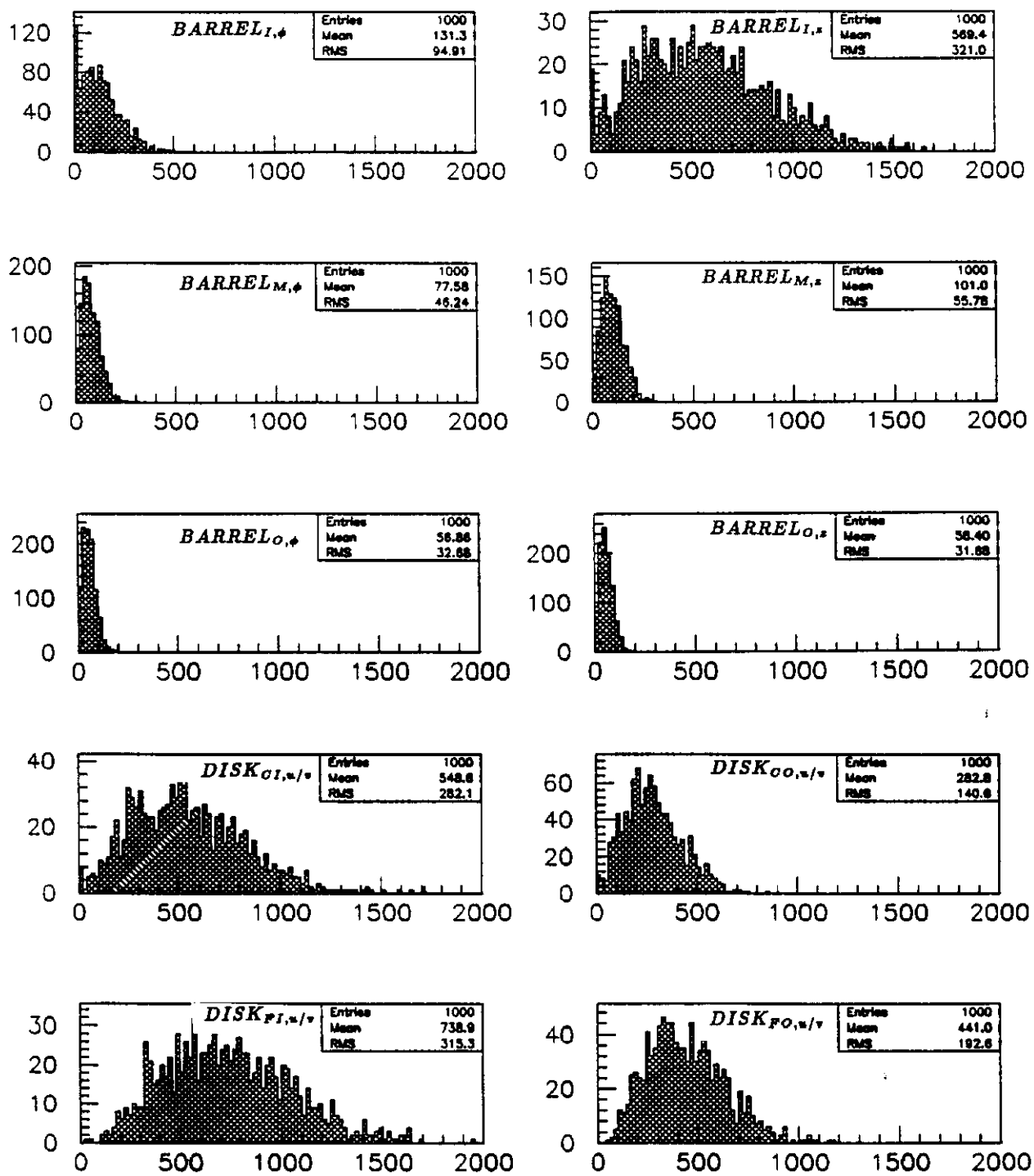

FIG. 13. The number of D_hit's recorded per wafer, for various wafer types. The event topology was '$B - jet$'. The large number of D_hit's for the inner "ϕ" Barrel wafer is mostly due to track crossing the wafer at grazing incidence. These tracks usually corresponds to moderately high rapidity ($\approx 2.$) particle emitted from a vertex located away from the central region ($Z \approx 30.$ cm). These tracks do not reach the middle $BARREL$.(see fig 5, 6).

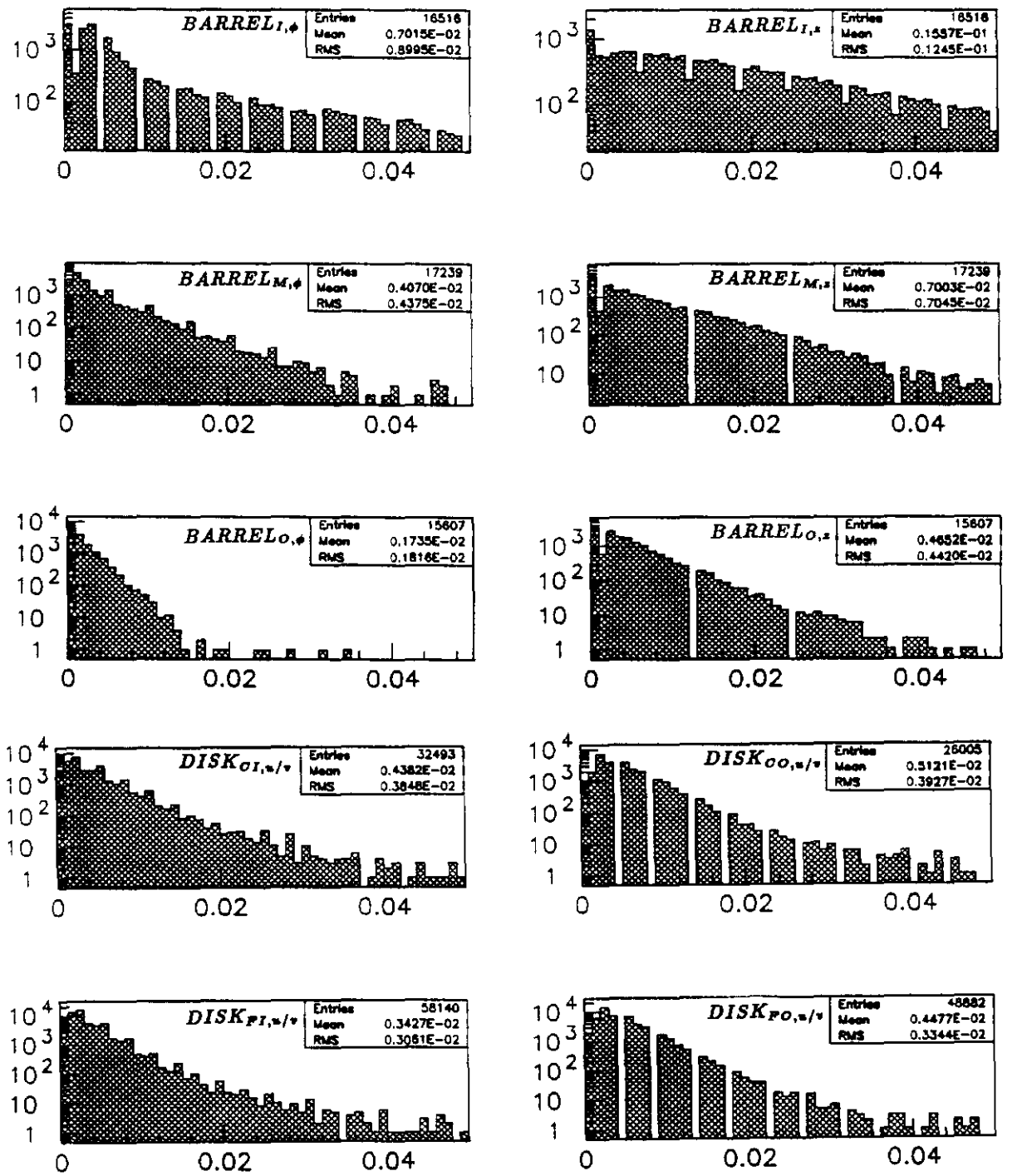

FIG. 14. The effective detector occupancy for various wafer types. Despite of the large number of hits, the relative occupancy is quite low, due to the large number of strips in the system. The event sample is the same as on fig 13. The empty bins are simply an artifact of the integer based calculation : this occupation probability (a floating point number is "quantized" by the number of channel.

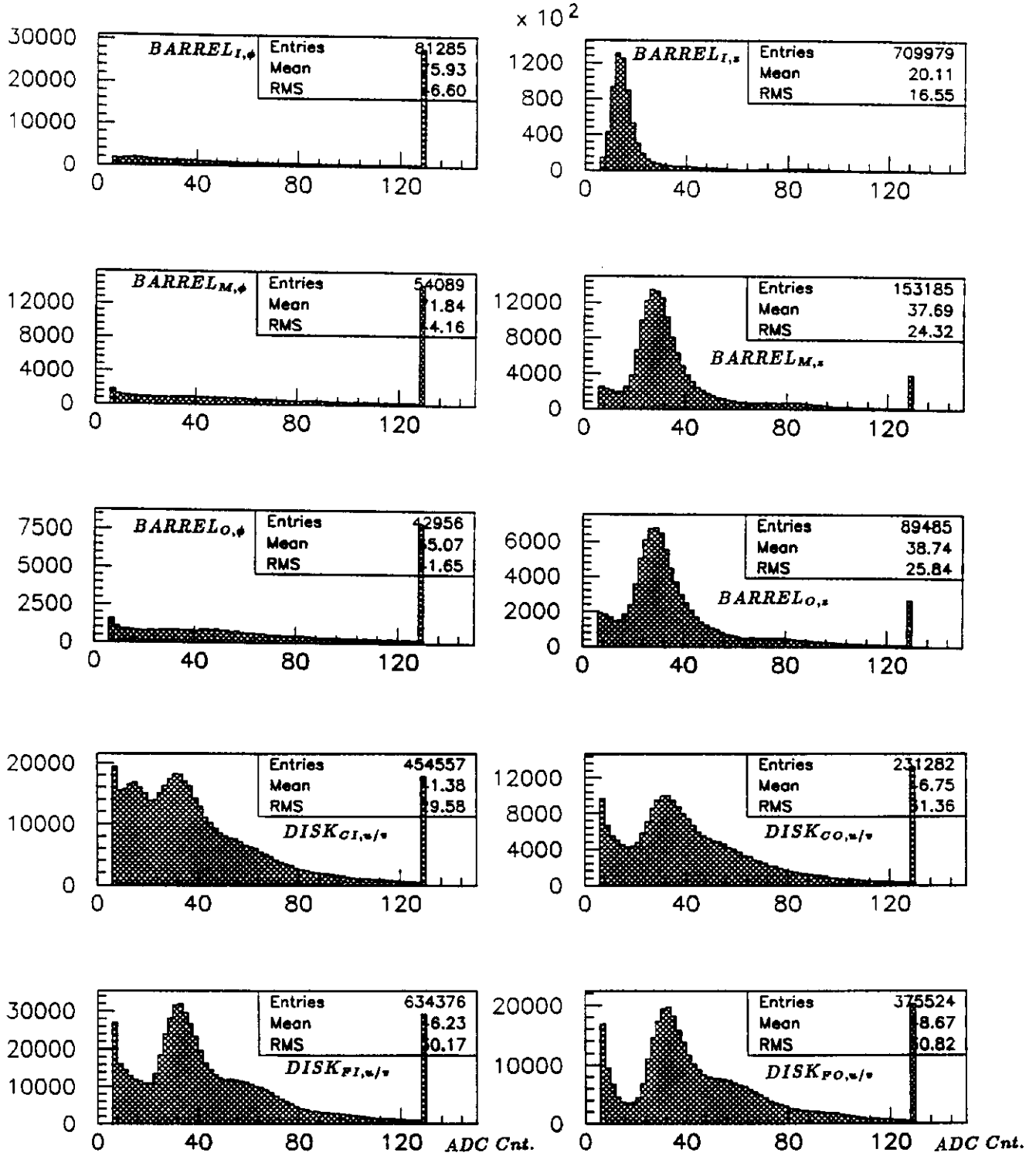

FIG. 15. The raw pulse height distribution observed for various wafer types. The event sample is the same as on fig 13. The *ADC* overflow bin is at channel 127. As expected, the grazing tracks are producing, for the "z" side, a large amount of individual signals characterized by a small pulse height and, for the "ϕ" side, fewer channels with relatively large pulse height. Since the rapidity distribution is rather flat, the ϕ path length distribution is rather flat as well, hence the pulse height is also flat. As consequence, the a relatively large dynamical range for the amplifier and the *ADC* is required.

B. The Cluster Level: The Hit to Track Assignment and Spatial Resolution at the Wafer

The reconstruction algorithms discussed in this analysis have been designed to work on real data. This means that the Monte-Carlo information, such as the track identity assigned to a given D_hit, is not used at the reconstruction stage but exclusively for debugging purposes. The raw data structures (D_hits) and the geometry database are used in the reconstruction package, while the Monte-Carlo information is to be used for computing acceptances.

The central tacking system (referred as the *STRAW* system) has been designed to perform the primordial pattern recognition. The *STRAW* system provides a large number of hit per track. In addition, its long lever arm allows accurate determination of the momenta [1]. The *SVX* detector acts as a vernier with respect to the *STRAW* system : the *SVX* refines the track parameters at the vertex. As shown in the last subsection, stand-alone *SVX* reconstruction algorithms do have serious deficiencies.

In any event, the first step is simply to *cluster* D_hits together, ignoring any kinematical or tracking information.

1. From a sequence of D_hits to a cluster.

A cluster is defined as a ensemble of contiguous D_hits. Hopefully, all D_hits associated to a given cluster have produced by one and only one track crossing the detector plane. By contiguous, one means that the number of 'blank' strips between 2 strips above threshold, within the cluster, is less than or equal to four strips, corresponding to 2 readout channels. This reconstruction parameter needs to be tuned with respect to preamplifier noise or event multiplicities in order to reduce the probability of either splitting a real cluster or lumping to independent tracks together. The *cluster position* of the cluster is currently simply a charge weighted average, if the number of strips in the cluster is less or equal to six. For extended clusters, this cluster position is defined as the geometrical average between the entrance and exit positions, themselves defined by the starting and ending strip locations. The value of this algorithm with respect to the weighted average one depends crucially on the signal to noise ratio of the detector. In addition to this position (expressed in strip units), the following information is kept for each cluster on each wafer:

- The error on the cluster position. This is yet to be defined properly, based on real data. For now, the error for narrow clusters is set to $1./\sqrt{12.}$, for extended clusters, $\sqrt{2.}/\sqrt{12.}$.
- The sequential number of the first strip in the cluster and the number of strips included.
- The average charge in the cluster.
- The *r.m.s.* on the previous quantity. In principle, for extended clusters, this can be useful to determine the cluster self-consistency : an extended cluster should be characterized by a relatively small *r.m.s.* since most of the strips have small charge.
- An integer number pointing to the *DIGI* structure, to be used in cluster validation studies (the *DIGI* structure itself points to the *KINE* structure).

Provision has been made to accommodate for *second generation* clusters, i. e., if a few strips in an extended cluster have a relatively large amount of charge compared to the average in the cluster, it is assumed that these few strips can be associated to a different track in the event, and are *confused* with the first generation cluster. Again, the usefulness of such an algorithm depends critically on the preamplifier noise level.

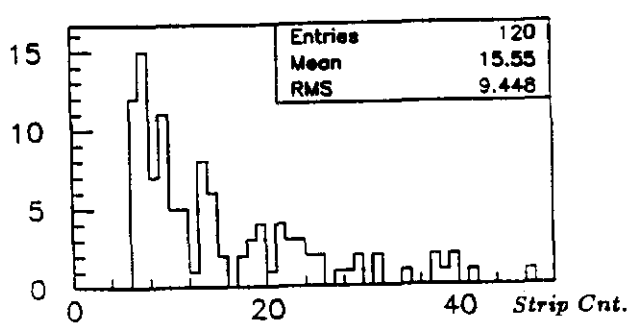

FIG. 16. The outer *BARREL* distance in the expressed in strip counts between 2 clusters generated by gamma conversions occuring in the inner layer. Only one cluster is observed in the ineer layer for most of those events. This unique topology could be used to distinguish between prompt isolated electrons and background conversions.

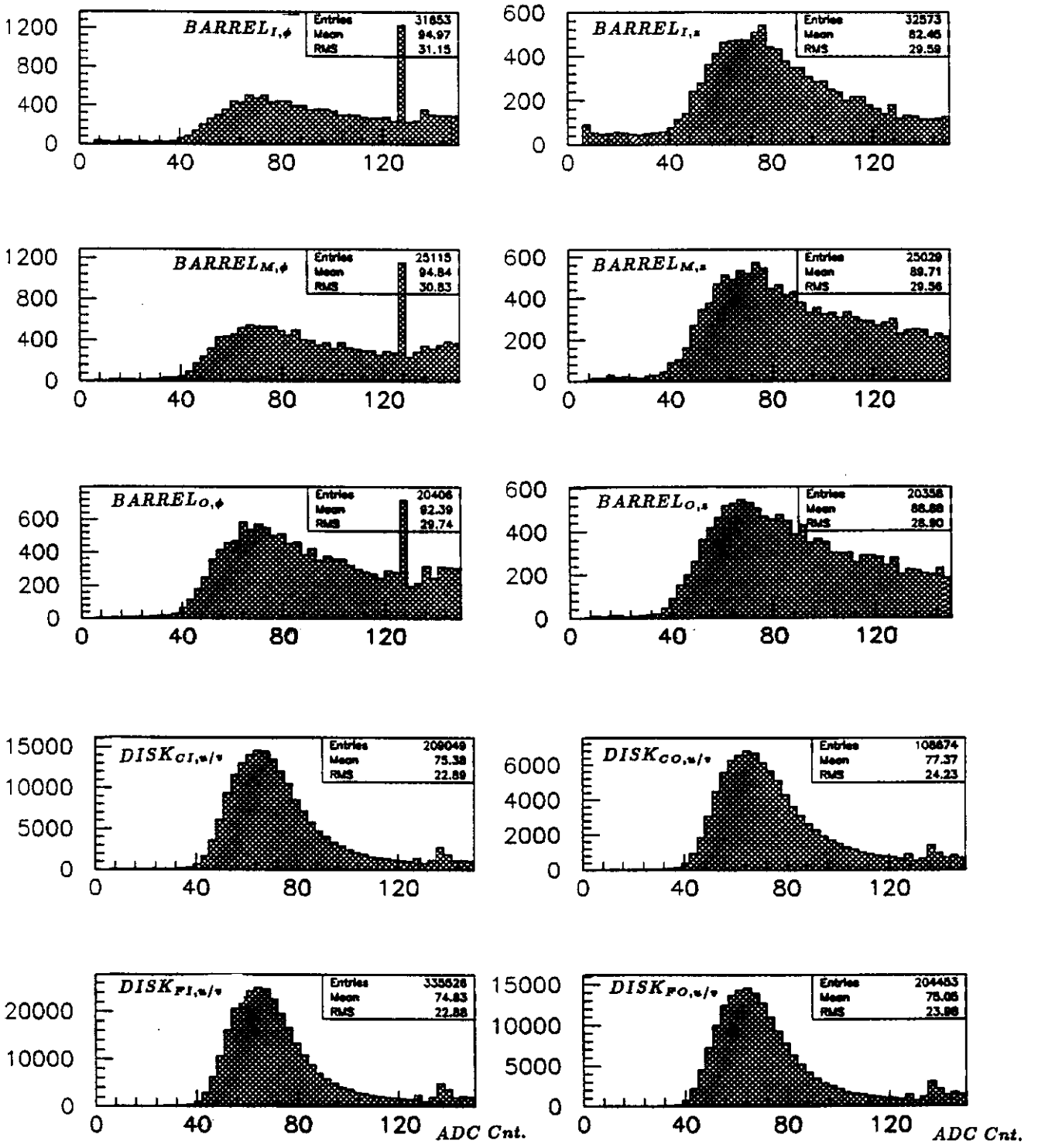

FIG. 17. The reconstructed pulse height distribution observed for various wafer types. Contrary to the figure 15, each entry in these histogram corresponds to a cluster and not a single D_hit. The event sample is the same as on fig 13. As expected, the ϕ and z distributions become similar.

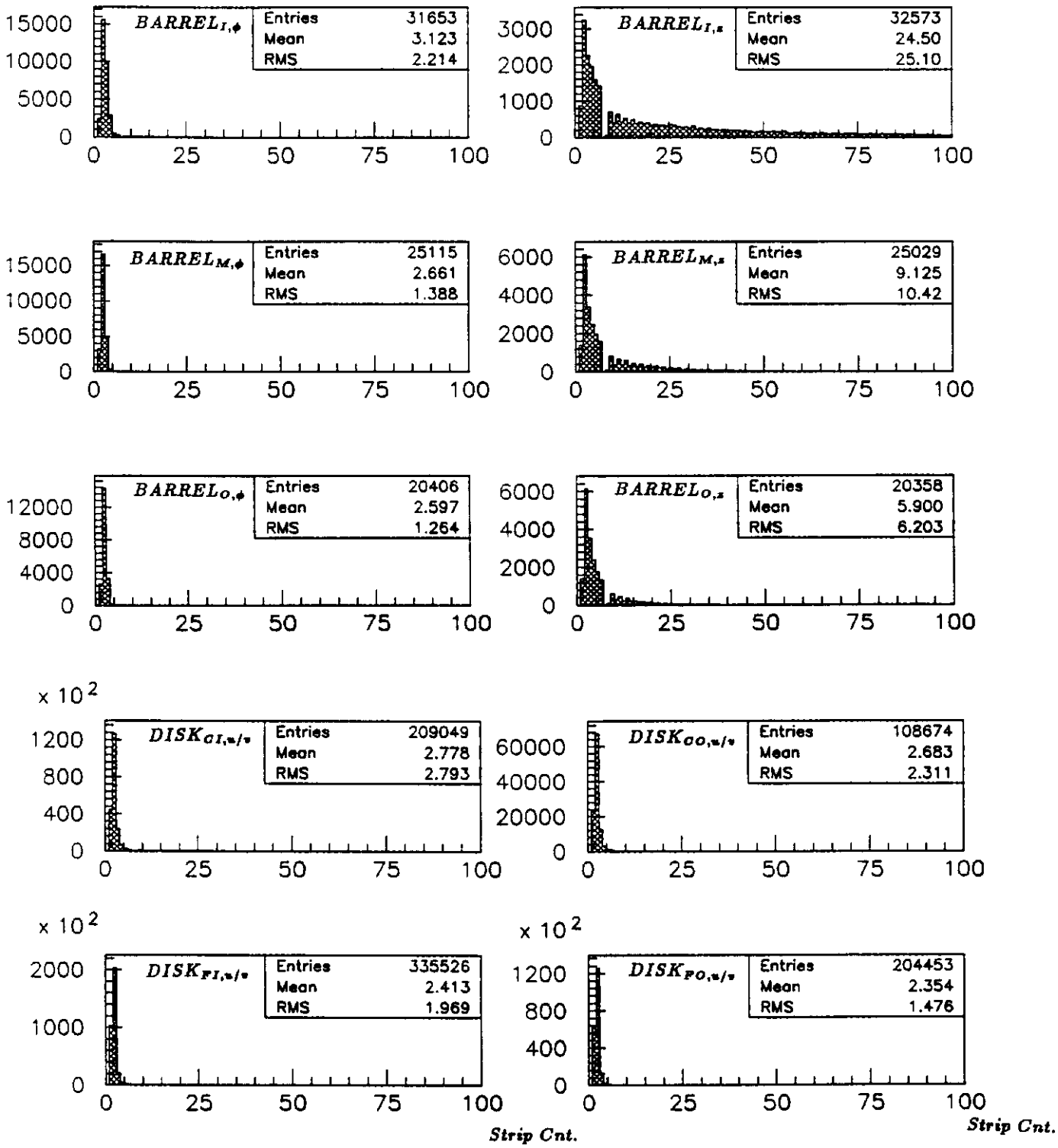

FIG. 18. The reconstructed cluster width, expressed in strip counts, for various wafer types. The event sample is the same as on fig 13. As expected, the ϕ clusters are much wider than the Z one. The gap in Z distribution is an artifact of the reconstruction algorithm.

A distinctive type of cluster can be generated by photon conversions occurring either in the beam pipe or in the silicon itself. Most of the background for relatively low P_t electrons trigger comes from such conversions. A careful analysis of the SVX data along the path of the electron permits to distinguish between isolated leptons issued from the collision and these conversions, which are characterized by either:

- A single isolated cluster, with a total charge between 2 and 3 times the charge corresponding to a single isolated particles. Given the amplifier gain mentioned above and the limited range of the *ADC* (7 bits), this corresponds most of the time to a saturated *ADC* count !
- Two clusters, each of them characterized by a charge above minimum ionizing, and separated only by a few hundred microns. This separation is entirely due to the magnetic field and is therefore momentum dependent.

This has been observed in a dedicated simulation run, where 10^5 2.5 GeV gammas were thrown at 90°. The azimuthal angle was chosen to maximize the deflection in the magnetic field. The inner *BARREL* detected 318 isolated clusters (that is, .3 % conversion probability), the middle *BARREL* detected 609 isolated clusters, the outer *BARREL* 814. Most of these clusters were characterized a completely saturated *ADC* count. In the middle (outer) layer, only 8 (60) events had 2 clusters respectively. The separation between these clusters (in strip count) is shown on Fig 16. Clearly, these pairs are due to conversions in the inner layer.

2. *The Cluster to Track Assignment*

Clusters have been studied with respect to GEANT hits or original tracks from the *KINE* structure. In principle, this could have been done for any hits, created by 'relevant' tracks (originated from the primary vertex or heavy quark decays), or irrelevant ones (Compton electrons, secondary interactions and so forth). In order to filter these hits, one has first to be able to associate them to relevant tracks. As mentioned earlier, relevant tracks are defined and measured either by a stand-alone SVX tracking code, or by the STRAW tracking system. Neither algorithm was available when this project started. Therefore, the only reasonable approach was to start from the GEANT *KINE* structure itself. Clearly, this swindle will be avoided in future versions of the integrated BCD software. The following selection criteria were applied to all *KINE* tracks :

- Only the following particles were considered : e^-, e^+, μ^-, μ^+, π^-, π^+, K^-, K^+, proton and antiprotons.
- $P_t \geq 0.1$ GeV/c
- $-4.0 \leq \eta \leq 4.0$
- The track comes either the primary vertex or a secondary vertex due to Beauty, Charm or other weak decays occurring within the beam pipe. Conversions and other secondaries produced in the beam pipe or the silicon wafers were ignored. The D_hits produced by these background tracks is certainly present in the simulation and indirectly affects the resolution. But it is anticipated that these tracks can be easily identified and declared irrelevant at the vertex level.

Based on this sample, a set of 'pseudo' STRAW tracks was created. The track parameter were smeared to take into account the finite resolution of the STRAW tracking system. It is anticipated that such a tracking system has a individual hit resolution approaching 50 μm [7]. Such a tracking system should be able to achieve of the order of 100 μm accuracy at the vertex, neglecting multiple scattering effects. Therefore, the *KINE* tracks position at the primary vertex was smeared in X and Y assuming a Gaussian resolution, with a sigma (σ_{straw}) left as a tunable quantity, ranging from 50 to 200 μm. Provision has been made in the code to also smear the track angles, although a realistic STRAW track fitting algorithm will correlate the position and angular resolution at the vertex. This information being unavailable, the implementation of the full covariance matrix of these tracks at the vertex has been postponed and tracks are currently smeared only in X and Y position at the vertex.

A given tracks will traverse few or many wafers, depending on track kinematics as well as the primary vertex position. As expected, most of the data comes from *DISK* wafers (Fig. 19). For each pseudo-straw track, at each wafer crossed by the track, the following information is computed and saved in a stand-alone data structure :

- The wafer type, and its unique address in the SVX hierarchical volume structure.
- The X, Y, Z location of the track in the middle of the wafer. It is assumed that the track is a straight line within the thickness of the wafer.

- The direction cosinus of the track ($1/P \times \partial P_x/\partial x$, $1/P \times \partial P_y/\partial y$, $1/P \times \partial P_z/\partial z$)
- The predicted errors projected on the U, V, ϕ or Z axis were used to establish a search window to match reconstructed track_hits to clusters, as well as in the SVX track fitting phase.
- For each side of the wafer, the predicted U and V (or ϕ and Z) cluster locations, expressed in strip units.
- The U / V (or ϕ, Z) search window width, currently set to 3 times the estimated position error.

Correct estimation of these predicted errors is crucial, as shown later in the track fitting and vertex measurements. These errors depend on σ_{straw} as well as the uncertainty due to multiple scattering. These two sources of uncertainty (STRAW resolution and multiple scattering) are independent and can be added in quadrature. The term due to multiple scattering can be estimated starting from the vertex going outward towards the gutter, or vise versa, starting from the gutter towards the vertex. The former calculation should be used in the fit, since the track parameters must be estimated at the vertex. In the latter case, the error for the outer layer is small and increases as the track propagates inward. This algorithm could be used to refine the search window for the outer layers. This will be postponed until further versions, when more knowledge on STRAW tracks is available. Finally, since the 'hit to track' algorithm worked on a per wafer basis, the multiple scattering error is compute independently for each wafer, neglecting obvious correlations in these errors. To summarize, one can identify 4 distinct components to the position resolution at the wafer. The first two of them are used in establishing the search window, the last one is entirely ignored at this stage :

- σ_{straw}, of the order of 100 μm.
- the multiple scattering, ranging from a few micron to a few hundred micron, depending on the location and the momentum
- The intrinsic detector resolution, depending of the strip pitch, the signal to noise of the electronic noise and therefore the track angle. This resolution range from 10 to 15 μ for a 25 μ pitch [8].
- The random, non Gaussian, contribution due to hit confusion due to spectator tracks.

Through the cluster to track matching process, these effects can be studied quantitatively. The information to check the result has been saved: since the STRAW tracks have been build from the $KINE$ structure, the cluster d/s points to D_hits d/s which themselves points to the same $KINE$ structure. Prior to final checks performed in the SVX track fitting procedure, there is a small but finite probability of association a given track_hit to more then one cluster. This probability is related to the *hit confusion* probability described in the introduction. Table VI summarizes these probabilities as a function of event topology and simulation conditions. This hit confusion probability for the worst case is shown on Fig 24 as a function of the strip length. This curve has been obtained by creating in the analysis phase pseudo "short strips" of variable length and by assessing the level of confusion within these short strips. To first order, the hit confusion probability is directly proportional to the raw event multiplicity. Unfortunately, this means that the probability to find a confused track in the event goes quadratically with the event multiplicity. A correct estimation of this multiplicity for low P_t B events becomes important if one wants to reduce detector cost while keeping good vertex detection. The effective position resolution at the wafer is affected by these pattern recognition failures, as shown below.

The efficiency of this matching procedure has been studied. Two indepedent sources of inefficiency can distinguished easily : either the cluster is simply missing, or is outside the search window. The former case of the happens very rarely, because of the low D_hit discriminator level with respect to the signal. The latter case can be corrected by hunting for the closest cluster, i.e., by opening the searching beyond the 3 σ level. The hit confusion probability is proportional to the width of this search window, the background will therefore rise. Recovering a few % of inefficiency is not necessarily the best choice, considering the number of measurements available (Fig. 19).

The difference between the predicted cluster position and the observed one relates directly to the *effective* or *practical* resolution. If more than one cluster was found within the search window, only the closest one is considered on these figures. This measured resolution can also be compared to the 'normalised' one, where the difference (predicted - observed) is divided by the error on this quantity. These quantities are displayed on Fig 20, 21, 22 for $B - jet$ events. In order to measure the *best possible* SVX detector resolution, σ_{straw} has been set to 0. Large variations from wafer to wafer are expected due to multiple scattering. Most crucial is the resolution at the first wafer, where multiple scattering can be neglected because of the close proximity of the wafer with respect to the beam pipe (Fig 21).

An other effect mentioned earlier is the angle of incidence of the track with respect to the wafer. This effect is particularly important for 'z' *BARREL* strips (Fig 22). Finally, the loss of resolution due to pattern recognition failure can be estimated by comparing results from single μ events to $B-jets$ events. These μ tracks were generated at a moderate P_t of 1.0 GeV/c, and can be directly compared to generic track from the $B-jets$ sample. Non Gaussian tails are observed for $B-jets$ (see fig 23), for all wafer types. These pattern recognitions failures -in which the closest cluster is the wrong one, or is contaminated by a spectator track- worsen the resolution as does the multiple scattering: these two effects are indistinguishable in most cases. (Fig 21, 23)

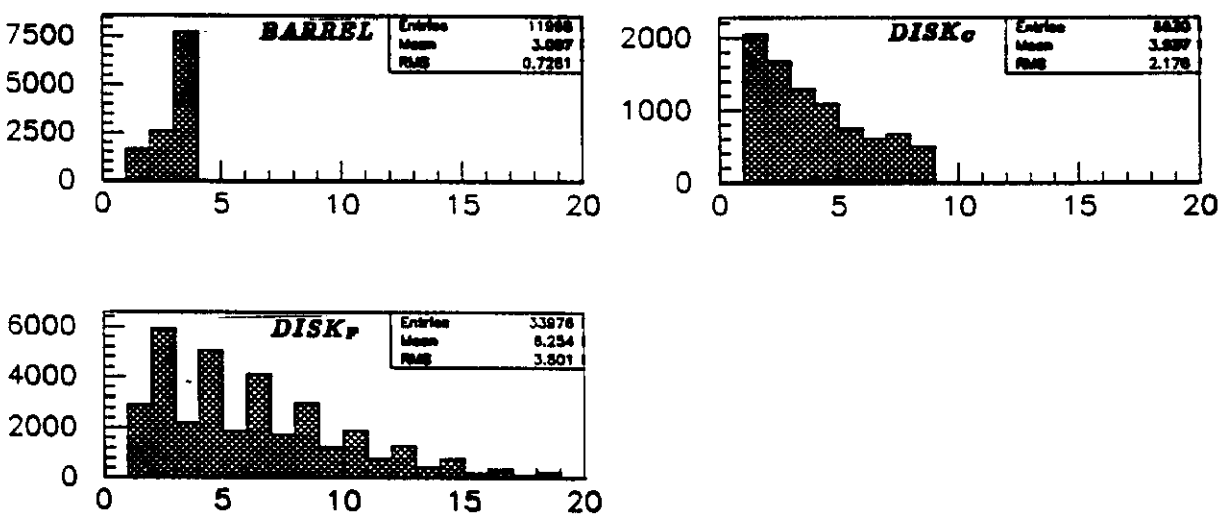

FIG. 19. The number of encountered wafers per tracks for *BARREL*, central and forward/backward *DISK* wafer types. The event topology was $B-jets$, $\sqrt{s}=2.0$ TeV.

TABLE VI. Hit confusion probabilities for all wafer types and strip stereoangles. For *DISK* wafers, *U* and *V* obviously gave the same results. For *BARREL* wafers, the 'ϕ' strips measure approximately the asimuthal angle ϕ at a fixed radius, therefore the strips are oriented parallel to the beam. The 'z' strips are perpendicular to the beam axis. The condition labeled 'sec' ('no_sec') refers to a simulation run where gamma conversions or hadron interactions were allowed to take place in the detector material, but the secondary particles were tracked (disregarded).

Physics Condition -	*BARREL*, ϕ strips (%)	*BARREL*, z strips (%)	*DISK*, Central (%)	*DISK* forw/back (%)
	Minimum bias events			
$B=1.$ Tesla, 'sec', $\sigma_{straw}=0.$	1.3	2.2	7.8	8.3
$B=0.$ Tesla, 'sec', $\sigma_{straw}=0.$	0.9	2.5	5.9	5.8
	$B-jet$ events			
$B=1.$ Tesla, 'sec', $\sigma_{straw}=0.$	1.1	1.6	4.8	4.1
$B=1.$ Tesla, 'no_sec', $\sigma_{straw}=0.$	1.0	1.3	4.3	3.8
$B=1.$ Tesla, 'sec', $\sigma_{straw}=50.\mu m$	1.3	2.3	5.0	4.4
$B=1.$ Tesla, 'sec', $\sigma_{straw}=100.\mu m$	2.1	3.0	5.7	4.9
$B=1.$ Tesla, 'sec', $\sigma_{straw}=200.\mu m$	3.8	4.5	7.3	6.3

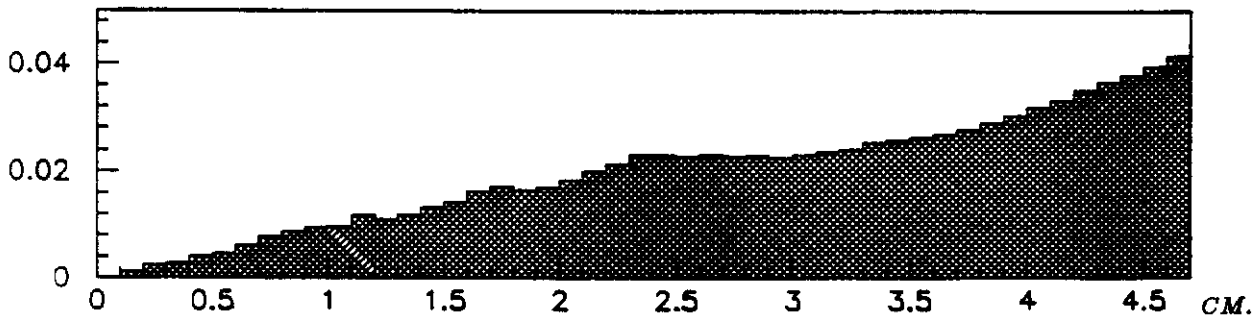

FIG. 20. Hit confusion probability for the *BARREL* 'ϕ' strips as a function of strip length for $B - jet$ events. Little track to track correlation is observed, since this probability rises almost linearly with the strip length.

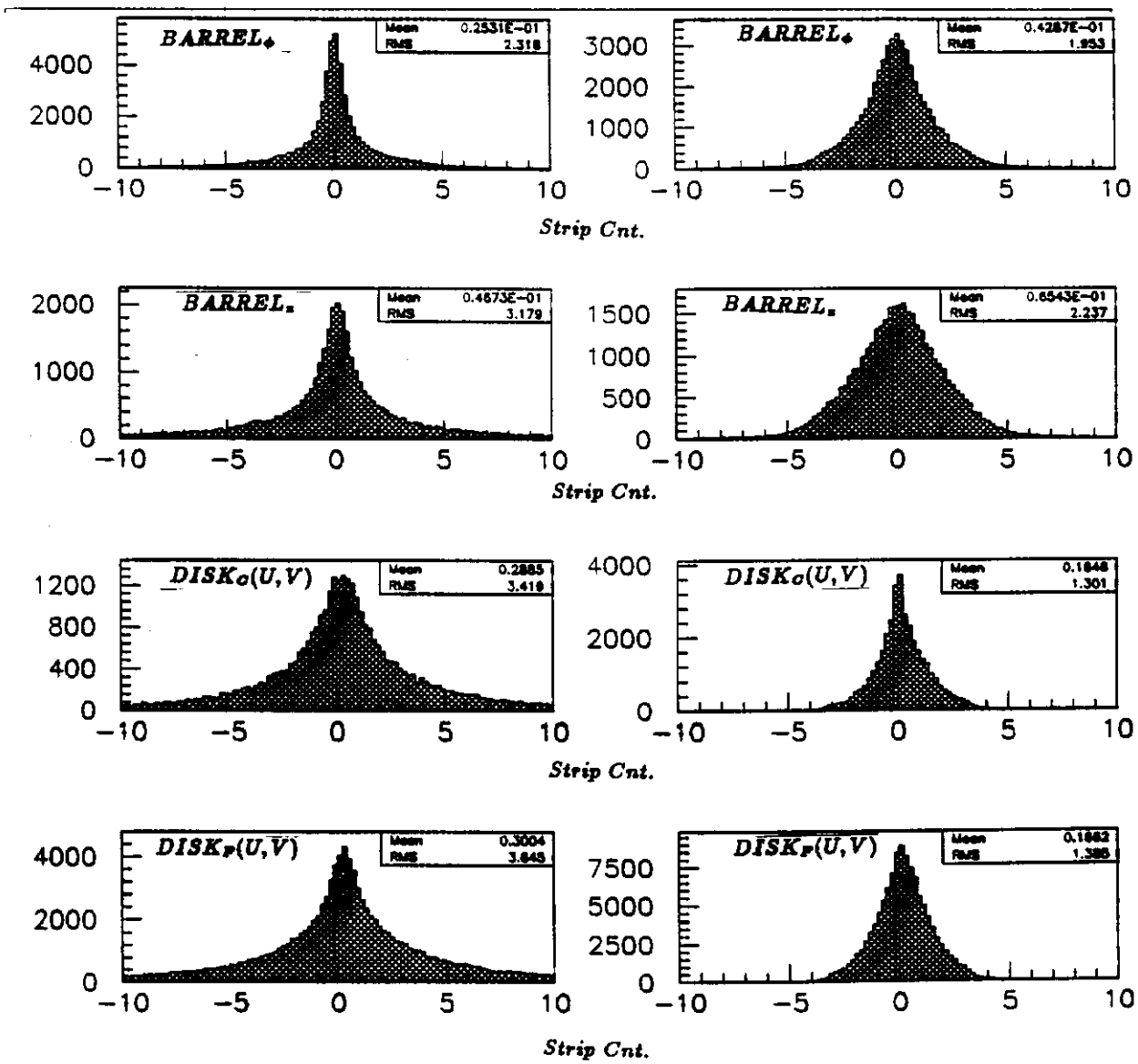

FIG. 21. Effective position resolution at the wafer, for four classes of strips. On the left hand side of the page, the difference predicted - observed is expressed in strips units. On the right hand side, this difference has been divided by the predicted position error. Multiple scattering, angle of incidence, hit confusion and intrinsic strip resolution contributes to the worsening resolution. All wafers on the tracks are included eliminate STRAW tracking uncertainties, $\sigma_{STRAW} = 0$. Unfortunately, significant non-gaussian tails must be taken into account.

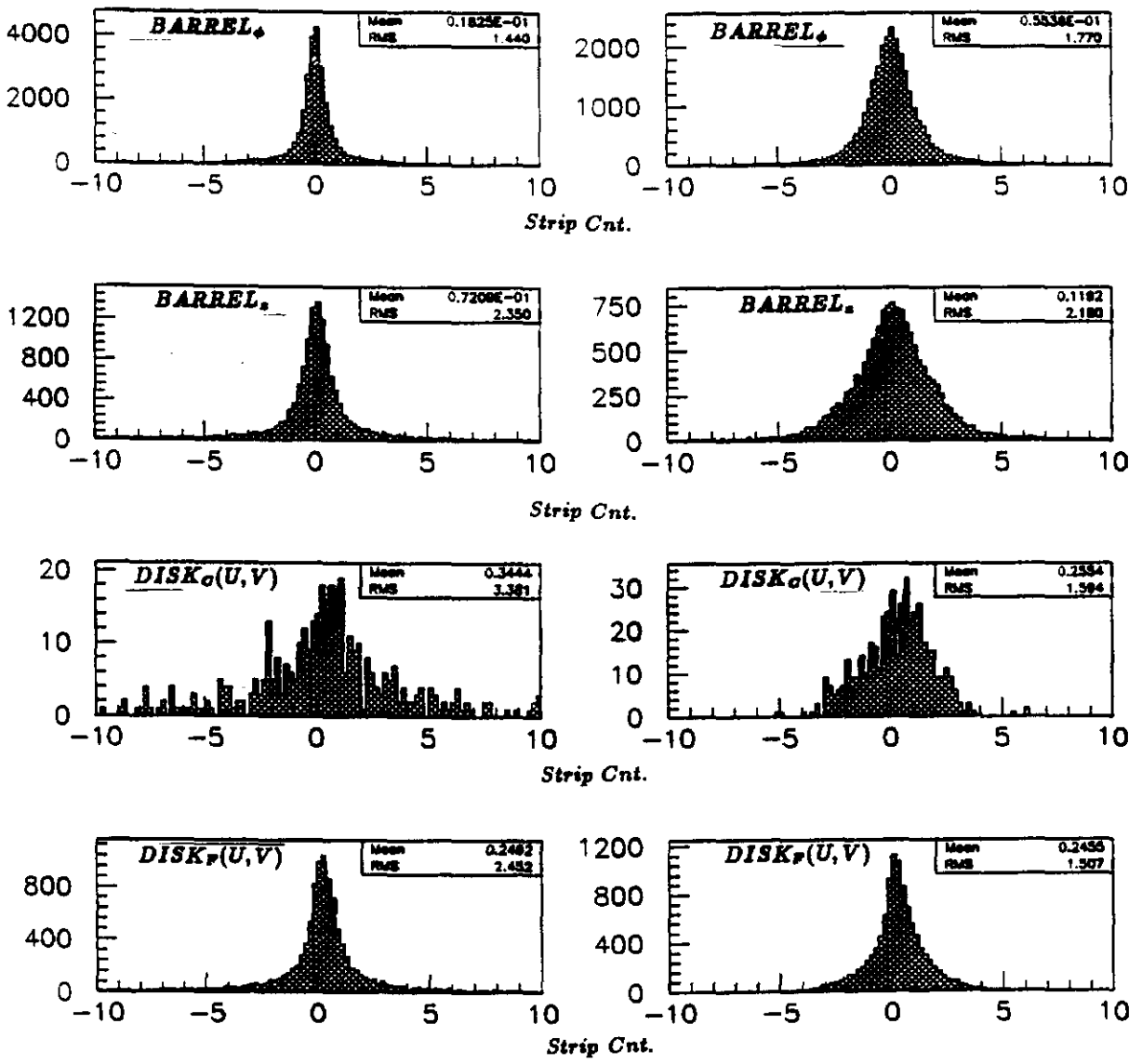

FIG. 21. Effective position resolution at the wafer for four classes of strips. Conditions are identical to Fig 20, but only the first wafer on the track (starting from the vertex) is included.

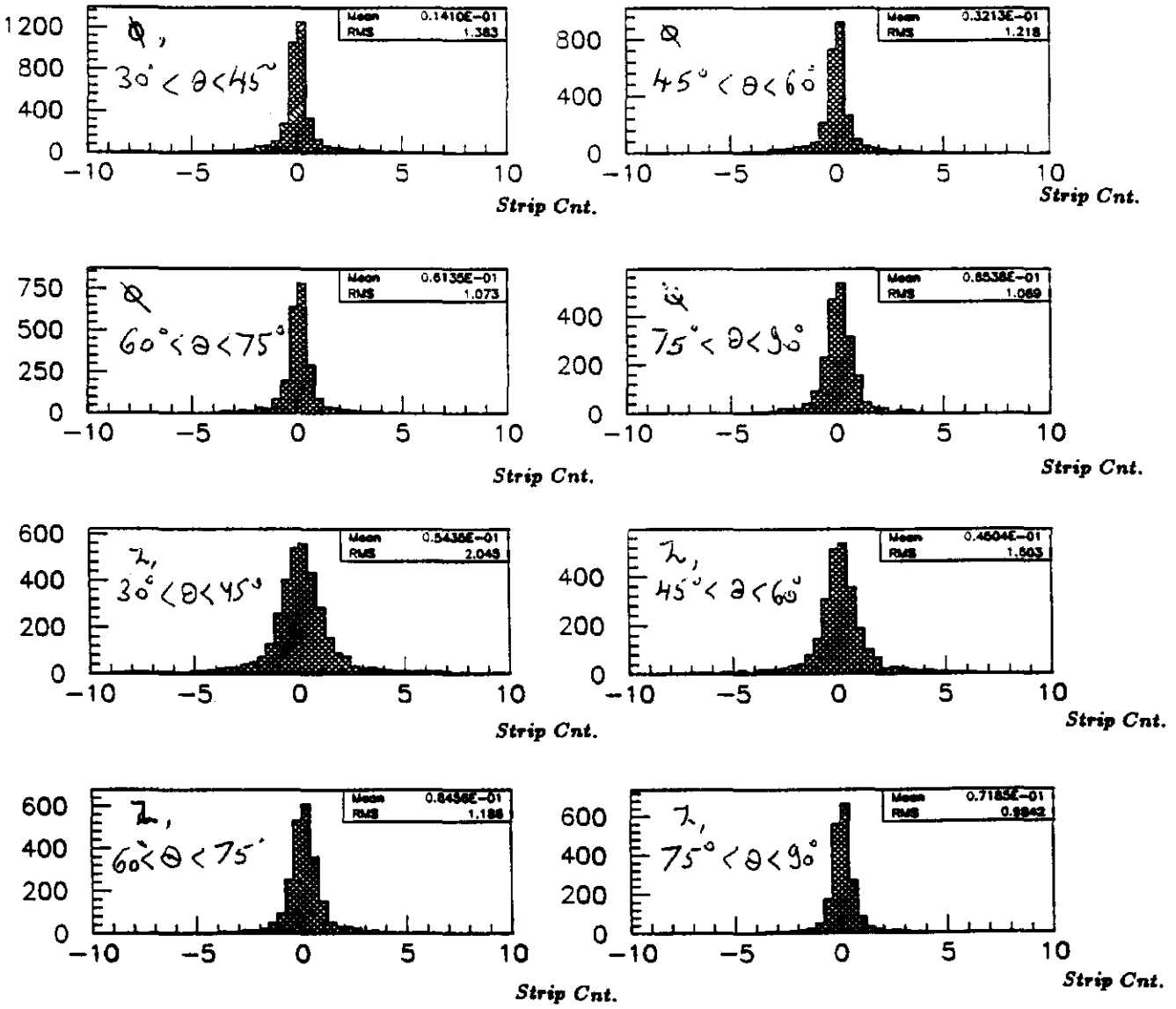

FIG. 22. Effective position resolution at the wafer at a function of the direction cosinus along the $z$axis ($1/P \times \partial P/\partial z$) for the *BARREL* wafers. As expected, the z resolution becomes worse at small angle, because the width of these cluster increases at the angle decreases (Fig 18). As on fig 21, only the first wafers on the track are considered. Only the position differences (in strip units) are plotted.

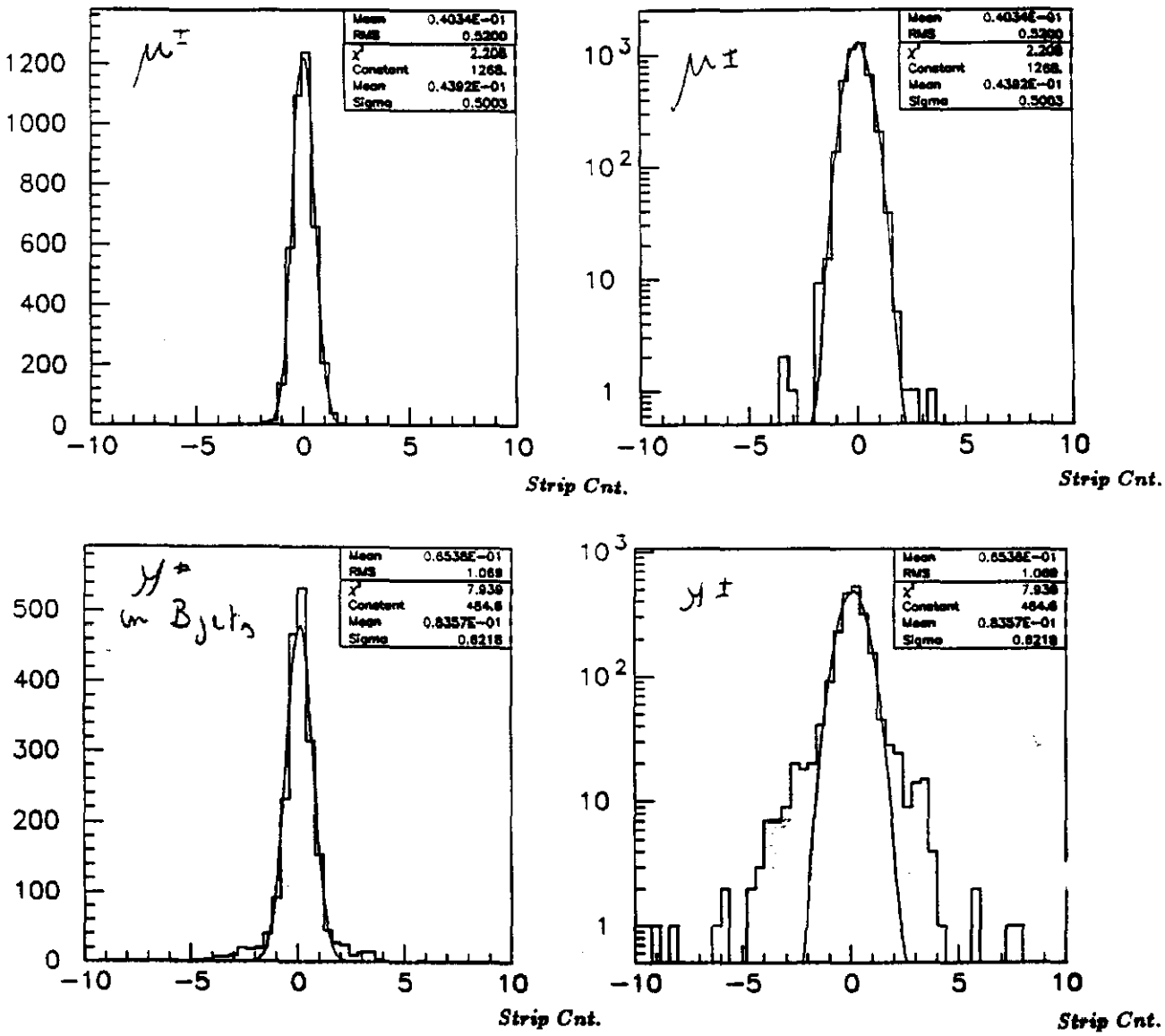

FIG. 23. Gaussian fits to the effective position resolution for the $BARREL_\phi$ strips. Tracks at grazing incidence have been rejected ($75° \leq \theta_z \leq 90°$). Results are shown for single μ track events and generic π tracks in $B - jets$ events.

C. Track Fitting and Spatial Resolution at the Vertex.

SVX tracks now can be defined as a sequence of matched clusters. These clusters can be fitted to the relevant track model. A simple straight line fit was used in the absence of the magnetic field, while a helix had to be used in the dipole field case. At low momentum, this helix can not be approximated to a simple parabola, given the relatively high field required to achieve a good mass resolution over a wide rapidity gap. Setting B to 1 Tesla, at $P \approx 0.5$ GeV/c a track will rotate by $\theta_r \approx 300.$ mrad. over a distance $\Delta l \approx 50cm.$, with a corresponding radius R of 167. cm. Hence, the deviation from a quadratic approximation is :

$$\Delta l \times (\sin\theta_r - \theta_r) \approx 2mm.$$

$$\Delta l \times (\cos\theta_r - (1. - \theta_r^2/2.)) \approx 300\mu$$

Also, the motion parallel to the field (y axis) is coupled to the motion in the bend plane ($x - z$ plane). For a fixed Δz (or Δx) and given the momentum P, finding Δy always comes down to resolving nonlinear equations of the type :

$$\Delta y = cst_1 \times \tau$$

$$\Delta x = cst_2 \times \tau + cst_3 \times \sin(\omega \times \tau)$$

In addition, because of the different orientations of the wafer planes ($BARREL$ versus $DISK$) and the different stereoangles for the $DISK$ wafers, the coordinates x, y or z are not measured independently. The nonlinear character of the track model and this *mixed coordinate* system for the input data impose some mathematical complications on the fitting procedure. A linear model fit can be resolved in such a mixed coordinate system easily through a rather straightforward matrix inversion. It is not so simple for the helix fit in our system.

A 'pseudo-fit' algorithm was developed based on the mixed coordinate, linear, model :

- The momentum of the track is not measured by the SVX detector, but by the STRAW tracking system. Although the amount of material within the SVX detector can seriously change the direction cosinus of the track, the momentum remains essentially unaffected. Since the STRAW system has better angular resolution than the SVX, it does make sense to neglect the error in the momentum while fitting the SVX tracks.

- Based on 2 wafers, a preliminary value for the four remaining SVX track parameters can be determined. Track parameters are expressed at the primary vertex location. Since this vertex can not be computed accurately without SVX tracks, a crude primary vertex from the STRAW tracks is used. Here again, we had to rely on the GEANT vertex. This is not a cheat, since it is merely a convenient coordinate transformation. At this point, The following track parametrisation was chosen, primarily to ease to the vertex fitting procedure :

  - x_0, the track intercept on the x axis at the z location of this preliminary vertex
  - $x' = \partial x/\partial z$, the 'slope' on the x axis.
  - y_0, the track intercept on the y axis at the same z location
  - $y' = \partial y/\partial z$, the 'slope' on the y axis.

- At each measurement, the differences between the measured position and the track position based on these preliminary track parameters were computed using the exact helix equations, while the derivatives of these quantities with respect to the track parameters were estimated numerically based on the STRAW track parameters. The intuitive justification for this unorthodox method is the following : essentially, we are dealing with a linear fit, but the corrections to this linear fit while estimating the track deviations must be computed quite accurately. In order to avoid wild fluctuation due to poor measurements, $BARREL$ z-hits matched with a grazing track ($\theta \leq 30°$) were rejected. Also, if a measurement was more than 5 σ away from the final fitted track, the fitting had to be done again, ignoring this measurement. Thus, this algorithm has the capability of rejecting a *confused* cluster and try the *next best* one.

As usual, the effective resolution is defined as the difference between the parameter obtained with this analysis and the corresponding parameter deduced directly from the $KINE$ d/s. The accuracy of this fitting procedure can be determined by simply comparing the resolution obtained with the exact linear fit (where tracks were generated without magnetic field) with the pseudo fit one. In order to simplify this comparison, single muon track events were used (Fig. 26, 27).

The effective track resolution at the vertex, for multiple track events ($B - jet$ topology) is likely to depend on the track topology, i.e., on the number and respective locations of the measurements on which the fit is based. This number varies widely, as low momentum tracks can be deflected either outside or inside the SVX hexagonal gutter(Fig 25). The effective x_0 resolution is shown as a function of the number of degrees of freedom in the fit (Fig 29) and as a function of the track momentum, for single muon tracks as well as $B - jets$ events (Fig 30, 31). This resolution does not improve as the number of measurements exceeds 6 or so, simply because the error on these measurements becomes large as the multiple scattering uncertainties becomes dominant. Because of the various effects, the track resolution at the vertex can not be summarized by a single number: although resolutions of 30 μm can be obtained, some 'bad luck' track topologies are characterized by much worse resolution. As a consequence, correct error matrices describing individual track fits must be used in the vertex fit.

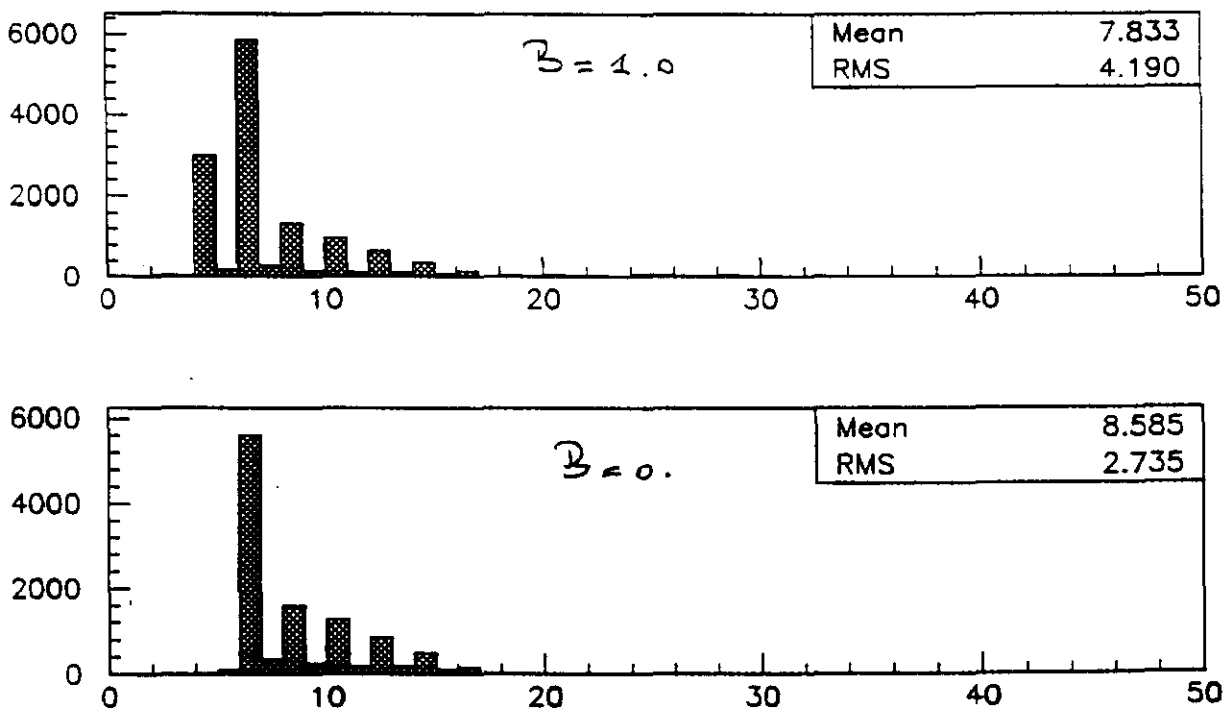

FIG. 25. Number of degrees measurements used in the fit for these muon events, using the *pseudo fit* with the field is turned on ($B = 1.0$ Tesla, top window) and using the linear model with the field turned off (bottom window). The number of measurement used in the fit is smaller than 2× the number of wafer intersecting the track, because track/cluster inefficiencies, grazing angle cut and the 5σ cut described in the text.

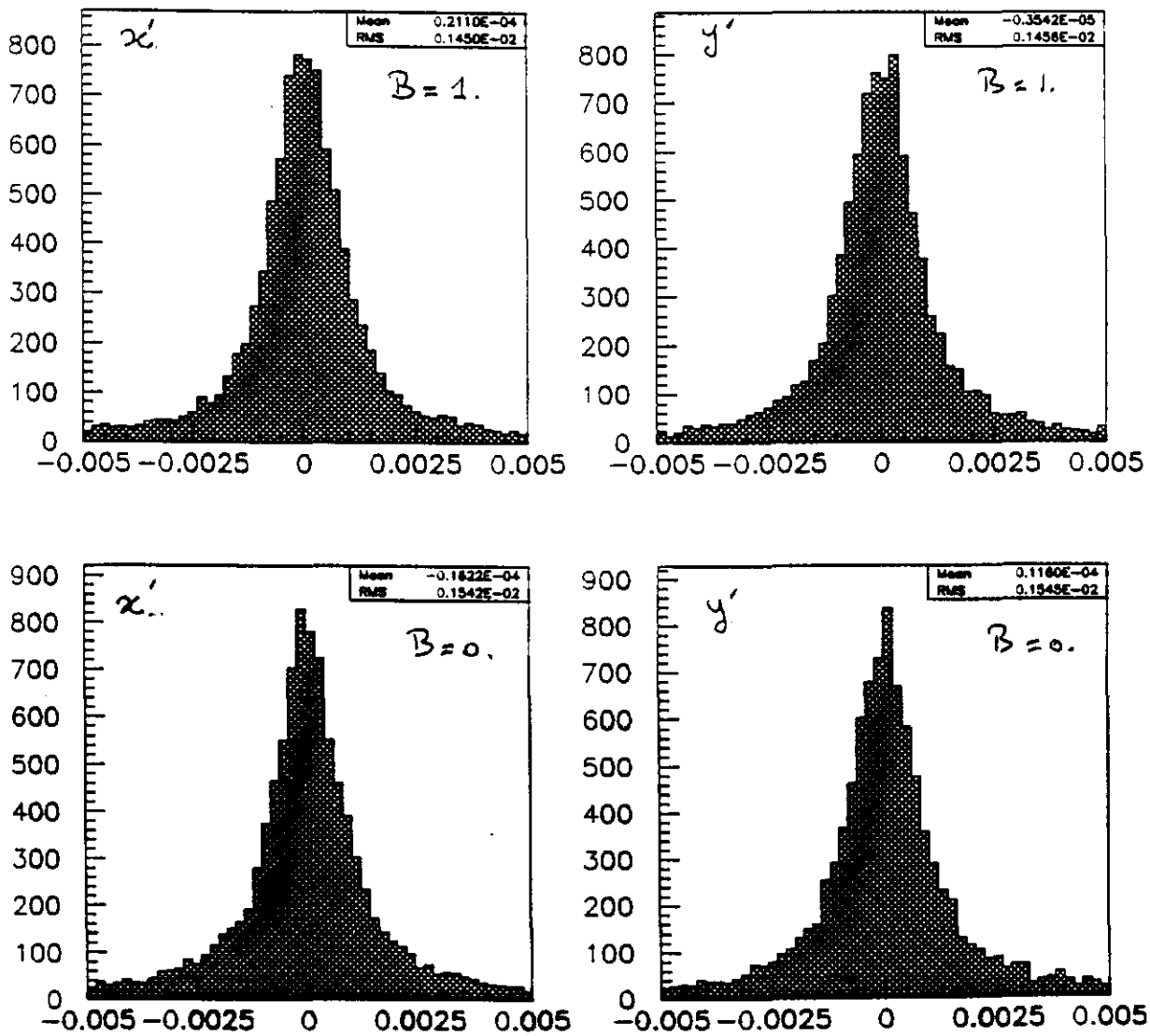

FIG. 26. Resolution curves for the two track parameters x' and y' for single track muon events. Units are radiants. These muon tracks were characterised by a fixed $P_t = 1.0$ Gev/c and the rapidity distribution was flat between $-3.$ and $+3.$, with an isotropic azimuthal angle. The two top curves have been obtained with the *pseudo-fit* (B = 1.0 Tesla), the two bottom ones with the straightforward linear fit (B = 0 Tesla).

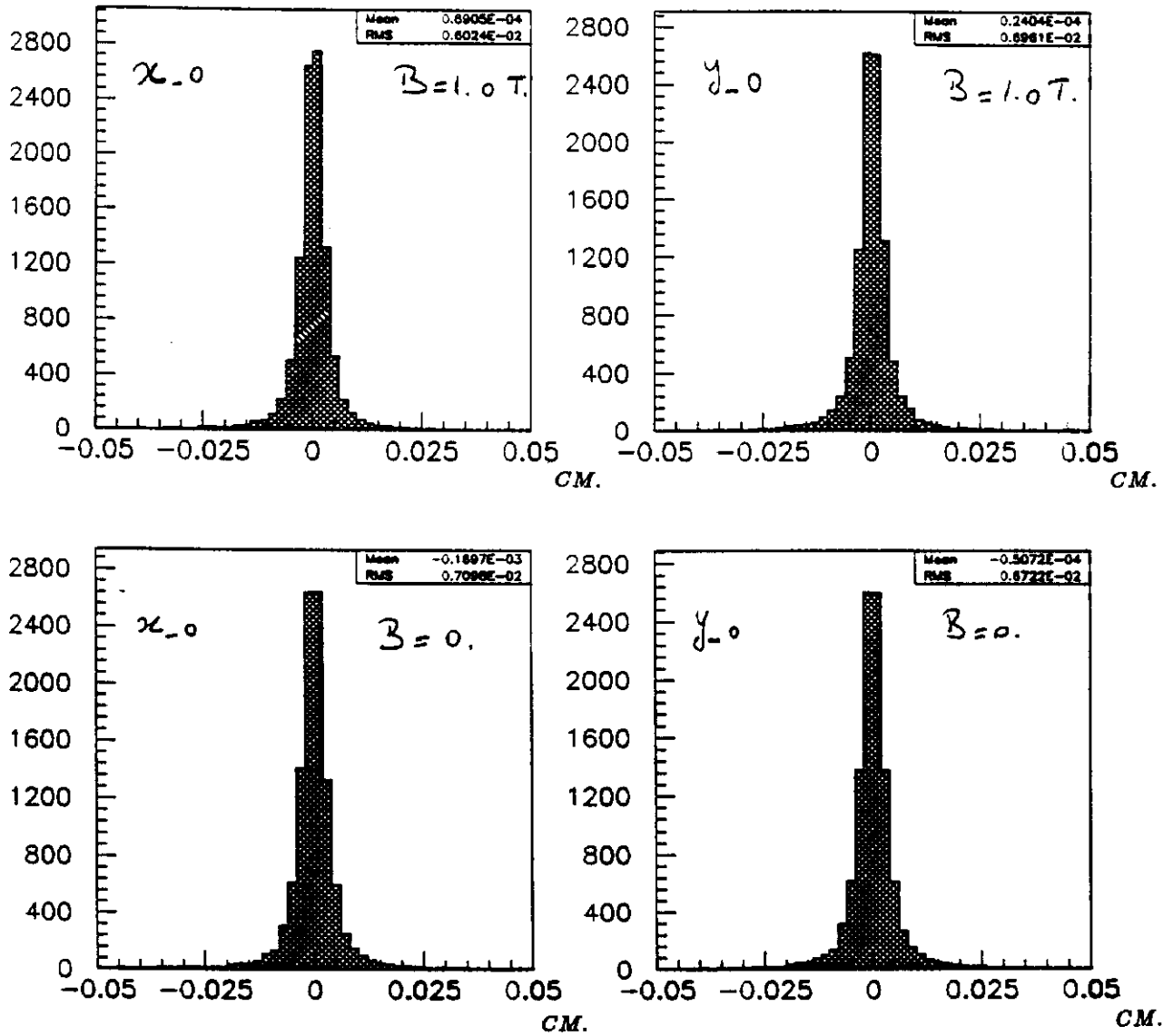

FIG. 27. Resolution curves for the two track parameters x_0 and y_0 for single track muon events. Units are cm. The track sample is identical to the one used in producing Fig 26. The two to curves have been obtained with the *pseudo-fit* (B = 1.0 Tesla), the two bottom ones with the straighforward linear fit (B = 0 Tesla).

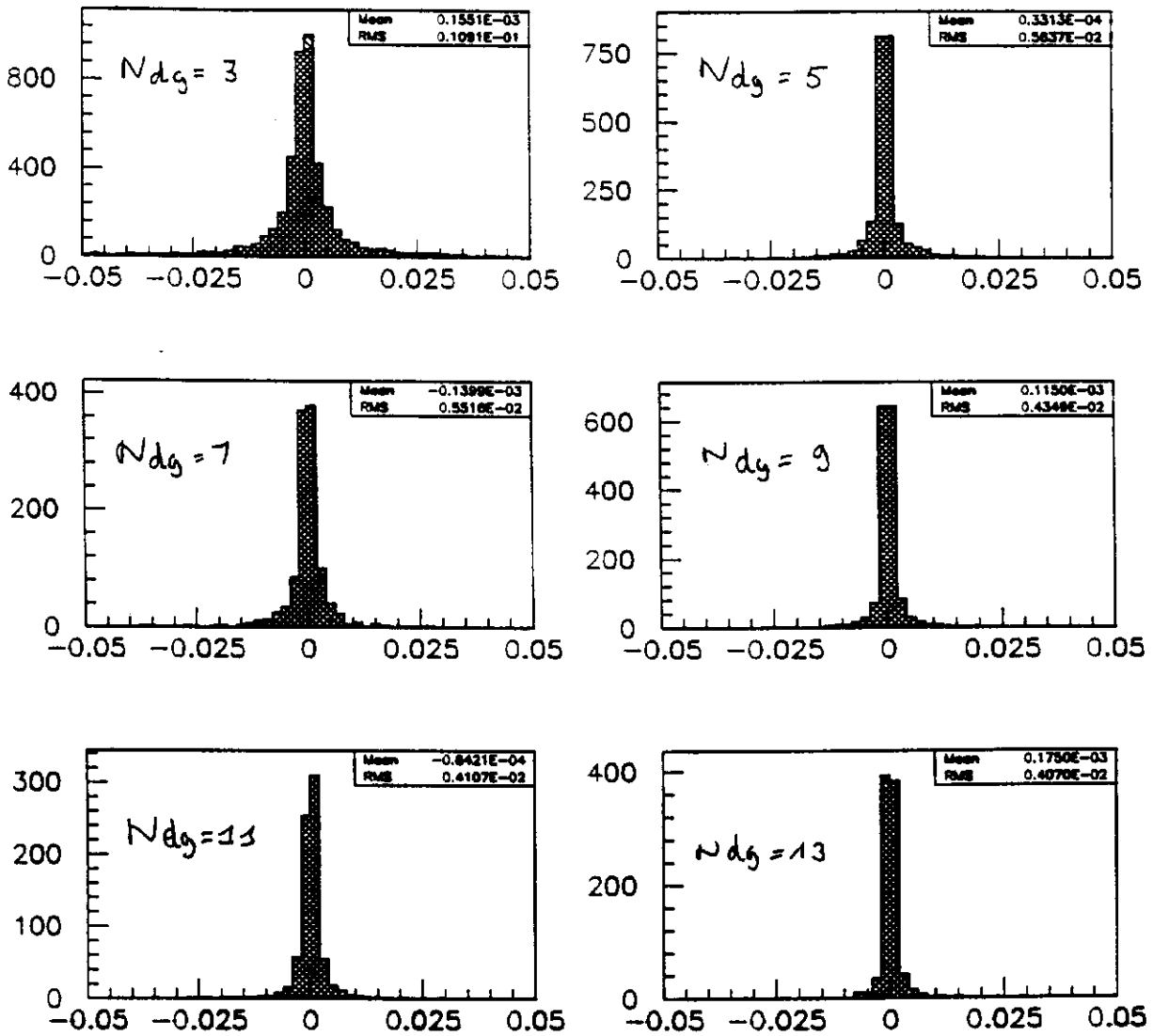

FIG. 28. z' resolution curves as a function of the number of degrees of freedom in the fit. The magnetic field was set at 1.0 Tesla. The sample is identical to the one used in the previous figure.

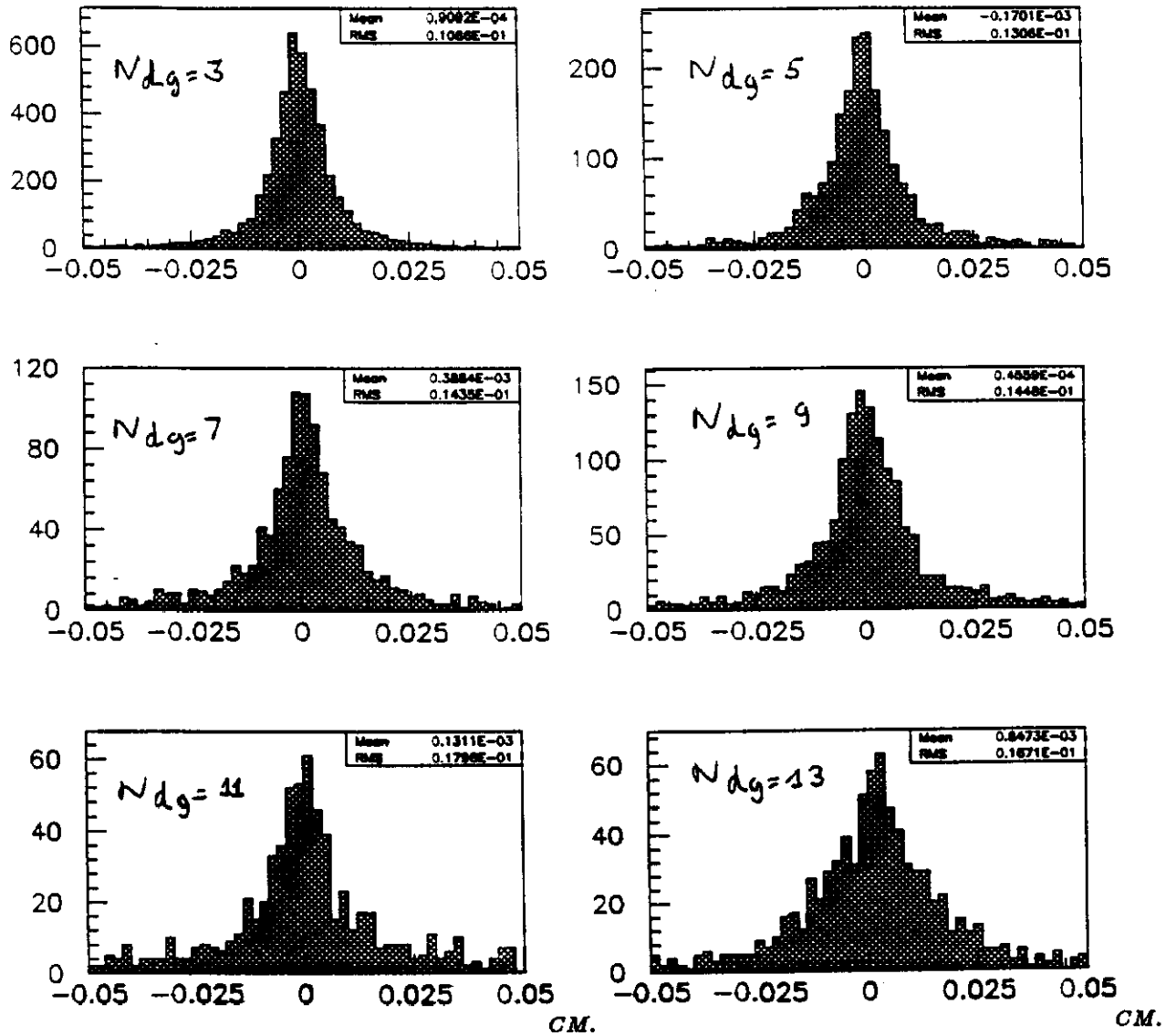

FIG. 29. z_0 resolution curves as a function of the number of degrees of freedom in the fit. The magnetic field was set at 1.0 Tesla. The track selection and event topology is described in detail in section III. B. The σ_{STRAW} parameter was set 100 μm.

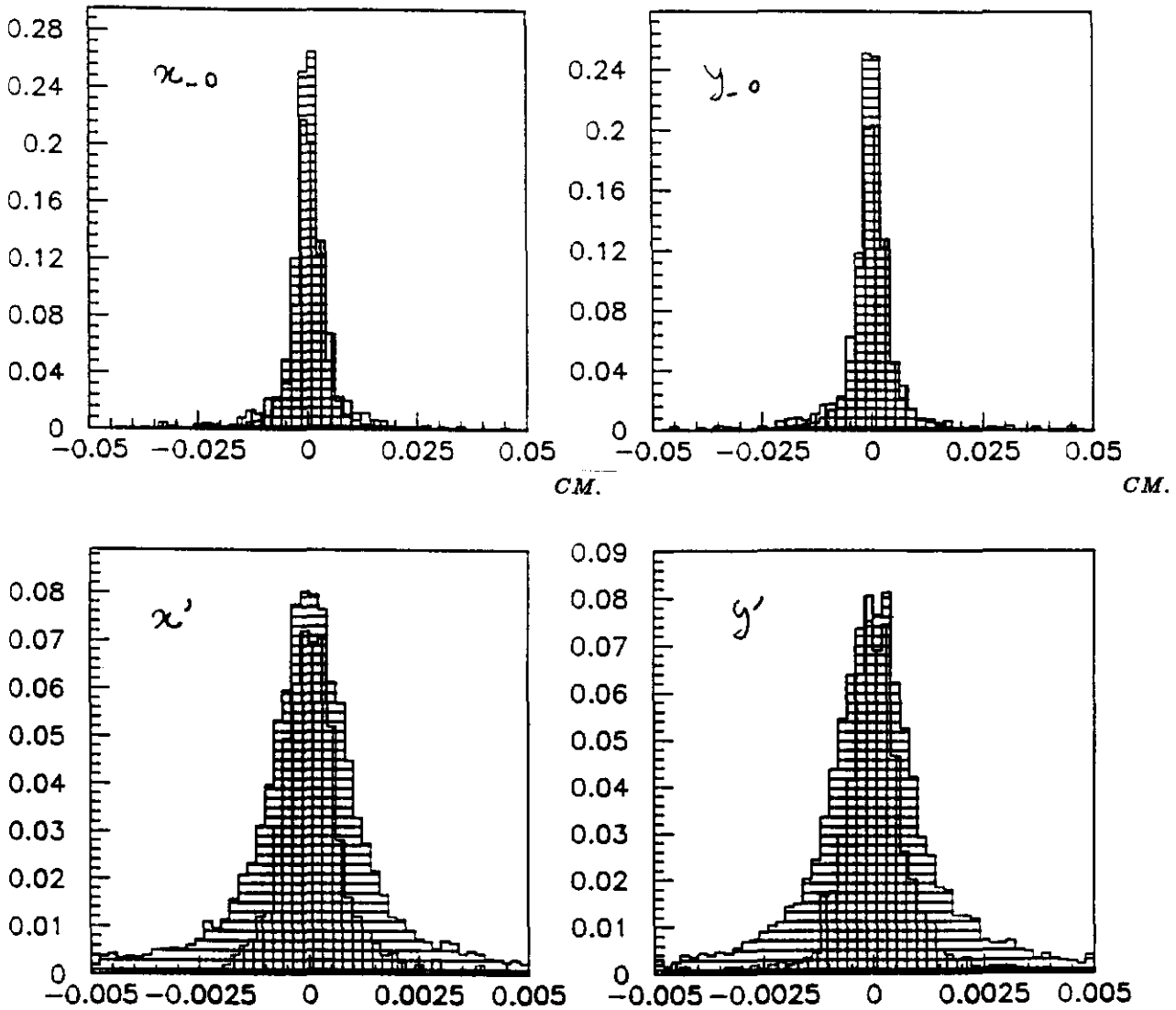

FIG. 30. Effective resolution curve for the four track parameters x_0, x', y_0 and y' below 3.0 Gev (horizontal hash) and above 3.Gev (vertical hash) These are single muon track events, as described on fig 26. The histogram have been renormalised, in order to enhance shape differences. The worsening of the resolution at low momentum is due to multiple scattering and affects mostly the x' and y' parameters.

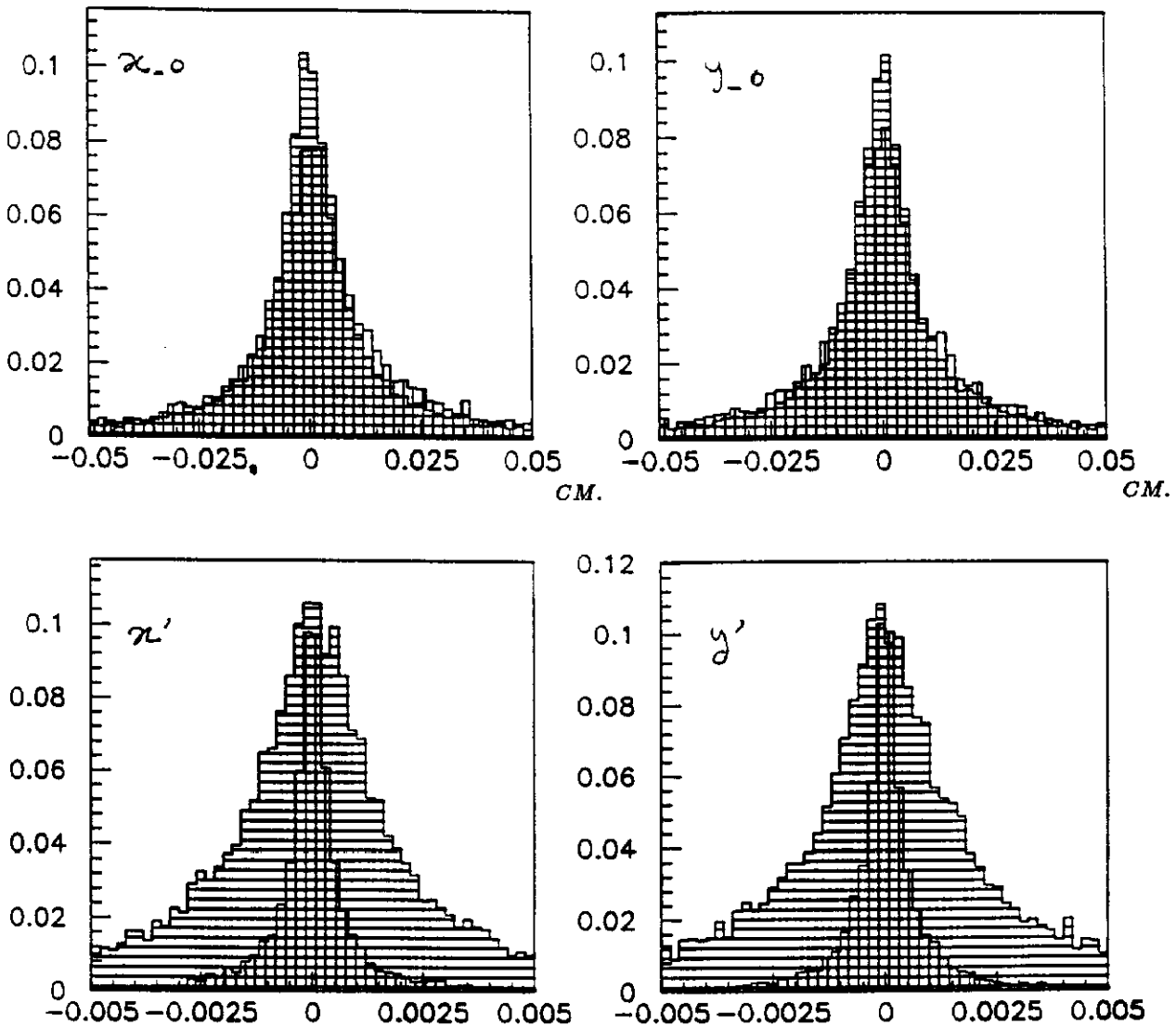

FIG. 31. Effective resolution curve for the four track parameters z_0, z', y_0 and y' below 3.0 Gev (horisontal hash) and above 3.Gev (vertical hash) The track selection and event topology, $B - jets$, are described in detail in section III. C. The worsening of the resolution at low momentum is mostly due to multiple scattering. $\sigma_{STRAW} = 100\ \mu m$.

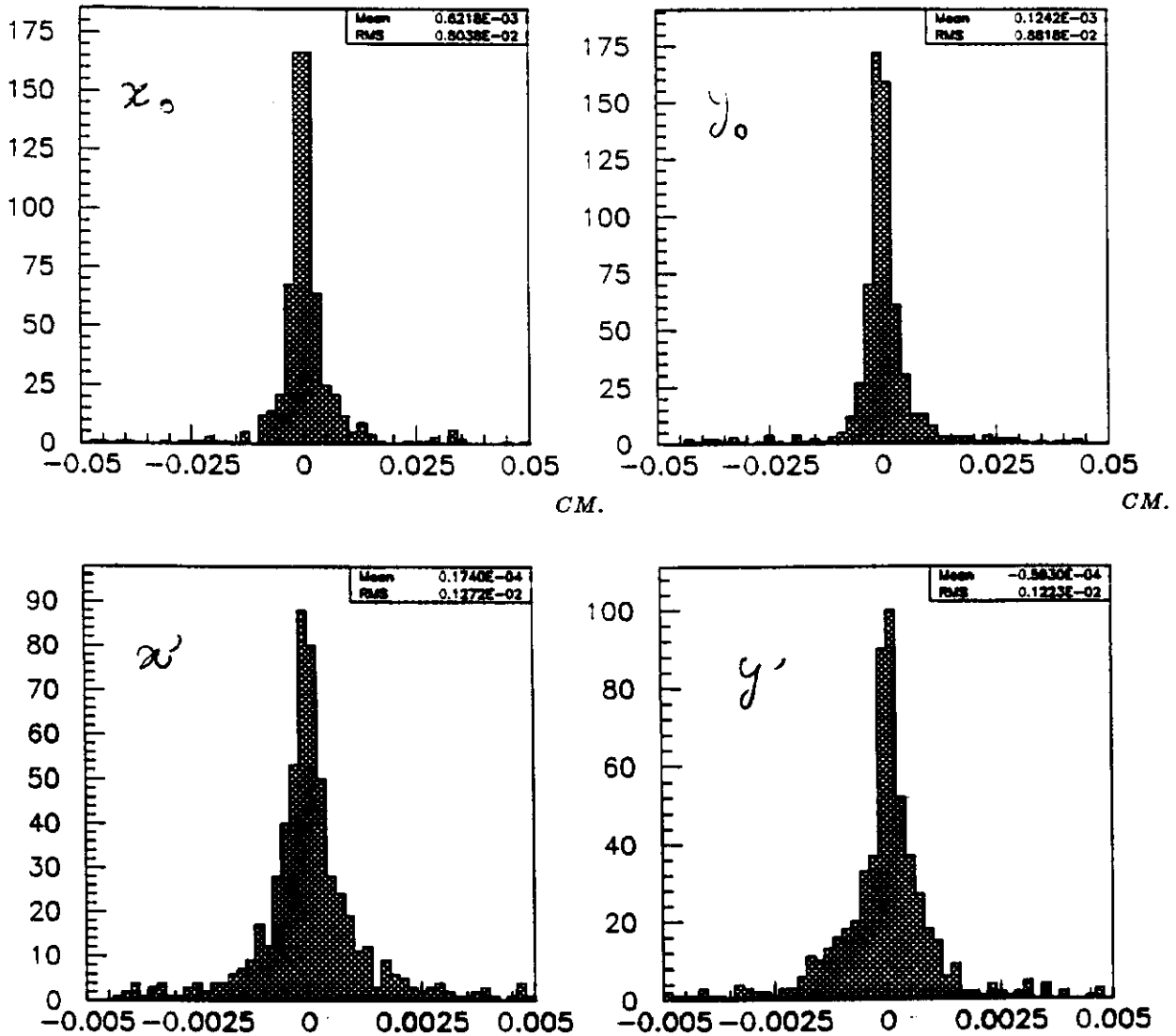

FIG. 32. Effective resolution curve for the four track parameters x_0, x', y_0 and y' . These track are π tracks from $B_d \to \pi^+\pi^-$ decay exclusively. $\sigma_{STRAW} = 100.\mu$m.

D. The Vertex level

The detailed analysis of the vertex resolution for the $B_d \rightarrow \pi^+\pi^-$ decays is still preliminary. Particularly difficult to estimate is the final *merit factor* - the ratio of the acceptance for the signal to the background reduction factor - This quantity obviously depends on some kinematical cuts, such momentum or mass, resolution factors and B life time . Only vertexing issues, resolution factors in particular, are discussed here.

1. Estimation of the effective vertex resolution.

This resolution is determined by two idependent factors :

- The track resolution at the vertex. The x_0 and y_0 resolutions are obviously crucial (fig. 32). The B_d vertex resolution is better than the one obtained for an arbitrary set of generic tracks in the same event, partly because a transverse momentum cut ($P_t \geq 0.5$ GeV/c) was applied.
- The vertex topology in the event. The cleanest case - but least interesting ! - is characterized by a single "primary" vertex, which includes all SVX tracks. The most difficult one is characterized by (i) multiple events within a few cm of each others within the same rf bucket (ii) multiple heavy quark decay of the type $b \rightarrow c \rightarrow s$, where about 2×6 charged tracks are coming from 2×2 detached vertices.

If no hypothesis are made on the vertex topology, a large number of combinations (track to vertex assignments) must be considered for every event. This is not only time consuming, but also wasteful since many of these combinations are likely to be unphysical. For instance, a B mesons has an electric charge $|Q| \leq 1$, while a statistical fluctuation can induce a secondary vertex characterized by, for sake of argument, 3 positive tracks. In addition, the knowledge of all vertex locations is not really required, "spectator" K^0 decays being not necessarily of interest. In order to simplify the vertex fitting procedure, and also improve the final vertex resolution, hypothesis on the vertex topology should be made. In this study, the decay $B_d \rightarrow \pi^+\pi^-$ was chosen because of it's crucial physics relevance, and it's conceptual simplicity. Because of the relatively small branching ratio (expected to be of the order of 10^-5) and the huge combinatoric background, it will be a difficult decay mode to observe, definitely hopeless without a vertex detector. Only one event out of 10^8 minimum bias trigger is contain a real $B_d \rightarrow \pi^+\pi^-$ decay...

B_d mesons were forced to decay in this mode at the event generation phase. After proceeding to the SVX track selection and fitting as described above, track pairs with an invariant mass within 50 MeV of the B_d mass were selected. A transverse momentum cut ($P_t \geq 0.5$ GeV/c) was applied on both π tracks to further remove backgrounds. Within this 100 MeV mass window, the probability to find such a pair of tracks unrelated to the B_d is less then a few percent, while keeping a large fraction of the π tracks from the B_d. Thus, provided the event has such a decay, the combinatorial background is not a problem. These two tracks were forced into a single vertex, a linear vertex fit algorithm from CERN [10] was used to compute the reconstructed vertex position and its covariance matrix. The χ^2 associated to this fit is a direct measurement of the validity of the hypothesis that these 2 tracks do indeed form a vertex. The effective resolution curves for this vertex are shown on Fig 33.

Once this selected secondary vertex is characterized, all other SVX tracks are considered to form a primary vertex. A priori, the number of tracks really belonging to this primary vertex is large compared to the number of tracks originating from other heavy flavored hadron and K^0 decays. Therefore, all these tracks are lumped into the primary vertex, and a first iteration primary vertex position can be computed. In a "clean-up" phase, the track with the worse $D.C.A.$ (distance closest to approach to the vertex, normalised by its error) was removed, a new primary vertex was formed. This procedure was repeated until no tracks with a $D.C.A. \geq 3.$ were left in the vertex. The primary vertex track multiplicity is shown on Fig 39 and its resolution on Fig 36. In order to assess the effect of "spectator" decays on the primary vertex resolution, the cut on the maximum $D.C.A.$ was relaxed. The x position resolution is shown on Fig. 40 as a function of this cut. Clearly, a slight degradation of the primary vertex due to these spectator decays has to be recognized. For sake of completeness, the primary vertex resolution for *minimum bias* event is shown on Fig 38. In some case, because of the lack of high P_t tracks, the resolution for *minimum bias* events is much worse than for the $B - jets$ events.

2. Acceptance studies

In order to compute real acceptance, independentely of the background contribution, only the *real* B_d vertex are considered in this section. Again, the $KINE$ and $VERT$ structure were used to check the π track origin.

Because of the incomplete acceptance coverage along the z axis, the hit matching criteria and the crude *pseudo-fit* used to reconstruct SVX tracks, the track reconstruction efficiency is currently rather poor. The first effect can be seen on fig 37, while the other effects can be qualitatively established by looking at the number of wafers seen by these tracks and the number of matched hits (fig 34). The probability to reconstruct such a track is currently about 30 %. This acceptance must be improved ! As a consequence, about 15 % of the relevant B_d decays can be submitted to the vertex algorithm.

Most important is the ratio of the reconstructed distance between the primary and the selected secondary vertex over its error, $\Delta L/\sigma_{\Delta L}$. This quantity is displayed on Fig. 41. Note that these errors do not follow Gaussian statistics. If one asks for a significance of at least 5 " σ ", ($\Delta L/\sigma_{\Delta L} \geq 5.$), 5.7 % of the B_d mesons are kept (Table VII). This means that the relative acceptance for this vertex cut, for the real signal, is about 42 %. This vertex acceptance is slightly biased towards high momentum (see Fig 35). This is mostly due to multiple scattering. Yet, a substantial fraction of the accepted B's have a momentum below $\approx$ 10. GeV. This acceptance justifies the instrumentation of the central region.

3. *Background rejection*

The same analysis can be repeated on other classes of events (fig. 42), in order to estimate the background rejection capability of the SVX detector. $B - jets$ and *minimum bias* events were generated and analysed as described above. The probability to find a 2 π track combination with a mass within 25 MeV of the B mass is rather small, of the order of 1%, even smaller if the P_t cut is raised. Thus, a lot more cpu time has to be dedicated to study the background than the signal. In order to compute a *first guess* of the merit factor in timely fashion, the mass window was made very wide to accept more background, ($3.75 \leq M \leq 6.75$ GeV). Note that, since this invariant mass is related to the relative opening angle of the π tracks and while this opening angle dictates the secondary vertex resolution, this cheat will affect the answer to some extent. A much larger sample will be required to perform this calculation correctly and will be done in the near future. The relative acceptance of this vertex cut for this particular class of track combinations is described on table VII. Applying a χ^2 cut (a confidence level cut on the validity of this vertex), only 2.3% of these *spurious* vertices are kept.

The final *merit factor* for this particular detector design, minimum bias event sample and specific vertex reconstruction algorithm is $\approx 42\% \times 1/(2.3\%) \approx 20$. This signal to noise improvement can be obtained with rather simple algorithms. Since this factor is definitely smaller for $B - jets$ events, more complete vertex algorithms involving the complete event topology (i.e., both B's..) will have to be considered in the future.

Because the Monte-Carlo information has been kept throughout this analysis, the source of background can be investigated, to a large extent. In the $B - jets$ sample, about 10 to 15 % (depending on the detachment significance cut) are indeed coming either from B or D decays. The other obvious source is due to pattern recognition failure : the probability to find at least one *confused* cluster for a given SVX track ranges from 11 % to 25 %, again, rising with the detachment significance (the *false* or *apparent* significance !).

TABLE VII. Acceptance for signal (*real B decays*) and background (em spurious vertices) for the $B_d \to \pi^+\pi^-$ decay mode. σ_A is the statistical error on this acceptance A. Systematic uncertainties are not presented here. The right-side columns refer to the same event sample, where the $\pi^+\pi^-$ vertices have a χ^2 small enough to validate this vertex hypothesis.

Acceptance (absolute) for $B_d \to \pi^+\pi^-$ *real* decays				
$\Delta L/\sigma_{\Delta L}$	A (%)	σ_A	A ($\chi^2 < 5.$)	σ_A
0	13.4	1.0	11.3	0.9
1	12.0	1.0	10.0	0.9
3	8.75	0.75	7.1	0.7
5	7.2	0.7	5.7	0.6
10	4.8	0.6	3.7	0.6
Acceptance (relative) for $B_d \to \pi^+\pi^-$ background ($3.75 < M < 6.75$), $B - jets$ event topology				
$\Delta L/\sigma_{\Delta L}$	A (%)	σ_A	A ($\chi^2 < 5.$)	σ_A
0	100.0	-	60.0	2.5
1	79	2.6	42.8	1.7
3	46.7	1.8	17.6	1.0
5	30.0	1.4	8.3	0.6
10	16.0	0.9	2.9	0.4
Acceptance (relative) for $B_d \to \pi^+\pi^-$ background ($3.75 < M < 6.75$), *Minimum bias* event topology				
$\Delta L/\sigma_{\Delta L}$	A (%)	σ_A	A ($\chi^2 < 5.$)	σ_A
0	100.0	-	56.0	5.0
1	79	6.4	40	4.1
3	41.0	4.1	12.8	2.1
5	27.0	3.2	5.8	1.3
10	13.0	2.1	2.3	0.8

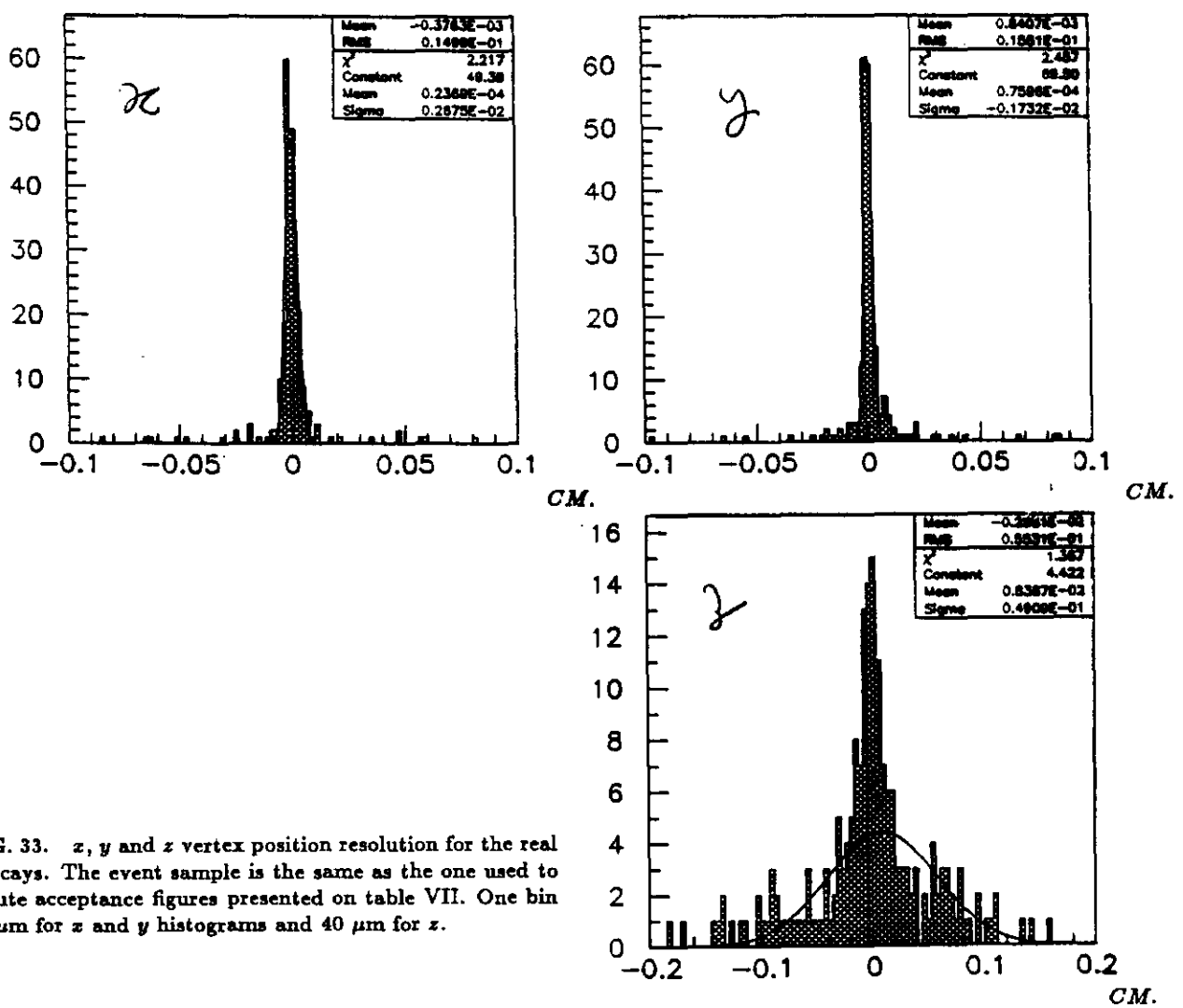

FIG. 33. x, y and z vertex position resolution for the real B_d decays. The event sample is the same as the one used to compute acceptance figures presented on table VII. One bin is 20 μm for x and y histograms and 40 μm for z.

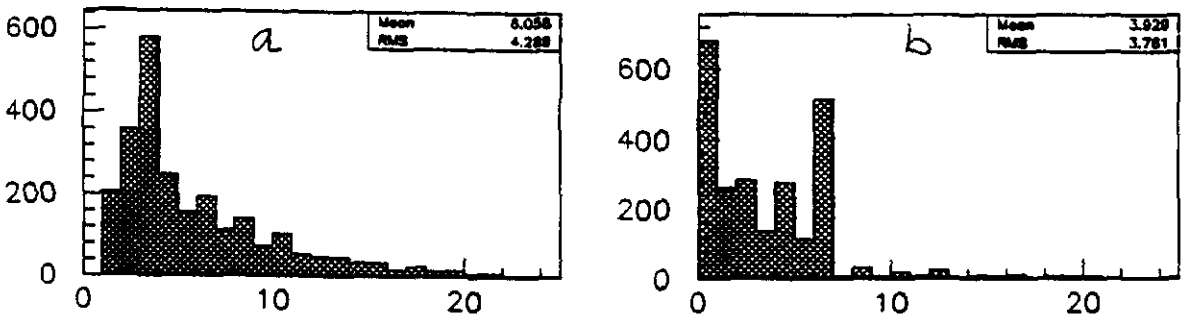

FIG. 34. The number of wafers crossed by the π tracks from B_d decays (left), and the corresponding number of hits available in the fit (right) . Four hits are required for a zero degree fit. This last distribution has a peculiar sh indicates a serious acceptance loss. This is due to the combined effect of : (i) decays occurring at $|Z| < 24.$ cm. are be missed by the central *BARREL* wafers. (ii) these π tracks are biased towards high P_t, because the large Q value decay (iii) measurements at grazing incidence are ignored. Further studies will have to be done to correct for this...

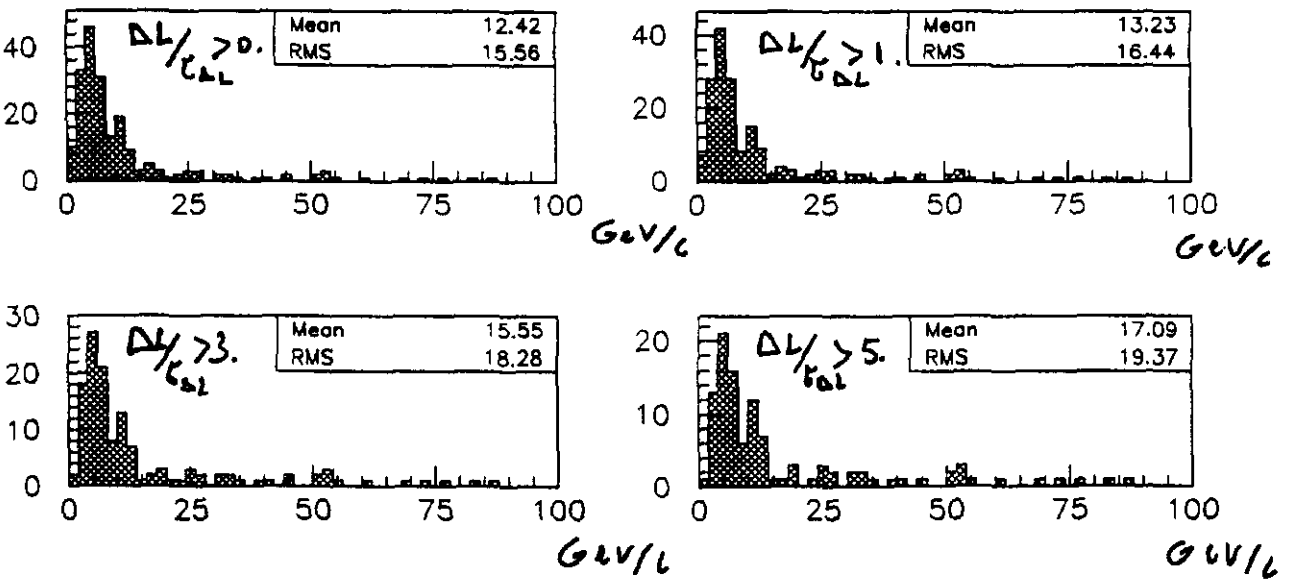

FIG. 35. The momentum distribution for 4 different detachment significance cuts. The event sample is the same as used to compute acceptance for real B_d decays discussed in table VII.

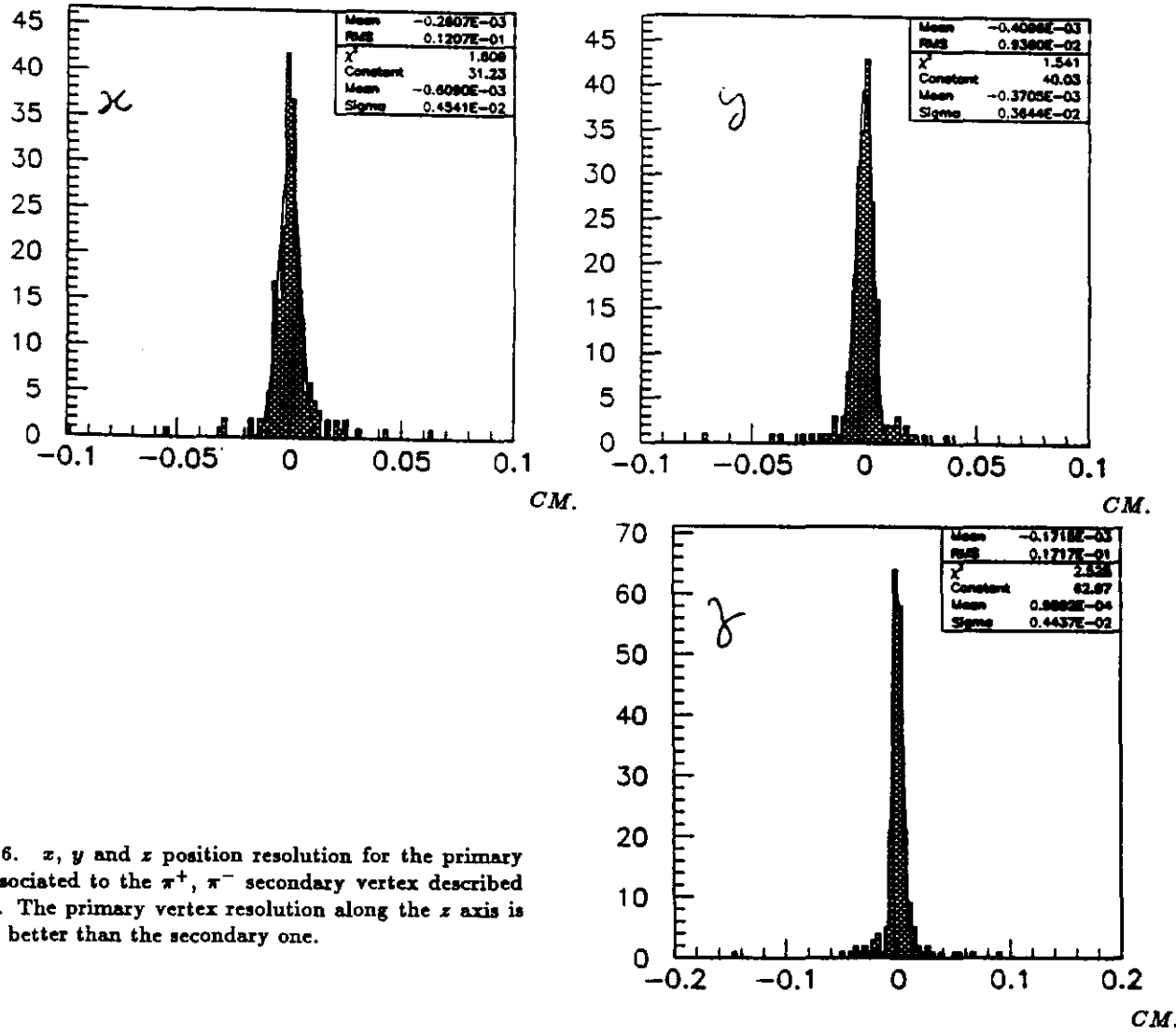

FIG. 36. x, y and z position resolution for the primary vertex associated to the π^+, π^- secondary vertex described on fig 33. The primary vertex resolution along the z axis is definitely better than the secondary one.

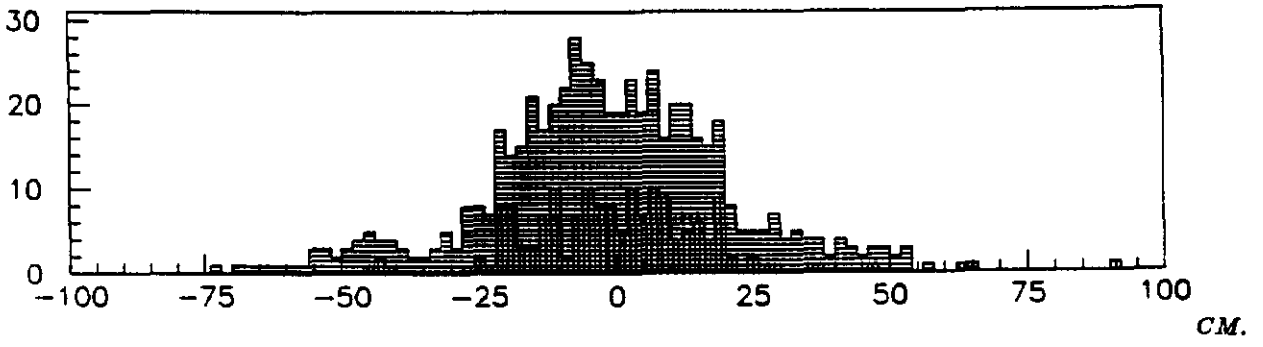

FIG. 37. The Z position of events with a well reconstructed primary vertex (horizontal dash) and of a subclass of these events where a $B_d \to \pi^+\pi^-$ has been fully reconstructed (vertical dash). In both cases, events generated outside the $BARREL$ region (total length is 48 cm.) are currently not reconstructed efficiently. The $r.m.s.$ of the generated distribution has been set to 30. cm in the Monte-Carlo, and follows a simple Gaussian.

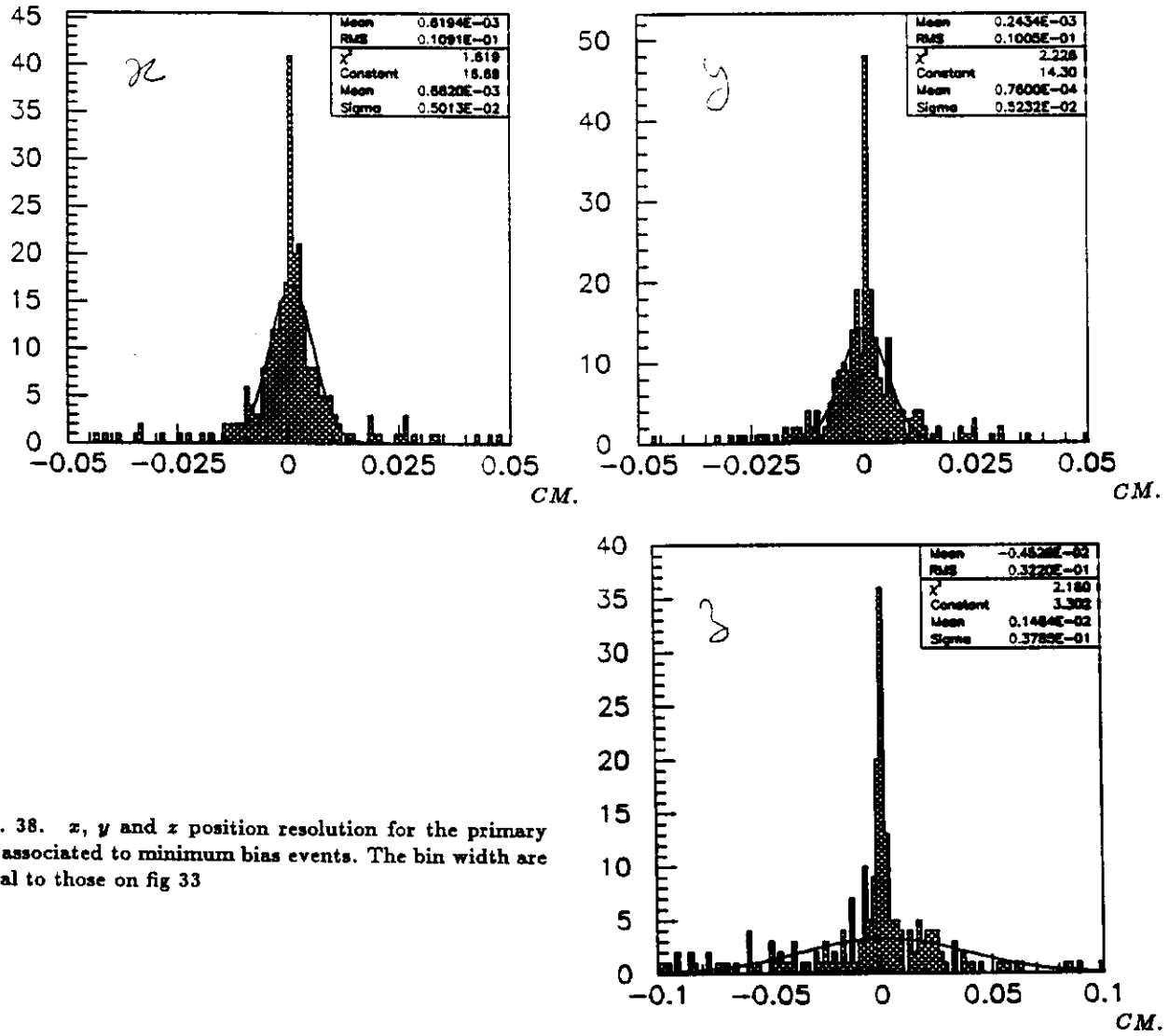

FIG. 38. x, y and z position resolution for the primary vertex associated to minimum bias events. The bin width are identical to those on fig 33

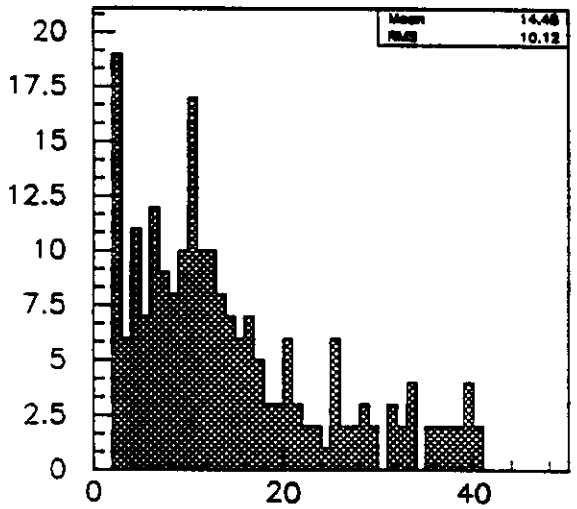

FIG. 39. The primary vertex track multiplicity distribution. The event topology and reconstruction cuts are those corresponding to fig 33.

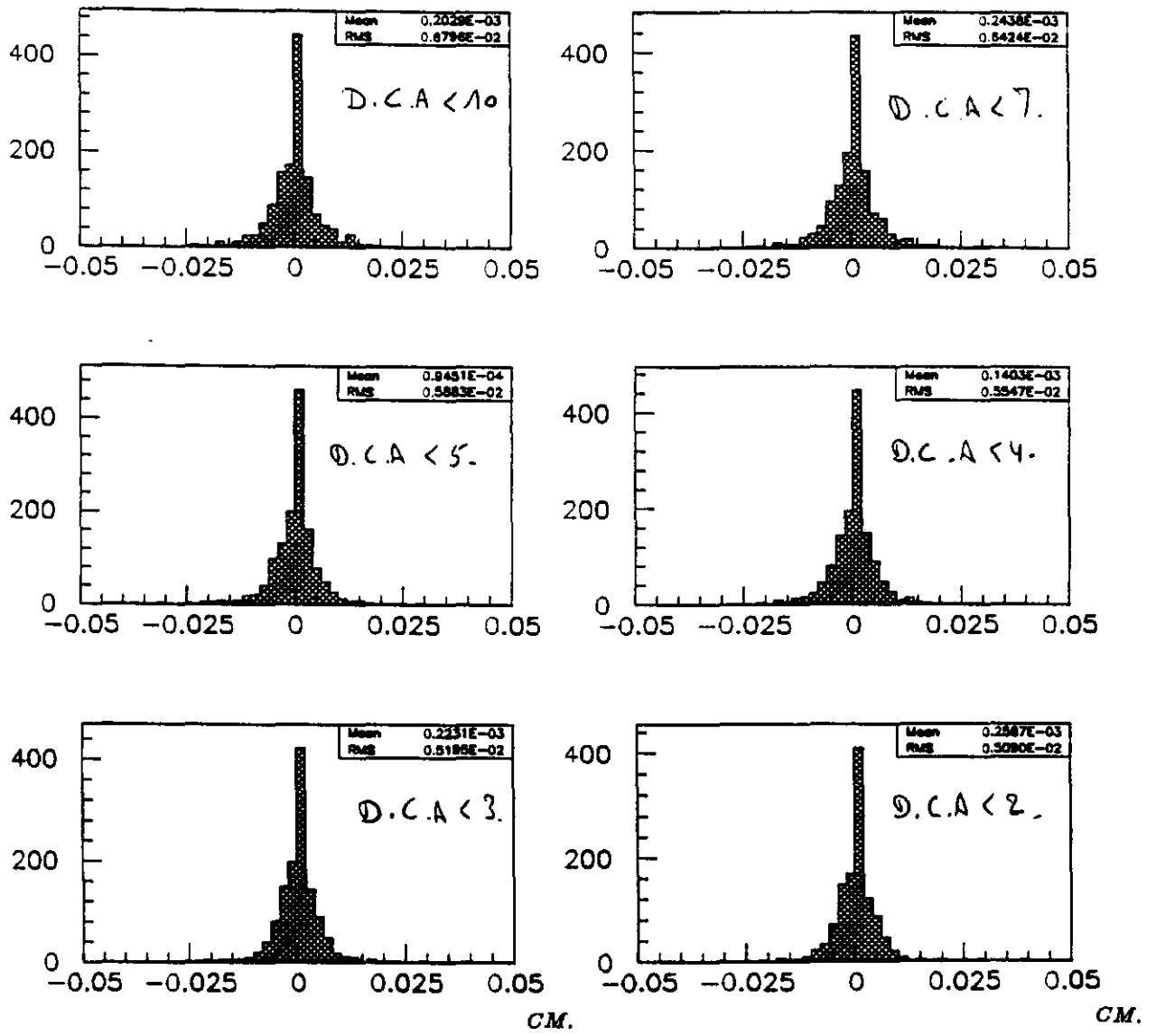

FIG. 40. The z vertex resolution curves for the primary vertex shown as a function of the maximum $D.C.A.$ allowed in this vertex. As this parameter increases, the number of suspicious tracks thrown out of the vertex increases, causing a modest resolution improvement. The event sample is the same as the one used on fig 33.

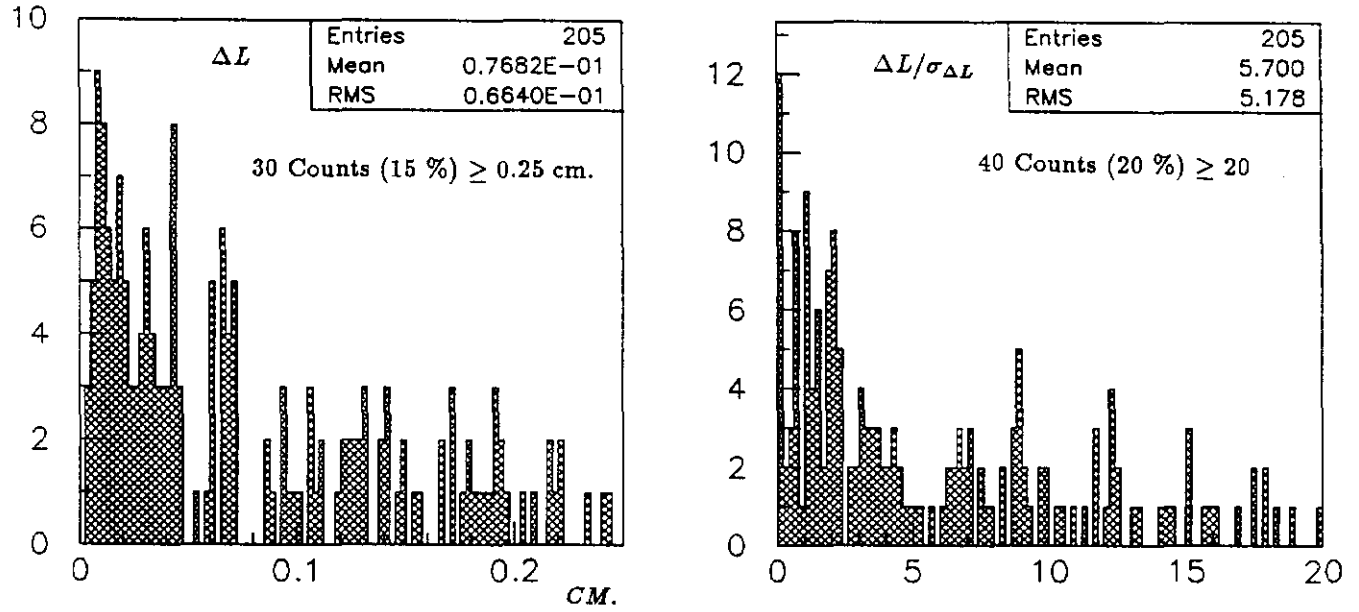

FIG. 41. ΔL and $L/\sigma_{\Delta L}$, the cartesian distance between the real B_d decay vertex and the primary vertex and the same quantity normalised to its error. The event topology and reconstructions cuts are those corresponding to fig ??.

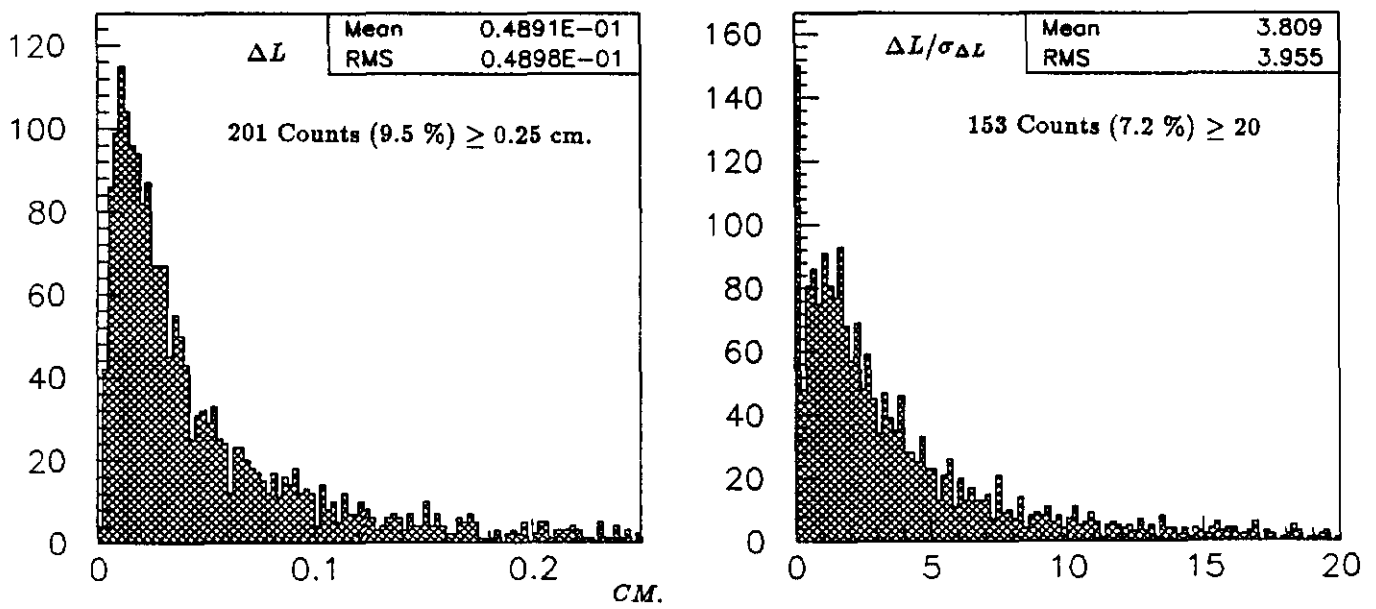

FIG. 42. ΔL and $L/\sigma_{\Delta L}$, the cartesian distance between the spurious $\pi^+\pi^-$ secondary vertex and the associated primary vertex (top) and the same quantity normalised to its error (below). The event topology is $B - jets$, where no $B_d \to \pi^+\pi^-$ occurs. These *pseudo detached* vertices were made of any 2 π tracks with $P_t > 0.5$ GeV, with an invariant mass within 1.5 GeV of the B mass.

E. Stand-alone SVX Algorithms : Preliminary Studies

Although the SVX detector has been designed to be used in conjunction with a central tracks system, there is a large amount of redundant information due to number of wafers intersecting the particle trajectories (Fig. 19). Therefore, it makes sense to investigate stand-alone SVX algorithms in the context of fast triggering or, eventually, configuration where the central tracking system is insufficient. Prior tackling specific topics, it is worthwhile to visualize a typical event ignoring the volume boundaries or the GEANT tracks themselves. The event display presented on fig 43 and is the raw to handled by such SVX stand-alone algorithm.

Topics relevant to both *online* and *offline* environment have been studied quantitatively. In particular, the following questions have been asked :

- How well can we reconstruct the primary vertex without SVX tracks by simply performing some kind of cluster position average ? Although this particular algorithm has not been implemented yet, a simple look at fig 43 teaches us that no obvious vertex location can be deduced just by computing a global average D_hit location. Seen from the correct angle, tracks pointing to the center of the pictures are visible, suggesting that tracking is a necessary condition to vertexing.

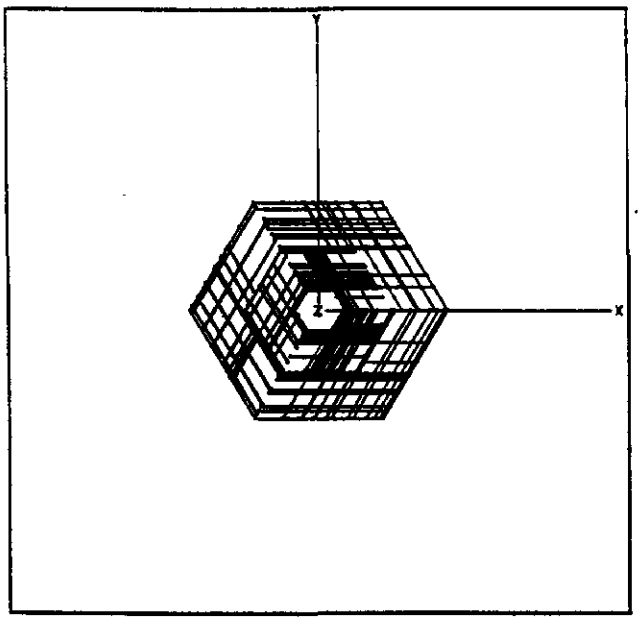

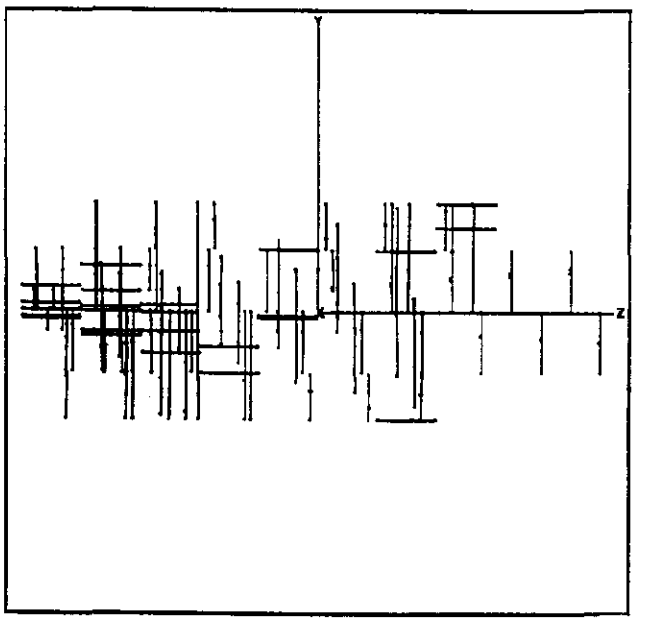

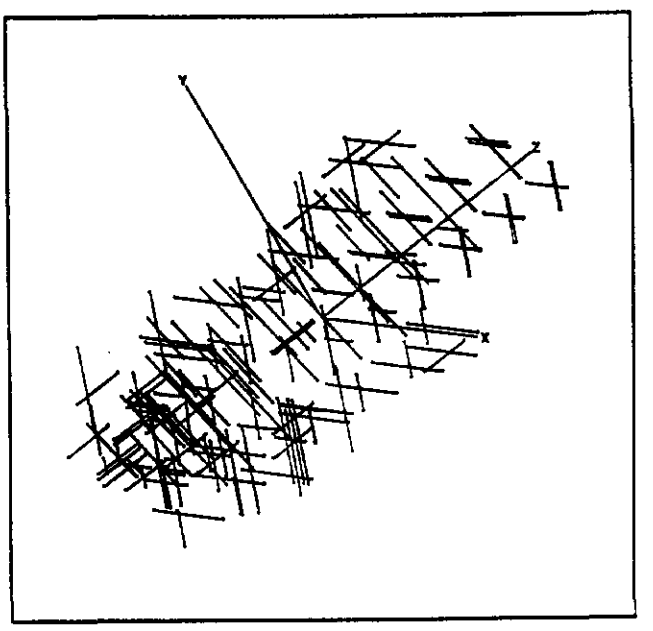

FIG. 43. A D_hit representation of a typical minimum bias event. Each line represents a strip whose signal is significantly above pedestal. To ease pattern recognition *by eye*, the magnetic field was set to 0. [9]

- Once crude projections (2-dim. track parameter, expressed in the x or y plane and at the vertex), or SVX tracks are made available (expressed at the presumed vertex location, so linear extrapolation are valid even in the presence of the magnetic field), how well can we locate the primary vertex along the z axis by averaging the Z position of all projections (or tracks) at $x = 0.$, $y = 0.$? Various simple algorithms have been considered, all of them bypassing the complicate vertexing procedure described in the previous section :

  - A simple unweighted average deduced from x or y projections only gives a $r.m.s.$ for this z primary vertex distribution of about .4 cm
  - If these averages are performed by assigning a weight proportional to the squared inverse of the z position error at $x = 0.$ or $y = 0.$, this r.m.s. becomes .5 mm
  - If the 2 unweighted x, y projection based averages are combined, this $r.m.s.$ is reduced to .35 cm.
  - If the 2 weighted x, y projection based averages are combined, this $r.m.s.$ is reduced to .45 mm.
  - This last figure can be further improved to $r.m.s.$ of 400 μm if this vertex is "cleaned up" from significantly detached tracks (characterized by an inconsistent Z at $x = 0., y = 0.$).

  As expected, these weights play an important role. They are based on errors, which themselves are based on the knowledge of the track momentum.

- Can meaningful vertex informations can be gathered without momentum information ? Highly doubtful: certainly the track curvature can not be ignored and only 1/3 of the tracks might have stand-alone nonbend view (y) projections, because of the hexagonal geometry and the strip orientation. In addition, the error at the vertex can not be estimated reliably since the multiple scattering uncertainties are unknown, leading to the disappointing results expressed in the last topic.

- What is the momentum resolution using a stand-alone SVX track fitting procedure ? Since the x' resolution varies widely depending on the topology, there is no simple answer. In any event, even using the exact absolute value of the momentum, while deducing the momentum directions from the pseudo-fit parameters x' and y' described in the SVX track fitting procedure, one gets a π^+, π^- invariant mass resolution at 5. GeV which is not good enough to detect a missing π^0 among the B_d final states. Yet, further studies are worth considering if the central tracking system is either too costly or cumbersome.

IV. CONCLUSIONS.

A complete and detailed Monte-Carlo simulation and analysis package for the proposed BCD SVX detector has been written. Spatial resolution at the Silicon wafer has been studied extensively and very soon will be compared with data [20]. Emphasis will be placed on the angular dependance of the position resolution at the wafer in these tests. Track fitting techniques and vertex topologies have been investigated. A preliminary study of the $B_d \rightarrow \pi^+\pi^-$ decay showed that a final acceptance of 5 to 10% can be reached, while rejecting hundreds of spurious combinations by requesting detached vertices. Yet, the final goal of 5 μm spatial resolution, 20 to 40 μm at the vertex allowing for SVX merit factor of 100 to 1,000 or more have not been demonstrated. Thus, the following upgrades will have to be considered :

1. *As mentioned above, many of the results are production model dependant.* The track multiplicity for both $B-jets$ and minimum biased are suspiciously high. The rapidity distribution of production model for minimum bias, charm and beauty events needs more attention. This work should be repeated using existing data, for instance, directly reading CDF minimum biased data stream.

2. *The geometrical description of the detector within the Monte-Carlo* program deserves more efforts. Particularly important is the flexibility in defining new geometry (octagonal structures instead of hexagonal, for instance) or the implementation of complex volumes, such as the flared conical beam pipe. Clearly, modern CAD/CAM software has to be brought to the HEP community.

3. *The precision problem* described in the appendix must be resolved. Unfortunately, a substantial amount of work will be required to install the required DOUBLE PRECISION arrays in GEANT and ensure appropriate memory management of these arrays by ZEBRA.

4. *Spatial resolution at the wafer for single track* is essentially a hardware challenge, since one of the crucial factor is the noise level at the preamplification stages. Reducing this noise allows for more sophisticated cluster finding algorithms, such a edge searches or truncated/weighted average to find a more accurate cluster position. In addition, more channels might be required if test beam data shows that reading every strip provides better resolution. Improving the spatial resolution must be carefully weighted against increase of material in the detector : for a substantial fraction of the momentum phase space (P less 1.5 GeV/c, or so), the biggest contribution to the effective resolution is multiple scattering.

5. *Spatial resolution loss due to pattern recognition failures* has been established. A few percent of the tracks are contaminated with misassigned D_hits. This frequency is proportional to the square of the event multiplicity, if the tracks are distributed smoothly in phase space. Therefore, this effect is highly production model dependant and deserves more attention.

6. *Spatial resolution at the vertex* is obviously related to the effective resolution at the wafer. Yet, improvements can be made using more accurate fitting techniques, including better handling of the component of the covariance matrix due to multiple scattering. Such techniques do exist [16], and can be applied to our problem provide the fit is not done in such a cumbersome *mixed coordinate* system.

7. *Vertex algorithms* are highly final state dependant, and can be written in a fairly well organised way once the correct track representation is found. No new software tools are required, although some useful algorithms have not yet been implemented :

   - Spurious vertices can be detected by requiring that tracks belonging to secondary vertices do not point back to the primary vertex. Although this secondary vertex can be significantly detached from the primary, an individual track lumped accidentally together into this secondary vertex will be characterized by a small $D.C.A$ to the primary vertex [17].
   - The SVX track parameters can be improved once the position of the vertices are known. This clearly calls for global iteration algorithms, where tracking is reconsidered after accurate vertexing has been done.
   - Spurious vertices occur when tracks fitting is done poorly. This is partly due to STRAW track to SVX cluster misassignments. Therefore, every track associated to a significantly detached vertex must check for possible D_hit misassignments.

8. Two independent factors motivate us to move from the hexagonal geometry to either a *square* or may be *octagonal* geometry as described on Fig 44. Note that, for all $DISK$ and half of the $BARREL$ wafers, the strips can be oriented along the x or y axis. For practical reasons, the connectors for the $DISK$ wafers must be

located exclusively on the outer edges of the wafer. This can only be achieved achieved with U, V stereoangle of 60° for an hexagonal geometry, while for a square geometry, this U or V strereo-angle becomes 90°. From the software viewpoint, the advantages are :

- This allows for x,*(bend view)* and y, *(non bend view)* independent projection reconstruction, which is almost mandatory if fast tracking algorithm are to be used in a SVX stand-alone trigger.
- The track fitting is done independently in x (a circle) and y (a straight line) views.

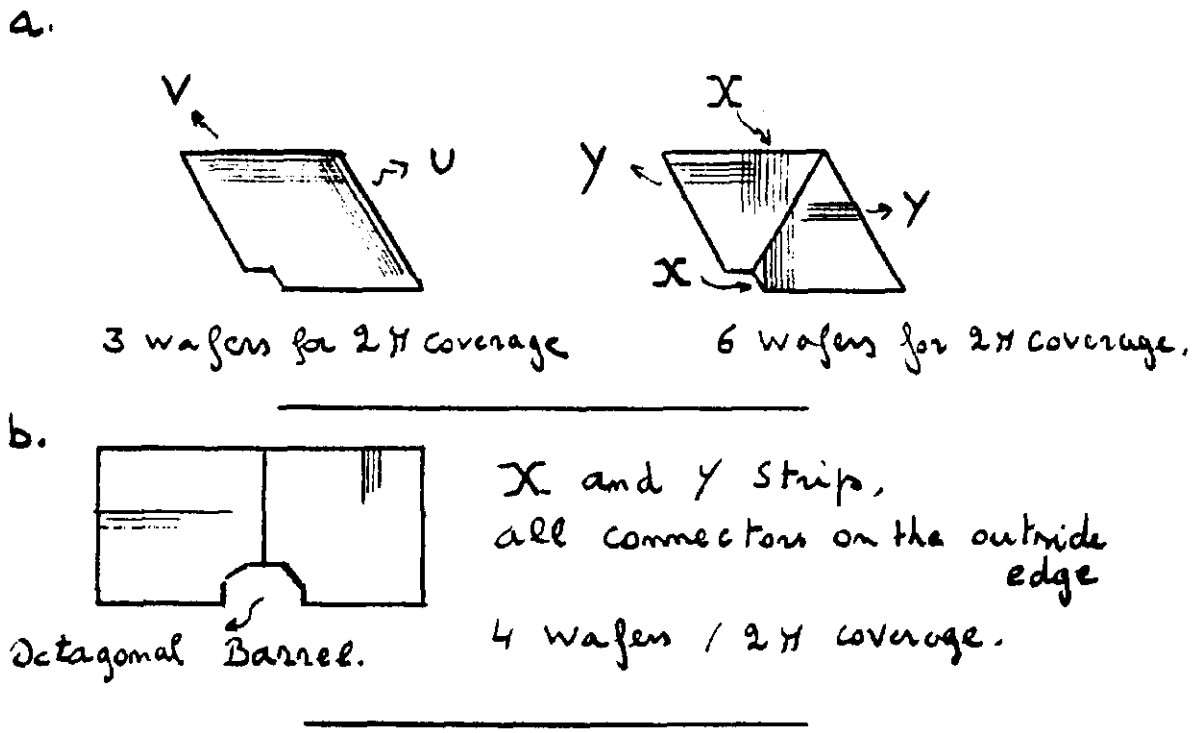

FIG. 44. The hexagonal and squared arrangements of wafers allowing for an easy implementation of x and y strips. Volumes orientations and size are similar to the one for fig 3

V. ACKNOWLEDGEMENTS

I wish to thank many of my BCD collaborators for their support. In particular, the advises of Lee Roberts, Linda Stutte, Jean Slaughter, Kirk McDonald and Nigel Lockyer were very helpful. I also wish to acknowledge the assistance of the Fermilab Computing Division staff. This research was supported in part by the U.S. Department of Energy.

APPENDIX : COMPUTATIONAL TECHNIQUES, SOFTWARE ENGINEERING

A. Hardware Platform and System

This software was originally written on a VAX VMS workstation. It recently has been ported to the SGI 25S "Data server" station, running the IRIX o/s (a System V UNIX o/s). This system was originally configured with 8 MgB. physical memory and had to be expanded to 16 Mgb. This RISC machine benchmarked at 12.5 Mips for the kind of algorithm described above.

A single SGI workstation is more than adequate to generate and analyse a few thousands events. Unfortunately, a sample of 10^5 ($b - jets$ topology) to 10^8 (minimum biased) background events is required to establish the final merit factor of the SVX detector [1]. Therefore, this code will be ported to a UNIX Farm, made of many data server station running concurrently. The CERN F77 memory manager ZEBRA [11] can be ported to such an environment: using the internal memory I/O capability of the FZ subpackage, these data structures can be exchanged among processors using the CPS package [14].

B. Resource requirements for the Monte-Carlo program

As mentioned in the first section, the BCD Monte-Carlo package based on the GEANT3 [15] system has been used to generate the event samples [1]. The version used for this study required at least 16 Mgb. heap space dedicated to Zebra management. This large amount of space was required to run at the SSC energies, where the track multiplicity for $B - jets$ topologies becomes quite high. For this application, a physical memory of 16 Mgb. at least is required to avoid excess paging. One $B - jets$ event generation at FNAL energy takes approximately 55 seconds cpu time. The average event size is $\approx$ 106 Kb. Most of this data is not the raw digitisation (the *DIGI* d/s) itself, but the information needed in the analysis phase to verify reconstruction algorithms (*KINE*, *VERT* and *HITS* d/s). These ZEBRA files were written on 8mm Exabyte tapes, and are readable on other platforms (VAX VMS, for instance). This software has not been optimized for speed at all, but for convenience and clarity. For instance, the MIPS FORTRAN optimizer has been turned off; more effort is needed to certify the level of optimisation.

C. Resource requirements for the analysis program

The analysis software described in the third section was essentially written stand-alone and does not use much of the GEANT utilities. Extensive use of the CERN F77 memory manager ZEBRA [11] and histogram package HBOOK4 [12] allowed a clean organisation of the various analysis stages. The data structure were originally designed based on the experience gained the from fixed target program, and were documented - at least at the beginning of the project - using MacDraft (see fig 46 for example). Clearly, more SASD tools should have been used. No other commercial software has been used, except DI3000 and MacDraw for graphics and for the stand-alone SVX pattern recognition searches, MacSpin. The CERN mathematical library was found adequate for this application. IMSL software was investigated for the nonlinear fitting and matrix inversions, and rejected based on the negligible performance improvement gained with respect to CERNLIB. In addition, Fermilab Computing Division does not support IMSL on the SGI platform.

One event analysis takes approximately 6 to 18 sec. cpu time, locking roughly 8 Mgb to 12 Mgb for user data (FNAL c.m. energy). The current analysis load is mostly dominated by histogramming or related studies. The data structures and related pointer manipulations were not at all optimized for speed, but for convenience and reliability. Production versions of similar software will need to be considered. Histograms were reviewed and displayed using the CERN PAW system [13].

D. Accuracy of the calculation

In many cases, the helix equations can be exactly solved. The numerical approximations used in the stand-alone analysis program can therefore be verified. It has been determined that the routines to compute the intersection of a track with a wafer must use double precision f. p. on a 32 bit machine. The SVX detector is capable of measuring deviations of $10.\mu$ m. over a distance of one meter or so. Given that a 32 bit floating number has between 5 and 6 significant digit and many floating point operation are done along the path of the track, this is not at all surprising.

Unfortunately, the temporary variables used in the GEANT tracking package are always kept in single precision. Most -if not all- of the step by step track propagations from one volume to the next are computed in single precision. As a result, significant loss of resolution occurs at the event generation phase. The *HITS* information has been

Deviations of the order of a few μm, up to 10 or 25 μm were found for low momentum tracks (of the order of 0.5 GeV/c) at the outer edges of the detector. Fortunately, these errors are not as big as the uncertainties due to multiple scattering for these tracks at these locations (fig 45). Yet, this kind of computational uncertainty severly impairs the debugging and certification of the package and certainly can be avoided. It is anticipated that similar and potentially far more damaging errors will happen in the detailed simulation of the STRAW tracking system.

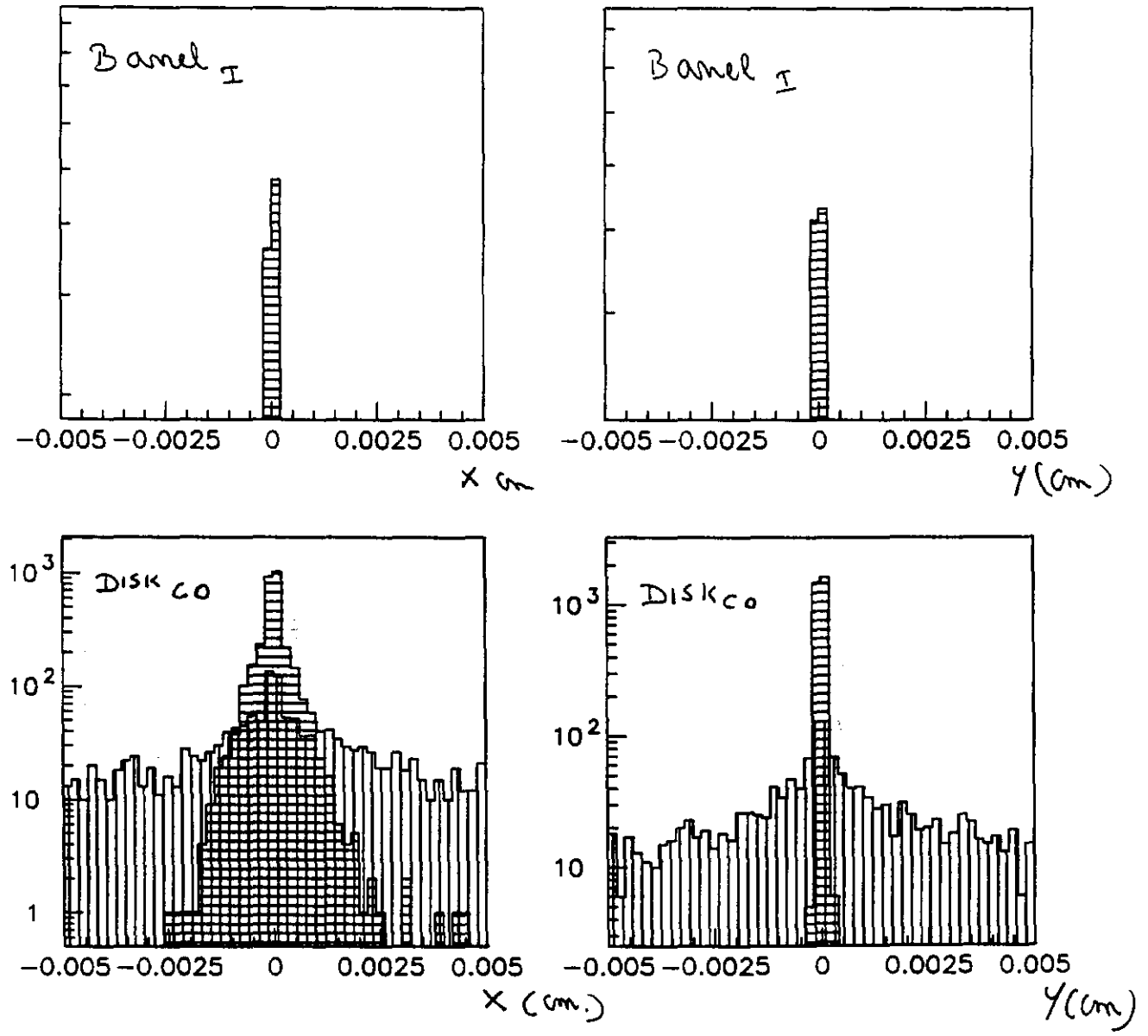

FIG. 45. x deviations measured at the GEANT hit level due to numerical uncertainties (horisontal hash) compared to multiple scattering (vertical hash). The former track sample was obtained by turning the multiple scattering "off" in the GEANT package. Both track sample were generated and the reconstructed hit positions were obtained with the magnetic field "on". The track momentum distribution is flat between 0.5 Gev/c and 1.0 Gev/c. The top curves refers to the inner *BARREL* wafers, where small uncertainties are expected because the GEANT tracing proceeded for only a few steps. The bottom curve refers to the outer *DISK* wafers, where substantial deviations are observed. Fortunately, they are small compared to multiple scattering.

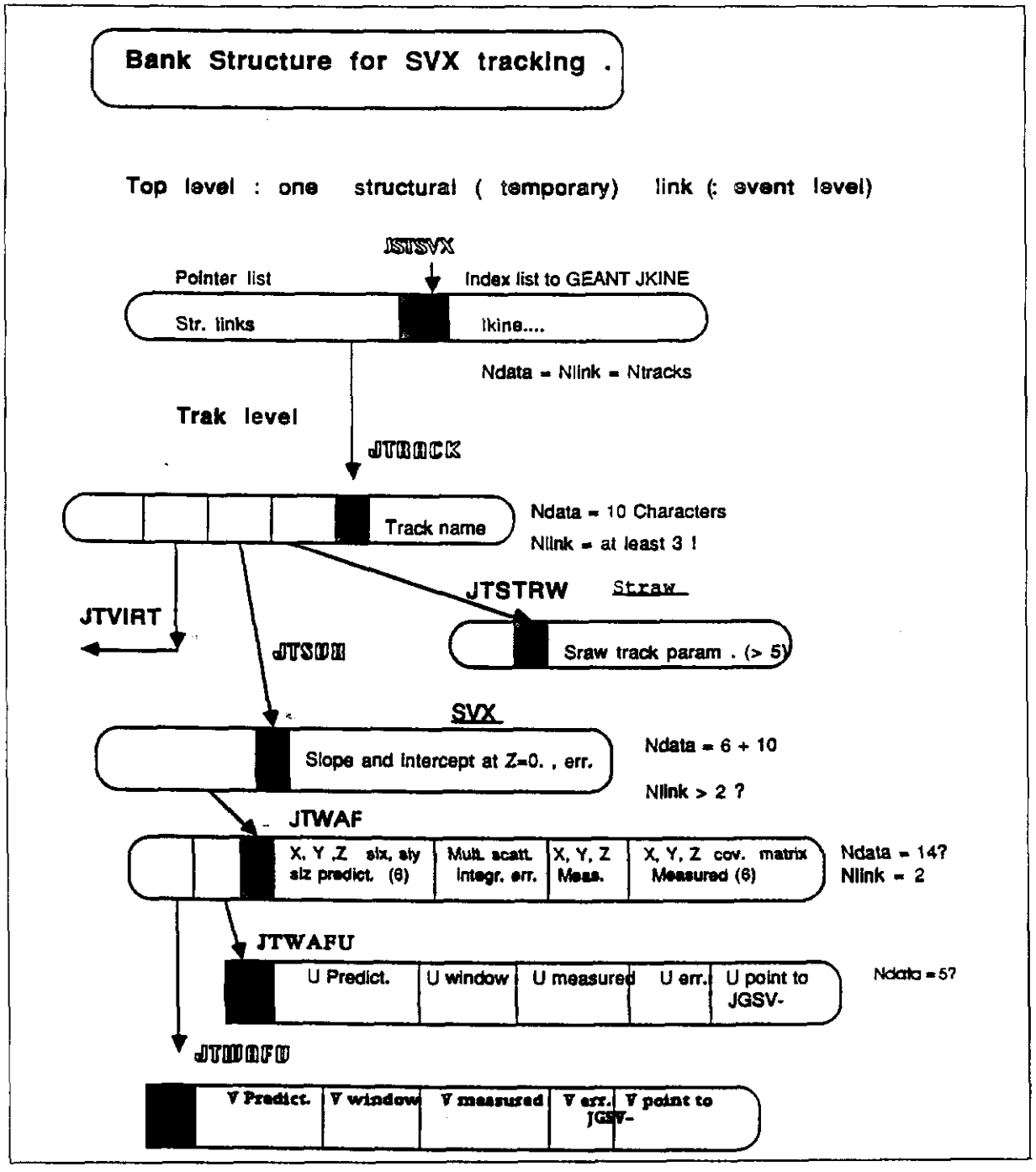

FIG. 46. A typical ZEBRA d/s layout used in the analysis software. Integration between the ZEBRA software running on the workstation and the MacIntosh drawing package obviously deserves improvements...

[1]H. Castro *et al, Expression of interest for a Bottom Collider Detector at the SSC*, May 25 1990.

[2]L.A. Roberts, *Monte Carlo Simulation of Silicon Vertex Detector for Bottom Collider Detector*, Fermilab preprint FN-488 (June, 1988).

[3]F. Abe *et al* Phys. Rev. Lett. *61* 1819 (1988).

[4]H. Mulderink, N. Michels, and H. Jöstlein, *Mechanical and Thermal behavior of a Prototype Support Structure for a Large Silicon Vertex Detector (BCD)*, Fermilab TM-1616 (August 23, 1989); H. Jöstlein and J. Miller, *Heat Resistance and Air-Pressure Drop in a Model of the BCD Silicon Vertex Detector*, Fermilab TM (Jan. 1990).

[5]C. Lindenmeyer, *Proposed Method of Assembly for the BCD Silicon Strip Vertex Detector Modules*, Fermilab TM-1627 (Oct. 16, 1989).

[6]J. D. Bjorken, private communication 1988

[7]C. Lu and K. T. McDonald, *A straw-tube Tracking System for the SSC*, to appear in the Proceedings of the IISC (Miami, Mar. 14-16 1990)

[8]G. R. Kalbfleisch and M. A. Lambrecht, private communication.

[9]This work was done by M. Edel, using a 3dim. graphic tool on the MacIntosh pesrsonal computer called MacSpin. The interface between the GEANT *KINE* structure and MacSpin user interface was written in LISP.

[10]M. Hansroul and J. Kubler (1977). Revised in 1983, *CERN/DD/EE/81-6 document.* Double precision has been used in this application.

[11]R. Brun and J. Zoll, *ZEBRA user guide, CERN program library Q100 1989*

[12]R. Brun and D. Lienart, *HBOOK4 user guide, CERN program library Y250 1989*

[13]R. Brun et al, *PAW Physics analysis workstation, CERN program library Q121 1989*

[14]J. Biel *et al, Fermilab ACP group internal note.*

[15]R. Brun *et al, GEANT3 user Guide, CERN program library DD/EE/84/-1*

[16]P. Billoir, *NIM 225 (1984) 352.*

[17]R. Morrison and J. Cumalat, private communication.

[18]Frank E. Paige and Serban D. Protopopescu, *A MONTE CARLO EVENT GENERATOR FOR P-P AND PBAR-P REACTIONS*, Brookhaven internal note, (1989).

[19]H.-U. Bengtsson, T. Sjostrand, Computer Phys. Comm. 46 (1987) 43

[20]The BCD and CDF collaboration are currently conducting a series of beam test of single and double sided wafer at Fermilab.